ACS OMEGA

http://pubs.acs.org/journal/acsodf

Article

Water/Alcohol Mixture Adsorption in Hydrophobic Materials: Enhanced Water Ingress Caused by Hydrogen Bonding

Rajamani Krishna* and Jasper M. van Baten

Cite This: *ACS Omega* 2020, 5, 28393−28402

Read Online

ACCESS | Metrics & More | Article Recommendations | Supporting Information

ABSTRACT: Microporous crystalline porous materials such as zeolites, metal−organic frameworks, and zeolitic imidazolate frameworks (ZIFs) have potential use for separating water/alcohol mixtures in fixed bed adsorbers and membrane permeation devices. For recovery of alcohols present in dilute aqueous solutions, the adsorbent materials need to be hydrophobic in order to prevent the ingress of water. The primary objective of this article is to investigate the accuracy of ideal adsorbed solution theory (IAST) for prediction of water/alcohol mixture adsorption in hydrophobic adsorbents. For this purpose, configurational bias Monte Carlo (CBMC) simulations are used to determine the component loadings for adsorption equilibrium of water/methanol and water/ethanol mixtures in all-silica zeolites (CHA, DDR, and FAU) and ZIF-8. Due to the occurrence of strong hydrogen bonding between water and alcohol molecules and attendant clustering, IAST fails to provide quantitative estimates of the component loadings and the adsorption selectivity. For a range of operating conditions, the water loading in the adsorbed phase may exceed that of pure water by one to two orders of magnitude. Furthermore, the occurrence of water−alcohol clusters moderates size entropy effects that prevail under pore saturation conditions. For quantitative modeling of the CBMC, simulated data requires the application of real adsorbed solution theory by incorporation of activity coefficients, suitably parameterized by the Margules model for the excess Gibbs free energy of adsorption.

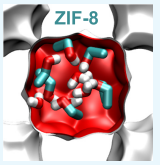

1. INTRODUCTION

Due to the formation of azeotropes, distillation of a water/alcohol mixture is energy-intensive. The use of membrane pervaporation devices in hybrid distillation-membrane processing schemes offers energy-efficient alternatives in production of purified alcohols.[1−5] The membranes may be constructed as thin films of zeolites (e.g., CHA,[3,6] DDR,[7,8] LTA,[9] MFI[10,11]) or zeolitic imidazolate frameworks (ZIFs).[12] The permeation selectivity of membrane constructs, S_{perm}, is dictated by a combination of the adsorption selectivity, S_{ads}, and the diffusion selectivity, S_{diff}.[13−15] The alcohol/water adsorption selectivity, S_{ads}, is defined by

$$S_{ads} = \frac{q_2/q_1}{f_2/f_1} = \frac{q_2/q_1}{y_2/y_1}; \quad y_1 = \frac{f_1}{f_t}; \quad f_t = f_1 + f_2 \tag{1}$$

where q_1 and q_2 are the molar loadings of the water and alcohol, respectively, in the adsorbed phase in equilibrium with a bulk fluid phase mixture with partial fugacities f_1 and f_2 and composition $y_1 = 1 - y_2$. Due to the narrow 3.8−4.1 Å window sizes of CHA, DDR, and LTA zeolites, the diffusion selectivity, S_{diff}, favors water transport.[5,16] For water-selective dehydration of feed streams of near-azeotropic composition, hydrophilic LTA-4A (= NaA) membranes are applied on a commercial scale.[17] Hydrophobic membranes made of materials such as all-silica MFI and ZIF-8 are suitable for enrichment of feed mixtures that are dilute in alcohol.[11,18]

In the production of bioalcohols by fermentation of biomass, the desired products such as bioethanol and biobutanol are available in low concentrations in the fermentation broth; consequently, distillation separations are infeasible. One separation strategy is to use fixed bed adsorption devices packed with hydrophobic microporous materials, such as all-silica MFI (also called silicalite-1), ZIF-8, ZIF-71, and MOFs.[18−22] The separation efficacy of fixed bed adsorbers is dictated by a combination of mixture adsorption equilibrium and intracrystalline diffusion of guest molecules.

For estimation of the component loadings q_1 and q_2 and selectivity, S_{ads}, it is common to use ideal adsorbed solution theory (IAST)[23] that requires the unary isotherm data as inputs. The IAST approach has been used in a number of published works for evaluating and screening adsorbents for a wide variety of mixture separations.[18,24−29]

For adsorption of water/alcohol mixtures in all-silica MFI zeolite, molecular simulations have established the occurrence of molecular clusters engendered by hydrogen bonding between water and alcohol molecules.[11,30−37] Such molecular clustering results in significantly enhanced water ingress that is not anticipated by IAST.[11,31] For adsorption of mixtures of water/ethanol mixtures of constant composition, y_1, in MFI zeolite, the molecular simulation data of Gómez-Álvarez et al.[33] also showed

Received: September 13, 2020
Accepted: October 9, 2020
Published: October 22, 2020

https://dx.doi.org/10.1021/acsomega.0c04491
ACS Omega 2020, 5, 28393−28402

that the ethanol/water selectivity decreases with increasing pore occupancy.

The primary objective of this article is to demonstrate that the enhanced water ingress, as evidenced by MFI zeolite in published works, is a common characteristic of other all-silica zeolites and also hydrophobic ZIFs. Toward this end, configurational bias Monte Carlo (CBMC) simulations of water/methanol and water/ethanol mixture adsorption equilibrium were performed for three all-silica zeolites (CHA, DDR, and FAU) and ZIF-8. The secondary objective is to elucidate the reasons behind the failure of the IAST to provide quantitatively accurate predictions of mixture adsorption. The tertiary objective is to show how the nonidealities in mixture adsorption can be quantified and modeled.

The CBMC simulation methodology used in this article follows published works.[14,38−41] All host materials are considered to be rigid in the simulations, performed at a temperature T = 300 K. The force field implementation follows earlier publications.[7,35,37,42] Water is modeled using the Tip5pEw potential.[43] The alcohols are described with the TraPPE force field.[44] Intramolecular potentials are included to describe the flexibility of alcohols, while the water molecules are kept rigid. The bond lengths are fixed for all molecules. Bond bending potentials are considered for methanol and ethanol, and a torsion potential is used for ethanol.[44] Further details, including force field parameters, are provided in the Supporting Information accompanying this publication.

2. RESULTS AND DISCUSSION

2.1. IAST Prescriptions and Origins of Nonidealities. In the Myers−Prausnitz development of IAST,[23] the partial fugacities in the bulk fluid mixture are related to the mole fractions x_i in the adsorbed phase mixture

$$x_i = q_i/q_t; \quad q_t = q_1 + q_2; \quad i = 1, 2 \tag{2}$$

by the analogue of Raoult's law for vapor−liquid equilibrium, i.e.

$$f_i = x_i P_i^0; \quad i = 1, 2, \ldots n \tag{3}$$

where P_i^0 is the pressure for sorption of every component i, which yields the same spreading pressure, π for each of the pure components, as that for the mixture:

$$\frac{\pi A}{RT} = \int_0^{P_1^0} \frac{q_1^0(f)}{f} \mathrm{d}f = \int_0^{P_2^0} \frac{q_2^0(f)}{f} \mathrm{d}f \tag{4}$$

In eq 4, A represents the surface area per kilogram of framework and $q_i^0(f)$ is the pure component adsorption isotherm. Since the surface area A is not directly accessible from experimental data, the adsorption potential $\pi A/RT$, with the unit mol kg^{-1}, serves as a convenient and practical proxy for the spreading pressure π. For binary mixture adsorption, each of the equalities on the right-hand side of eq 4 must be satisfied. These constraints may be solved using a suitable equation solver to yield the set of values of P_1^0, and P_2^0, both of which satisfy eq 4. The corresponding values of the integrals using these as upper limits of integration must yield the same value of $\frac{\pi A}{RT}$ for each component; this ensures that the obtained solution is the correct one.

The applicability of the Raoult law analog, eq 3, mandates that all of the adsorption sites within the microporous material are equally accessible to each of the guest molecules, implying a homogeneous distribution of guest adsorbates within the pore landscape, with no preferential locations of any guest species.[45,46] This prescription is fulfilled for adsorption of mixtures of nonpolar guest molecules in relatively "open" host materials. As an illustration, Figure 1a compares IAST estimates

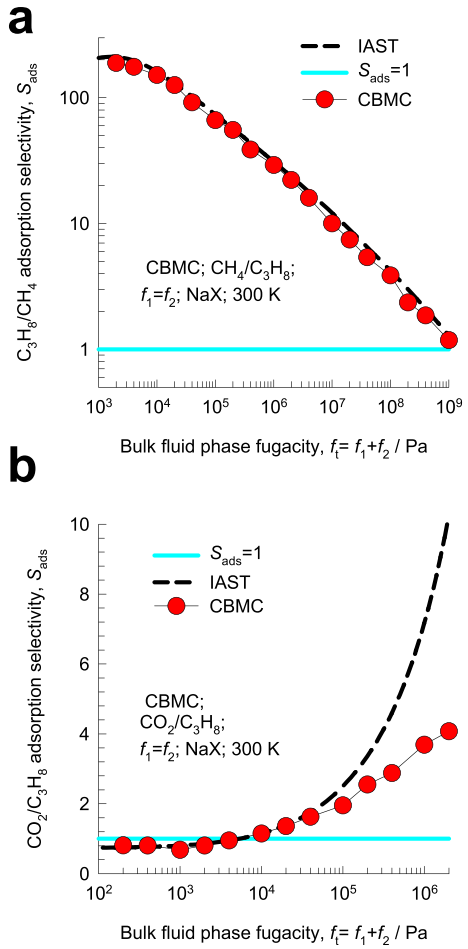

Figure 1. CBMC simulation data for (a) CH_4/C_3H_8 and (b) CO_2/C_3H_8 mixture adsorption in NaX zeolite (106 Si, 86 Al, 86 Na^+, Si/Al = 1.23) at 300 K, with equal partial fugacities, $f_1 = f_2$, in the bulk fluid phase mixture. The dashed lines are the IAST calculations of the component loadings. Further information on the data inputs and calculations are provided in the Supporting Information accompanying this publication.

of S_{ads} with CBMC data for equimolar CH_4/C_3H_8 mixtures in cation-exchanged NaX zeolite. Noteworthily, IAST quantitatively predicts the decrease in C_3H_8/CH_4 selectivity with increasing bulk fugacity, f_t; this decrease is engendered by entropy effects that favor the smaller methane molecule that has the higher saturation capacity.[24,47] However, for adsorption of CO_2/C_3H_8 mixtures in NaX zeolite, IAST overestimates the CO_2/C_3H_8 selectivity because the CO_2 molecules tend to congregate around the Na^+ cations, thereby reducing the competition between the two guest species;[45,46,48] see Figure 1b.

A further key assumption of IAST is that the enthalpies and surface areas of the adsorbed molecules do not change upon mixing.[23] If the total mixture loading is q_t, the area covered by the adsorbed mixture is $\frac{A}{q_t}$ with a unit of m^2 (mole mixture)$^{-1}$. Therefore, the assumption of no surface area change due to mixture adsorption translates as

https://dx.doi.org/10.1021/acsomega.0c04491
ACS Omega 2020, 5, 28393−28402

$$\frac{A}{q_t} = \frac{Ax_1}{q_1^0(P_1^0)} + \frac{Ax_2}{q_2^0(P_2^0)} \quad (5)$$

The occurrence of molecular clustering due to hydrogen bonding should be expected to invalidate the use of eq 5 in the IAST calculations of q_t.

2.2. Evidence of Hydrogen Bonding for Water/Alcohol Mixture Adsorption. In order to demonstrate the occurrence of hydrogen bonding in water/methanol and water/ethanol mixtures, CBMC simulation data on the spatial locations of the guest molecules were sampled to determine the O···H distances of various pairs of molecular distances. By sampling a total of 10^6 simulation steps, the radial distribution functions (RDFs) of O···H distances were determined for water−water, water−alcohol, and alcohol−alcohol pairs. Figure 2a shows the RDF of O···H distances for molecular pairs of water(1)/methanol(2) mixture adsorption in CHA zeolite at 300 K. The partial fugacities of components 1 and 2 are f_1 = 2.5 kPa and f_2 = 7.5 kPa. We note that the first peaks in the RDFs occur at a distance less than 2 Å, which is characteristic of hydrogen bonding.[35,49] The heights of the first peaks are a direct reflection of the degree of hydrogen bonding between the molecular pairs. We may conclude therefore that for water/methanol mixtures, the degree of H bonding between water−methanol pairs is significantly larger, by about an order of magnitude, than for water−water and methanol−methanol pairs. An analogous set of conclusions can be drawn for water/ethanol mixtures, for which the RDF data are presented in Figure 2b: that is, the degree of H bonding between water−ethanol pairs is larger than for water−water and ethanol−ethanol pairs. For comparison purposes, the RDF data for adsorption of methanol/ethanol mixtures are shown in Figure 2c. The magnitudes of the first peaks for methanol−ethanol, methanol−methanol, and ethanol−ethanol pairs are significantly lower than those of the water−alcohol peaks in Figure 2a,b. Therefore, the H-bonding effects should be expected to be of lesser importance for methanol/ethanol mixture adsorption in CHA than for water/methanol and water/ethanol mixtures.

Analogous results are obtained for the RDFs in DDR, MFI, and ZIF-8; see Figures S15−S22 of the Supporting Information.

2.3. Water/Alcohol Mixture Adsorption; CBMC vs IAST. Figure 3a compares CBMC simulations of unary water isotherms in different microporous host materials, plotted as a function of the fugacity of water in the bulk fluid phase. The plot clearly shows the difference between various hydrophobic hosts (all-silica zeolites, ZIF-8, ZIF-71) and hydrophilic host CuBTC; for hydrophobic hosts, the bulk fluid phase fugacity needs to be at least 1 kPa before significant water uptake is realized.

Two types of mixture adsorption simulation campaigns were conducted. In campaign A, the bulk fluid phase mixture is equimolar, $f_1 = f_2$, and the bulk fluid phase fugacity $f_t = f_1 + f_2$ was varied over a wide range from the Henry regime of adsorption, f_t = 1 Pa, to near pore saturation conditions, typically f_t>50 kPa. In campaign B, the bulk fluid phase fugacity $f_t = f_1 + f_2$ was held at a constant value of 10 kPa, and the bulk fluid phase mixture composition was varied, $0<y_1<1$. The obtained results for both sets of campaigns in the different host materials are presented in Figures S24−S50 of the Supporting Information.

As an illustration, Figure 3b presents the CBMC data for campaign A of water/ethanol mixture adsorption in DDR. The component loadings in the adsorbed mixture (filled symbols) are compared with CBMC simulations of unary isotherms (open symbols) at the same partial fugacity, f_i, in the bulk phase. For f_i < 10 kPa, the ethanol loading in the mixture is practically identical to that of the unary isotherm while the water loading in the mixture is considerably larger than that of pure water. For f_i < 10 kPa, the IAST calculations (indicated by the dashed lines) do not anticipate the substantially enhanced water ingress from the mixture because the influence of molecular clustering is not catered for in the theoretical development of IAST. From a close

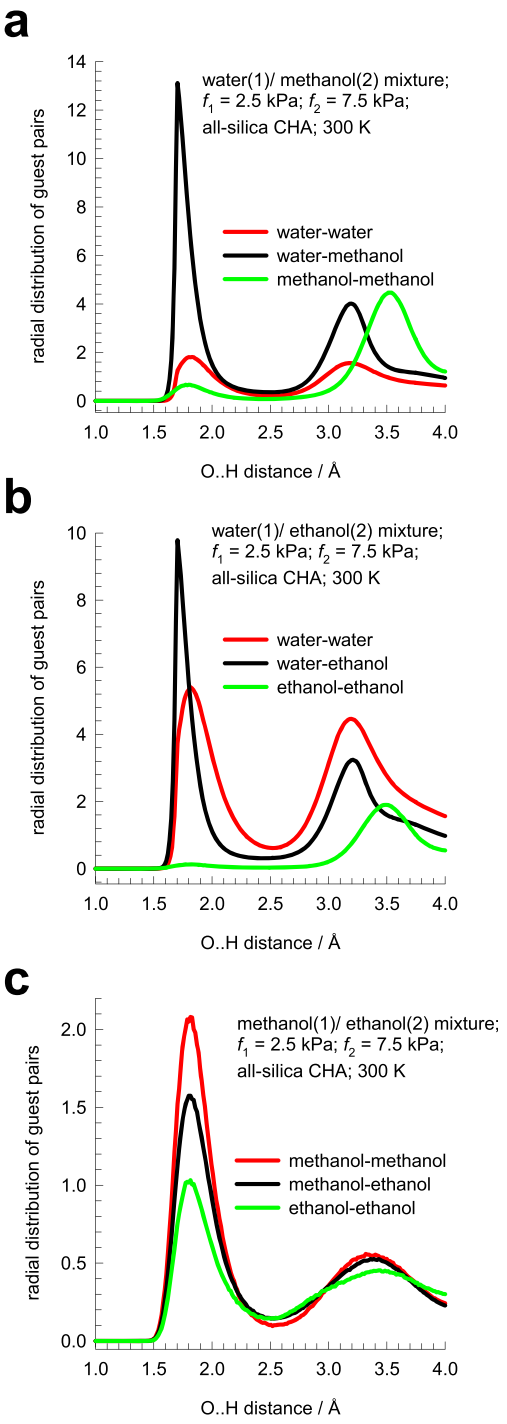

Figure 2. RDF of O···H distances for molecular pairs of (a) water(1)/methanol(2), (b) water(1)/ethanol(2), and (c) methanol(1)/ethanol(2) mixture adsorption in CHA zeolite at 300 K. For all three sets of mixtures, the partial fugacities of components 1 and 2 are f_1 = 2.5 kPa and f_2 = 7.5 kPa. The y-axes are normalized in the same manner, and therefore, the magnitudes of the first peaks are a direct reflection of the degree of hydrogen bonding between the molecular pairs.

https://dx.doi.org/10.1021/acsomega.0c04491
ACS Omega 2020, 5, 28393−28402

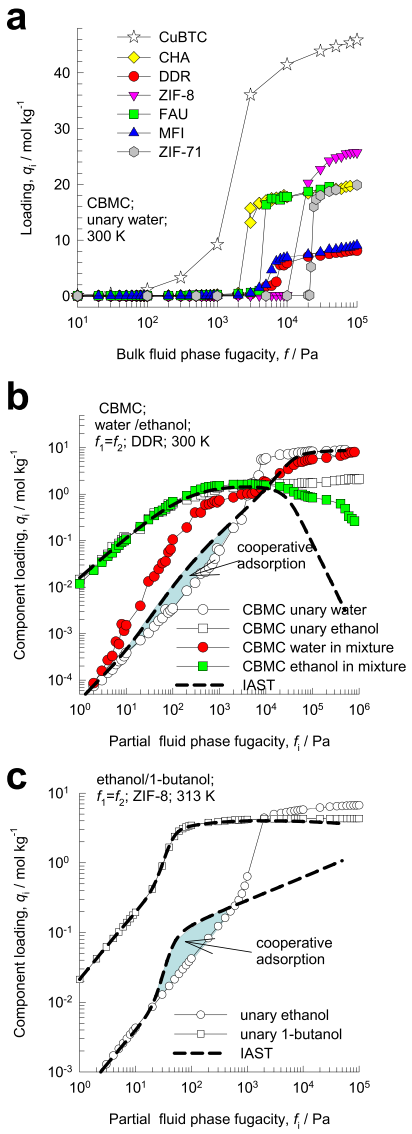

Figure 3. (a) Comparison o CBMC simulations of unary water isotherms in different microporous host materials, plotted as a function of the fugacity of water in the bulk fluid phase. (b) CBMC simulation data for water(1)/ethanol(2) mixture adsorption in DDR at 300 K with equal partial fugacities, $f_1 = f_2$, in the bulk fluid phase mixture. The component loadings in mixture (filled symbols) are compared with CBMC simulations of unary isotherms (open symbols), both plotted as a function of the partial fugacity f_i in the bulk fluid phase mixture. The dashed lines are the IAST calculations of the component loadings. Further information on the data inputs and calculations are provided in the Supporting Information accompanying this publication. (c) IAST calculations of the component loadings for ethanol/1-butanol mixture adsorption in ZIF-8 are compared with the unary isotherm data fits reported by Claessens et al.[20]

examination of Figure 3b, it is also noteworthy that water loading from the IAST calculations also exceeds the unary water loading, albeit to a minor extent as indicated by the shaded area. This increase in the loading of the lighter component in the mixture is a common characteristic of mixtures in which the lighter component (with higher saturation capacity) exhibits a much steeper unary isotherm than that of the heavier component (with lower saturation capacity). For adsorption of ethanol/1-butanol mixtures in ZIF-8, the experiments of Claessens et al.[20] demonstrated that the ethanol loading in the mixture may exceed that of pure ethanol over a certain limited range of bulk fugacities; see Figure 3b. These authors have dubbed this phenomenon as "co-operative adsorption" and have further demonstrated that IAST is capable of describing such effects. By contrast, for water/ethanol adsorption in DDR, the CBMC data for enhancement in the water loading far exceeds the IAST value. To put it another way, hydrogen bonding effects tend to significantly amplify the "co-operative adsorption" effect.

By dividing the CBMC data on water loadings in the mixture by the corresponding loading determined from the unary water isotherm, the enhancement in the water loading can be determined. These data are summarized in Figure 4a,b for

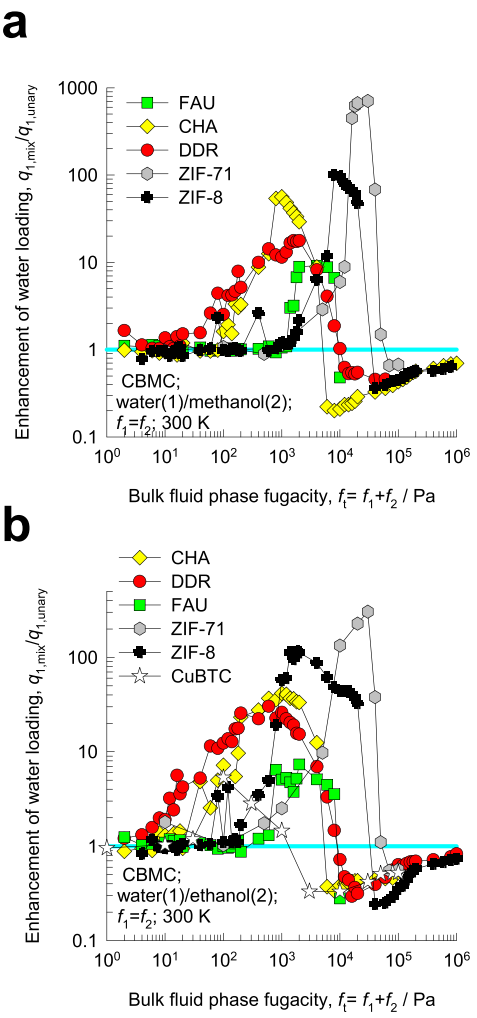

Figure 4. Enhancement of water loading in (a) water(1)/methanol(2) and (b) water(1)/ethanol(2) mixtures, determined from CBMC simulations for mixture adsorption in various host materials at 300 K with equal partial fugacities, $f_1 = f_2$, in the bulk fluid phase mixture. The x axis represents the bulk fluid phase fugacity $f_t = f_1 + f_2$. Also included are the data for ZIF-71[52] and CuBTC.[50,51] Further information on the data inputs and calculations are provided in the Supporting Information accompanying this publication.

water/methanol and water/ethanol mixtures in different host materials; the data sets include those for hydrophilic CuBTC and hydrophobic ZIF-71, culled from the published literature.[50−52] For a range of bulk fluid phase fugacities, the enhancement in the water loadings may range from 10 to 500.

https://dx.doi.org/10.1021/acsomega.0c04491
ACS Omega 2020, 5, 28393−28402

Figure 5a,b summarizes the CBMC data for methanol/water and ethanol/water selectivities, S_{ads}, in different host materials.

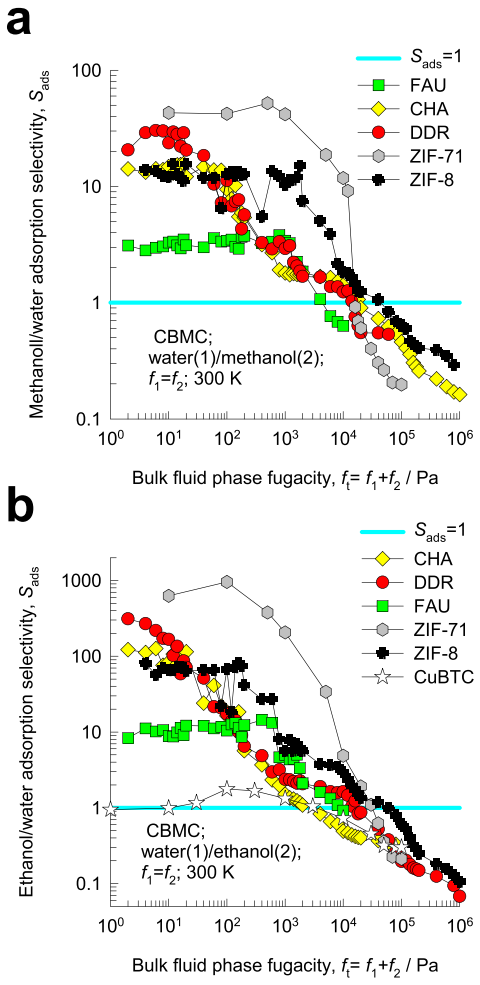

Figure 5. CBMC simulation data for alcohol/water adsorption selectivity for (a) water(1)/methanol(2) and (b) water(1)/ethanol(2) mixtures in various host materials at 300 K with equal partial fugacities, $f_1 = f_2$, in the bulk fluid phase mixture. The x axis represents the bulk fluid phase fugacity $f_t = f_1 + f_2$. Also included are the data for ZIF-71[52] and CuBTC.[50,51] Further information on the data inputs and calculations are provided in the Supporting Information accompanying this publication.

In all cases, the selectivity reverses in favor of water as pore saturation conditions are approached, typically for f_t > 50 kPa. Water is preferentially adsorbed due to size entropy effects that favor the smaller molecule due to improved packing within the pore landscape.[24,47] For hydrophobic all-silica CHA and FER zeolites, the experiments of Arletti et al.[53] and Confalonieri et al.[54] provide confirmation that adsorption of water/ethanol mixtures is water-selective at high pore occupancies.

In Figure 6a, the CBMC data for ethanol/water selectivity in DDR, S_{ads}, are compared with IAST estimates. IAST takes due account of entropy effects and selectivity reversals, but the quantitative agreement with the CBMC data is not adequate because the IAST development does not account for molecular clustering; IAST essentially portrays an exaggerated influence of entropy effects. For f_t < 20 kPa, S_{ads} is overestimated because IAST ignores water uptake induced by hydrogen bonding. For f_t > 50 kPa, cluster formation tends to moderate entropy effects,

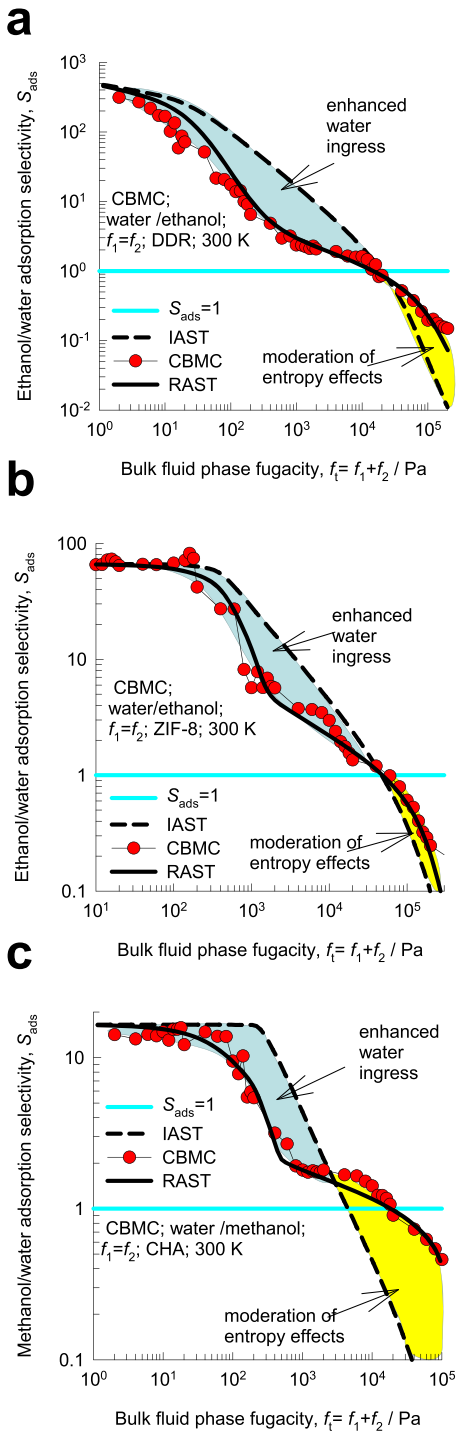

Figure 6. CBMC simulation data for the alcohol/water selectivity for water(1)/alcohol(2) mixture adsorption in (a) DDR, (b) ZIF-8, and (c) CHA at 300 K with equal partial fugacities, $f_1 = f_2$, in the bulk fluid phase mixture. The dashed lines are the IAST calculations of the component loadings. The continuous solid lines are the RAST calculations using the Margules model. Further information on the data inputs and calculations are provided in the Supporting Information accompanying this publication.

causing the IAST calculations for alcohol/water selectivity to fall below those determined from CBMC. Precisely analogous results are obtained for deviations of IAST from CBMC simulation results for water/ethanol/ZIF-8 and water/methanol/CHA; see Figure 6b,c. Comparisons of the CBMC data S_{ads}

https://dx.doi.org/10.1021/acsomega.0c04491
ACS Omega 2020, 5, 28393−28402

with IAST estimates for all investigated mixture/host combinations are available in Figures S24−S50 of the Supporting Information. They all show common characteristics that are illustrated in Figure 6a−c for three different cases.

Molecular dynamics simulation data for mixture diffusion have shown that cluster formation tends to reduce the diffusivities of both water and alcohol molecules;[5,33,35,42,55−58] this mutual slowing-down phenomena is a corollary to the moderation of entropy effects in mixture adsorption.

For methanol/ethanol adsorption in CHA, Figure 7a compares the CBMC simulation data for S_{ads} with IAST

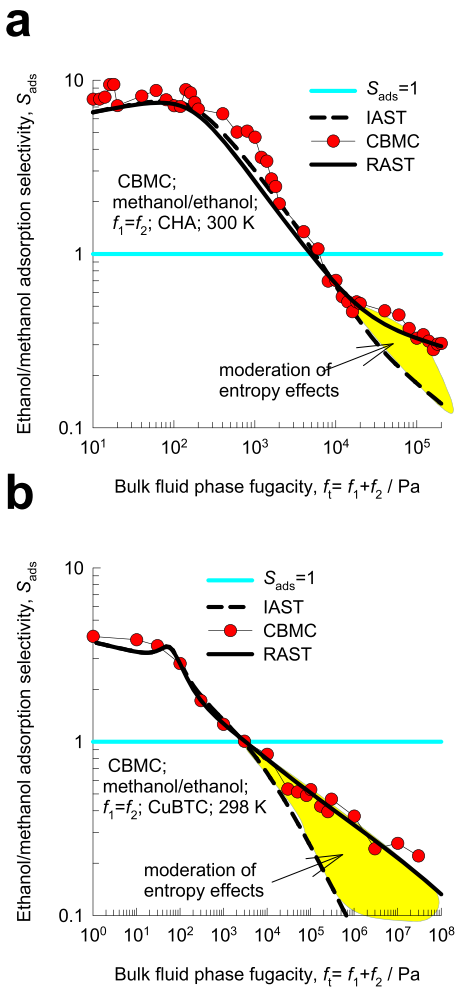

Figure 7. CBMC simulation data for ethanol/methanol adsorption selectivity for methanol(1)/ethanol(2) mixtures with equal partial fugacities, $f_1 = f_2$, in (a) CHA and (b) CuBTC. The x axis represents the bulk fluid phase fugacity $f_t = f_1 + f_2$. The dashed lines are the IAST calculations of the component loadings. The continuous solid lines are the RAST calculations using the Margules model. Further information on the data inputs and calculations are provided in the Supporting Information accompanying this publication.

estimates. There is good agreement between the two data sets for bulk phase fugacities f_t < 10 kPa because hydrogen bonding effects are smaller than for water/alcohol systems, as witnessed in Figure 2. The entropy-driven selectivity reversal in favor of methanol is correctly predicted by IAST. For f_t > 50 kPa, as pore saturation conditions are approached, IAST tends to underestimate the ethanol/methanol selectivity due to moderation of entropy effects as a result of some degree of molecular clustering that prevail at pore saturation. Analogous results are obtained for methanol/ethanol adsorption in hydrophilic CuBTC; see Figure 7b.

Figure 8a presents CBMC data for ethanol/water selectivity in DDR zeolite for campaign B, in which the bulk fluid composition is varied. The CBMC data show that for water-rich mixtures,

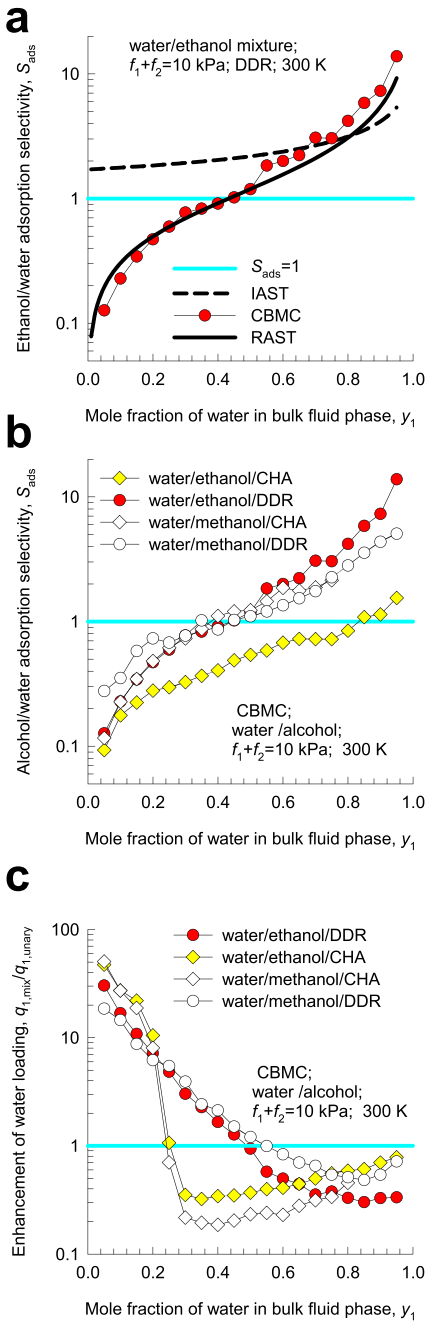

Figure 8. (a) Comparisons of CBMC data for S_{ads} with IAST (dashed line) and RAST calculations (continuous solid line) for water/ethanol adsorption in DDR for $f_t = f_1 + f_2 = 10$ kPa. (b) CBMC simulation data for alcohol/water adsorption selectivities, S_{ads}, in CHA and DDR zeolites at 300 K; the bulk fluid phase is maintained at a constant fugacity $f_t = f_1 + f_2 = 10$ kPa, and the mole fraction of water in the bulk mixture y_1 is varied. (c) Enhancement of water loading for water/alcohol mixture adsorption in CHA and DDR for $f_t = f_1 + f_2 = 10$ kPa. Further information on the data inputs and calculations are provided in the Supporting Information accompanying this publication.

https://dx.doi.org/10.1021/acsomega.0c04491
ACS Omega 2020, 5, 28393−28402

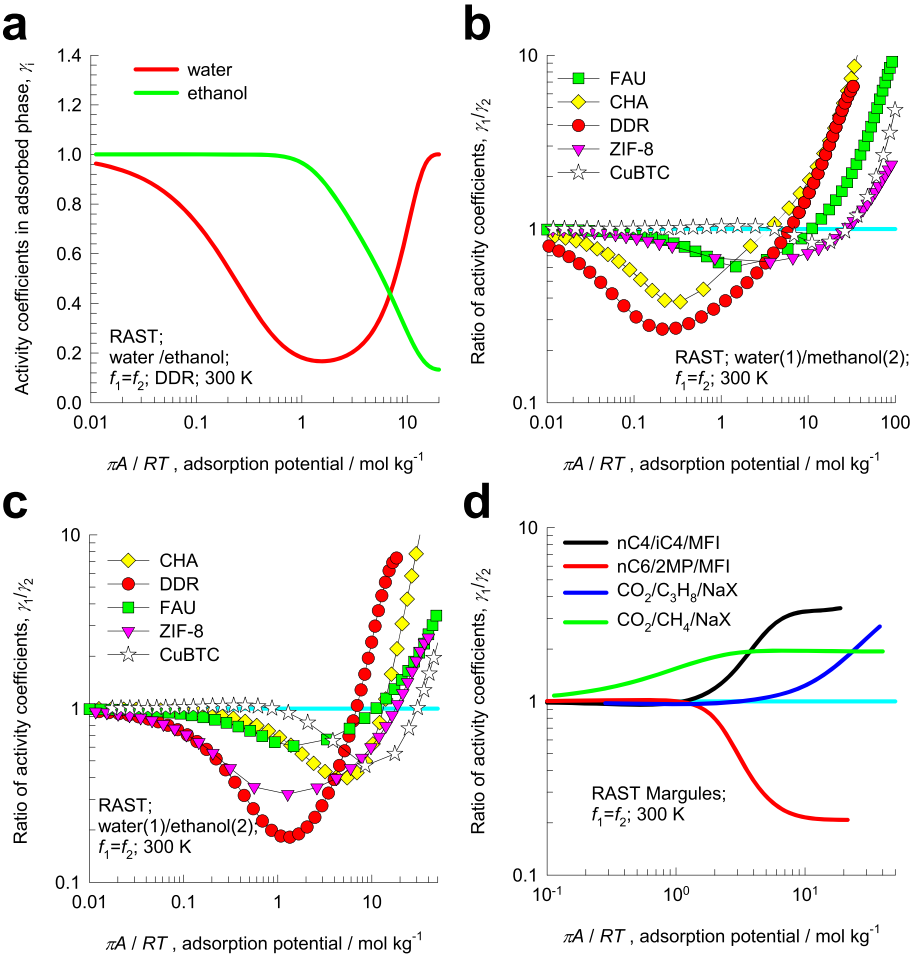

Figure 9. (a) RAST calculations of activity coefficients γ_i for water/ethanol adsorption in DDR zeolite at 300 K with equal partial fugacities, $f_1 = f_2$, in the bulk fluid phase mixture, plotted as a function of the adsorption potential, $\pi A/RT$. (b, c) RAST calculations of the ratio of activity coefficients γ_1/γ_2 for (b) water/methanol and (c) water/ethanol mixtures in different hosts. (d) RAST calculations of the ratio of activity coefficients γ_1/γ_2 for $CO_2(1)/C_3H_8(2)$/NaX, $CO_2(1)/CH_4(2)$/NaX, nC4(1)/iC4(2)/MFI, and nC6(1)/2MP(2)/MFI. Further information on the data inputs and calculations are provided in the Supporting Information accompanying this publication.

y_1>0.5, the adsorption is ethanol-selective; this is desired of adsorbents in recovery of bioethanol from fermentation broths. However, for feed mixtures that are richer in ethanol, y_1<0.5, the adsorption is water-selective; this is a desirable feature for use of DDR in membrane constructs for water-selective pervaporation processes.[7] The narrow 8-ring windows of DDR, with dimensions of 3.65 Å × 4.37 Å, ensure that the diffusion selectivity S_{diff} also favors water.[16,35,37,42] IAST (dashed line) anticipates ethanol-selective adsorption over the entire range of y_1. Analogous results are obtained for water/alcohol mixture adsorption in CHA; see Figure 8b. Adsorption of alcohol-rich feed mixtures in CHA is water-selective; therefore, CHA membranes are used for purification of alcohols by membrane pervaporation because diffusion through 3.8 Å × 4.2 Å 8-ring windows of CHA also favors water.[6,16,35,37,42]

For rationalization of these results, Figure 8c plots the enhancement in the water loading as a function of y_1. We note that for dilute aqueous alcohol solutions with y_1<0.2, the enhancement in the water loading is about one to two orders of magnitude. Each water molecule has a greater probability of forming O···H bonds with alcohols due to the preponderance of alcohol molecules that are present.

There is evidence that molecular clustering effects induced by hydrogen bonding also cause failure of IAST to provide quantitative description of adsorption equilibrium for methanol/benzene, ethanol/benzene, acetone/benzene, methanol/*n*-hexane, 1-propanol/toluene, and 1-butanol/*p*-xylene mixtures in CuBTC and cation-exchanged zeolites;[36,50,51,59−61] detailed analyses are provided in Figures S37−S44 and S55−S57.

2.4. RAST Modeling of Thermodynamic Nonidealities.

To account for nonideality effects in mixture adsorption, engendered by hydrogen bonding, we need to introduce activity coefficients γ_i into eq 3

$$f_i = \gamma_i x_i P_i^0 \tag{6}$$

The implementation of the activity coefficients is termed as real adsorbed solution theory (RAST). Following the approaches of Myers, Talu, and Sieperstein,[62−64] we model the excess Gibbs free energy for binary mixture adsorption as follows

$$\frac{G^{excess}}{RT} = x_1 \ln(\gamma_1) + x_2 \ln(\gamma_2) \tag{7}$$

A variety of models such as Regular solution,[64] Wilson,[45,46,48] NRTL,[65] SPD,[63] and Margules[11] have been used for describing the composition dependence of γ_i. Here, we employ the Margules model, which is particularly suitable for water/alcohol mixtures,[11] expressed in the following form

https://dx.doi.org/10.1021/acsomega.0c04491
ACS Omega 2020, 5, 28393−28402

$$\ln(\gamma_1) = x_2^2(A_{12} + 2(A_{21} - A_{12})x_1)\left(1 - \exp\left(-C\frac{\pi A}{RT}\right)\right)$$

$$\ln(\gamma_2) = x_1^2(A_{21} + 2(A_{12} - A_{21})x_2)\left(1 - \exp\left(-C\frac{\pi A}{RT}\right)\right) \quad (8)$$

In eq 8, C is a constant with the unit kg mol^{-1}. The introduction of $\left(1 - \exp\left(-C\frac{\pi A}{RT}\right)\right)$ imparts the correct limiting behaviors $\gamma_i \to 1$; $\frac{\pi A}{RT} \to 0$ for the activity coefficients in the Henry regime, $f_t \to 0$; $\frac{\pi A}{RT} \to 0$. As pore saturation conditions are approached, this correction factor tends to unity $\left(1 - \exp\left(-C\frac{\pi A}{RT}\right)\right) \to 1$.

For calculation of the total mixture loading, eq 5 is replaced by

$$\frac{1}{q_t} = \frac{x_1}{q_1^0(P_1^0)} + \frac{x_2}{q_2^0(P_2^0)} + x_1x_2[A_{12}x_2 + A_{21}x_1]C\exp\left(-C\frac{\pi A}{RT}\right) \quad (9)$$

The parameters A_{12}, A_{21}, C can be fitted to match the CBMC data on mixture adsorption. Further details of the RAST model calculations, fitting methodology, and values of the fitted Margules parameters are provided in the Supporting Information. As an illustration, Figure 9a presents RAST calculations of activity coefficients γ_i for water/ethanol adsorption in DDR zeolite, plotted as a function of the adsorption potential, $\pi A/RT$. The water activity coefficient exhibits a deep minimum for conditions under which significant enhancement in the water ingress is caused by hydrogen bonding. Analogous characteristics are found for other guest/host combinations as evidenced in Figure 9b,c in which the ratio of activity coefficients γ_1/γ_2 is plotted for (a) water/methanol and (b) water/ethanol mixtures in different host materials. The non-monotonic variation of γ_1/γ_2 with increasing $\pi A/RT$ is a distinguishing and common characteristic of nonidealities induced by hydrogen bonding; in sharp contrast, for nonidealities engendered by congregation/segregation effects,[45,46,48] the variation of γ_1/γ_2 with increasing $\pi A/RT$ is monotonic; see Figure 9d. In the range of $\pi A/RT$ values for which $\gamma_1/\gamma_2<1$, IAST overestimates S_{ads} because of enhanced water ingress, indicated by the cyan shaded areas in Figure 6a−c. In the range of $\pi A/RT$ values for which $\gamma_1/\gamma_2>1$, IAST underestimates S_{ads} because of moderation of entropy effects, indicated by the yellow shaded areas in Figure 6a−c.

The continuous solid lines in Figures 6−8 are the RAST calculations of S_{ads}; the improvement over the corresponding IAST estimation is significant, as should be expected.

3. CONCLUSIONS

Two different CBMC campaigns, A and B, for water/methanol and water/ethanol adsorption in hydrophobic CHA, DDR, FAU, and ZIF-8 were undertaken to investigate the accuracy of IAST estimates of component loadings and adsorption selectivities.

For CBMC simulation campaign A with equimolar bulk fluid mixtures, $f_1 = f_2$, the increase of $f_t = f_1 + f_2$ from 1 Pa to about 10 kPa shows that the water ingress in the host material is significantly higher than that anticipated from the pure water isotherm data. The enhancement in the water ingress is induced by the formation of water/alcohol clusters due to hydrogen bonding; this enhanced water ingress is not anticipated by IAST. When pore saturation conditions are approached, typically f_t>50 kPa, the CBMC simulations show selectivity reversal in favor of water; this selectivity reversal is driven by size entropy effects that favor water to pack more efficiently. The formation of water/alcohol clusters has a moderating influence on size entropy effects. Since molecular clustering is not recognized in the IAST development, the entropy effects are exaggerated; consequently, IAST estimates of S_{ads} are more water-selective than that observed in the CBMC data.

The CBMC simulations following campaign B in which the bulk fluid phase fugacity is held constant, f_t = 10 kPa, show that for CHA and DDR, the adsorption of alcohol-rich mixtures is water-selective and suitable for use in membrane pervaporation processes for alcohol purification. For water-rich mixture, the adsorption is alcohol-selective and therefore suitable for use in the recovery of bioalcohols.

The quantitative modeling of water/alcohol mixture adsorption in hydrophobic adsorbent requires use of RAST, with appropriate parametrization of the model to describe activity coefficients. For all hydrophobic adsorbents, the variation of the activity coefficients with the spreading pressure displays common characteristics as evidenced in Figure 9b,c.

■ ASSOCIATED CONTENT

Supporting Information

The Supporting Information is available free of charge at https://pubs.acs.org/doi/10.1021/acsomega.0c04491.

Structural details of zeolites, MOFs, and ZIFs, details of the CBMC simulation methodology, details of the IAST and real adsorbed solution theory (RAST) calculations for mixture adsorption equilibrium, unary isotherm fits for all the guest/host combinations, Margules parameter fits for thermodynamic nonidealities, and plots of CBMC simulation data and comparisons with IAST/RAST estimates for all guest/host combinations (PDF)

■ AUTHOR INFORMATION

Corresponding Author

Rajamani Krishna − *Van't Hoff Institute for Molecular Sciences, University of Amsterdam, XH, Amsterdam 1098, The Netherlands;* orcid.org/0000-0002-4784-8530; Email: r.krishna@contact.uva.nl

Author

Jasper M. van Baten − *Van't Hoff Institute for Molecular Sciences, University of Amsterdam, XH, Amsterdam 1098, The Netherlands*

Complete contact information is available at: https://pubs.acs.org/10.1021/acsomega.0c04491

Notes

The authors declare no competing financial interest.

■ ACKNOWLEDGMENTS

The authors acknowledge Dr. Richard Baur for helpful discussion.

■ NOMENCLATURE

Latin alphabet

A surface area per kg of framework, m^2 kg^{-1}

A_{12}, A_{21} Margules parameters, dimensionless

https://dx.doi.org/10.1021/acsomega.0c04491
ACS Omega 2020, 5, 28393−28402

C constant used in eq [8], kg mol^{-1}
f_i partial fugacity of species i, Pa
f_t total fugacity of bulk fluid mixture, Pa
G^{excess} excess Gibbs free energy, J mol^{-1}
n number of species in the mixture, dimensionless
P_i^0 sorption pressure, Pa
q_i molar loading of species i, mol kg^{-1}
q_t total molar loading of mixture, mol kg^{-1}
R gas constant, 8.314 J mol^{-1} K^{-1}
S_{ads} adsorption selectivity, dimensionless
S_{diff} diffusion selectivity, dimensionless
S_{perm} permeation selectivity, dimensionless
T absolute temperature, K
x_i mole fraction of species i in the adsorbed phase, dimensionless
y_i mole fraction of species i in the bulk fluid mixture, dimensionless

Greek alphabet

γ_i activity coefficient of component i in the adsorbed phase, dimensionless
π spreading pressure, N m^{-1}

REFERENCES

(1) Peng, P.; Shi, B.; Lan, Y. A Review of Membrane Materials for Ethanol Recovery by Pervaporation. *Sep. Sci. Technol.* **2011**, *46*, 234−246.
(2) Sato, K.; Aoki, K.; Sugimoto, K.; Izumi, K.; Inoue, S.; Saito, J.; Ikeda, S.; Nakane, T. Dehydrating performance of commercial LTA zeolite membranes and application to fuel grade bio-ethanol production by hybrid distillation/vapor permeation process. *Microporous Mesoporous Mater.* **2008**, *115*, 184−188.
(3) Sato, K.; Sugimoto, K.; Shimotsuma, N.; Kikuchi, T.; Kyotani, T.; Kurata, T. Development of practically available up-scaled high-silica CHA-type zeolite membranes for industrial purpose in dehydration of N-methyl pyrrolidone solution. *J. Membr. Sci.* **2012**, *409-410*, 82−95.
(4) Krishna, R. Highlighting Thermodynamic Coupling Effects in Alcohol/Water Pervaporation across Polymeric Membranes. *ACS Omega* **2019**, *4*, 15255−15264.
(5) Krishna, R.; van Baten, J. M. Investigating the Influence of Diffusional Coupling on Mixture Permeation across Porous Membranes. *J. Membr. Sci.* **2013**, *430*, 113−128.
(6) Hasegawa, Y.; Abe, C.; Nishioka, M.; Sato, K.; Nagase, T.; Hanaoka, T. Formation of high flux CHA-type zeolite membranes and their application to the dehydration of alcohol solutions. *J. Membr. Sci.* **2010**, *364*, 318−324.
(7) Kuhn, J.; Castillo-Sanchez, J. M.; Gascon, J.; Calero, S.; Dubbeldam, D.; Vlugt, T. J. H.; Kapteijn, F.; Gross, J. Adsorption and Diffusion of Water, Methanol, and Ethanol in All-Silica DD3R: Experiments and Simulation. *J. Phys. Chem. C* **2009**, *113*, 14290−14301.
(8) Kuhn, J.; Yajima, K.; Tomita, T.; Gross, J.; Kapteijn, F. Dehydration performance of a hydrophobic DD3R zeolite membrane. *J. Membr. Sci.* **2008**, *321*, 344−349.
(9) Pera-Titus, M.; Fité, C.; Sebastián, V.; Lorente, E.; Llorens, J.; Cunill, F. Modeling Pervaporation of Ethanol/Water Mixtures within 'Real' Zeolite NaA Membranes. *Ind. Eng. Chem. Res.* **2008**, *47*, 3213−3224.
(10) Yu, M.; Falconer, J. L.; Noble, R. D.; Krishna, R. Modeling Transient Permeation of Polar Organic Mixtures through a MFI Zeolite Membrane using the Maxwell-Stefan Equations. *J. Membr. Sci.* **2007**, *293*, 167−173.
(11) Mittal, N.; Bai, P.; Siepmann, J. I.; Daoutidis, P.; Tsapatsis, M. Bioethanol Enrichment using Zeolite Membranes: Molecular Modeling, Conceptual Process Design and Techno-Economic Analysis. *J. Membr. Sci.* **2017**, *540*, 464−476.
(12) Yao, J.; Wang, H. Zeolitic Imidazolate Framework Composite Membranes and Thin Films: Synthesis and Applications. *Chem. Soc. Rev.* **2014**, *43*, 4470−4493.
(13) Krishna, R.; van Baten, J. M. In Silico Screening of Zeolite Membranes for CO_2 Capture. *J. Membr. Sci.* **2010**, *360*, 323−333.
(14) Krishna, R.; van Baten, J. M. In silico screening of metal-organic frameworks in separation applications. *Phys. Chem. Chem. Phys.* **2011**, *13*, 10593−10616.
(15) Krishna, R. Thermodynamic Insights into the Characteristics of Unary and Mixture Permeances in Microporous Membranes. *ACS Omega* **2019**, *4*, 9512−9521.
(16) Krishna, R. The Maxwell-Stefan Description of Mixture Diffusion in Nanoporous Crystalline Materials. *Microporous Mesoporous Mater.* **2014**, *185*, 30−50.
(17) Morigami, Y.; Kondo, M.; Abe, J.; Kita, H.; Okamoto, K. The First Large-scale Pervaporation Plant Using Tubular-type Module with Zeolite NaA Membrane. *Sep. Purif. Technol.* **2001**, *25*, 251−260.
(18) Zhang, K.; Lively, R. P.; Zhang, C.; Koros, W. J.; Chance, R. R. Investigating the Intrinsic Ethanol/Water Separation Capability of ZIF-8: An Adsorption and Diffusion Study. *J. Phys. Chem. C* **2013**, *117*, 7214−7225.
(19) Remi, J. C. S.; Rémy, T.; van Huskeren, V.; van de Perre, S.; Duerinck, T.; Maes, M.; De Vos, D. E.; Gobechiya, E.; Kirschhock, C. E. A.; Baron, G. V.; Denayer, J. F. M. Biobutanol Separation with the Metal−Organic Framework ZIF-8. *ChemSusChem* **2011**, *4*, 1074−1077.
(20) Claessens, B.; Martin-Calvo, A.; Gutiérrez-Sevillano, J. J.; Dubois, N.; Denayer, J. F. M.; Cousin-Saint-Remi, J. Macroscopic and Microscopic View of Competitive and Cooperative Adsorption of Alcohol Mixtures on ZIF-8. *Langmuir* **2019**, *35*, 3887−3896.
(21) Lively, R. P.; Dose, M. E.; Thompson, J. A.; McCool, B. A.; Chance, R. R.; Koros, W. J. Ethanol and Water Adsorption in Methanol-derived ZIF-71. *Chem. Commun.* **2011**, *47*, 8667−8669.
(22) Xie, L.-H.; Xu, M.-M.; Liu, X.-M.; Zhao, M.-J.; Li, J.-R. Hydrophobic Metal−Organic Frameworks: Assessment, Construction, and Diverse Applications. *Adv. Sci.* **2020**, *7*, 1901758.
(23) Myers, A. L.; Prausnitz, J. M. Thermodynamics of Mixed-Gas Adsorption. *AIChE J.* **1965**, *11*, 121−127.
(24) Krishna, R. Separating Mixtures by Exploiting Molecular Packing Effects in Microporous Materials. *Phys. Chem. Chem. Phys.* **2015**, *17*, 39−59.
(25) Motkuri, R. K.; Thallapally, P. K.; Annapureddy, H. V. R.; Dang, L. X.; Krishna, R.; Nune, S. K.; Fernandez, C. A.; Liu, J.; McGrail, B. P. Separation of Polar Compounds using a Flexible Metal-Organic Framework. *Chem. Commun.* **2015**, *51*, 8421−8424.
(26) Plessius, R.; Kromhout, R.; Ramos, A. L. D.; Ferbinteanu, M.; Mittelmeijer-Hazeleger, M. C.; Krishna, R.; Rothenberg, G.; Tanase, S. Highly Selective Water Adsorption in a Lanthanum Metal-Organic Framework. *Chem. − Eur. J.* **2014**, *20*, 7922−7925.
(27) He, C.-T.; Jiang, L.; Ye, Z.-M.; Krishna, R.; Zhong, Z.-S.; Liao, P.-Q.; Xu, J.; Ouyang, G.; Zhang, J.-P.; Chen, X.-M. Exceptional hydrophobicity of a large-pore metal-organic zeolite. *J. Am. Chem. Soc.* **2015**, *137*, 7217−7223.
(28) Krishna, R. Metrics for Evaluation and Screening of Metal-Organic Frameworks for Applications in Mixture Separations. *ACS Omega* **2020**, *5*, 16987−17004.
(29) Krishna, R. Screening Metal-Organic Frameworks for Mixture Separations in Fixed-Bed Adsorbers using a Combined Selectivity/Capacity Metric. *RSC Adv.* **2017**, *7*, 35724−35737.
(30) Xiong, R.; Sandler, S. I.; Vlachos, D. G. Alcohol Adsorption onto Silicalite from Aqueous Solution. *J. Phys. Chem. C* **2011**, *115*, 18659−18669.
(31) Bai, P.; Tsapatsis, M.; Siepmann, J. I. Multicomponent Adsorption of Alcohols onto Silicalite-1 from Aqueous Solution: Isotherms, Structural Analysis, and Assessment of Ideal Adsorbed Solution Theory. *Langmuir* **2012**, *28*, 15566−15576.
(32) Farzaneh, A.; DeJaco, R. F.; Ohlin, L.; Holmgren, A.; Siepmann, J. I.; Grahn, M. Comparative Study of the Effect of Defects on Selective

https://dx.doi.org/10.1021/acsomega.0c04491
ACS Omega 2020, 5, 28393−28402

Adsorption of Butanol from Butanol/Water Binary Vapor Mixtures in Silicalite-1 Films. *Langmuir* **2017**, *33*, 8420−8427.
(33) Gómez-Álvarez, P.; Noya, E. G.; Lomba, E.; Valencia, S.; Pires, J. Study of Short-Chain Alcohol and Alcohol−Water Adsorption in MEL and MFI Zeolites. *Langmuir* **2018**, *34*, 12739−12750.
(34) Farzaneh, A.; Zhou, M.; Potapova, E.; Bacsik, Z.; Ohlin, L.; Holmgren, A.; Hedlund, J.; Grahn, M. Adsorption of Water and Butanol in Silicalite-1 Film Studied with *in Situ* Attenuated Total Reflectance−Fourier Transform Infrared Spectroscopy. *Langmuir* **2015**, *31*, 4887−4894.
(35) Krishna, R.; van Baten, J. M. Hydrogen Bonding Effects in Adsorption of Water-alcohol Mixtures in Zeolites and the Consequences for the Characteristics of the Maxwell-Stefan Diffusivities. *Langmuir* **2010**, *26*, 10854−10867.
(36) Krishna, R.; van Baten, J. M.; Baur, R. Highlighting the Origins and Consequences of Thermodynamic Nonidealities in Mixture Separations using Zeolites and Metal-Organic Frameworks. *Microporous Mesoporous Mater.* **2018**, *267*, 274−292.
(37) Krishna, R.; van Baten, J. M. Highlighting Pitfalls in the Maxwell-Stefan Modeling of Water-Alcohol Mixture Permeation across Pervaporation Membranes. *J. Membr. Sci.* **2010**, *360*, 476−482.
(38) Krishna, R.; van Baten, J. M. A comparison of the CO_2 capture characteristics of zeolites and metal-organic frameworks. *Sep. Purif. Technol.* **2012**, *87*, 120−126.
(39) Frenkel, D.; Smit, B. *Understanding Molecular Simulations: From Algorithms to Applications*; 2nd Edition, Elsevier: 2001.
(40) Smit, B.; Krishna, R. Molecular simulations in zeolitic process design. *Chem. Eng. Sci.* **2003**, *58*, 557−568.
(41) Vlugt, T. J. H.; Krishna, R.; Smit, B. Molecular Simulations of Adsorption Isotherms for Linear and Branched Alkanes and Their Mixtures in Silicalite. *J. Phys. Chem. B* **1999**, *103*, 1102−1118.
(42) Krishna, R.; van Baten, J. M. Mutual slowing-down effects in mixture diffusion in zeolites. *J. Phys. Chem. C* **2010**, *114*, 13154−13156.
(43) Rick, S. W. A Reoptimization of the Five-site Water Potential (TIP5P) for use with Ewald Sums. *J. Chem. Phys.* **2004**, *120*, 6085−6093.
(44) Chen, B.; Potoff, J. J.; Siepmann, J. I. Monte Carlo Calculations for Alcohols and Their Mixtures with Alkanes. Transferable Potentials for Phase Equilibria. 5. United-Atom Description of Primary, Secondary, and Tertiary Alcohols. *J. Phys. Chem. B* **2001**, *105*, 3093−3104.
(45) Krishna, R.; Van Baten, J. M. Using Molecular Simulations for Elucidation of Thermodynamic Non-Idealities in Adsorption of CO_2-containing Mixtures in NaX Zeolite. *ACS Omega* **2020**, *5*, 20535−20542.
(46) Krishna, R.; Van Baten, J. M. Investigating the Non-idealities in Adsorption of CO_2-bearing Mixtures in Cation-exchanged Zeolites. *Sep. Purif. Technol.* **2018**, *206*, 208−217.
(47) Krishna, R. Elucidation and Characterization of Entropy Effects in Mixture Separations with Micro-porous Crystalline Adsorbents. *Sep. Purif. Technol.* **2019**, *215*, 227−241.
(48) Krishna, R.; Van Baten, J. M. Elucidation of Selectivity Reversals for Binary Mixture Adsorption in Microporous Adsorbents. *ACS Omega* **2020**, *5*, 9031−9040.
(49) Zhang, C.; Yang, X. Molecular dynamics simulation of ethanol/water mixtures for structure and diffusion properties. *Fluid Phase Equilib.* **2005**, *231*, 1−10.
(50) Gutiérrez-Sevillano, J. J.; Calero, S.; Krishna, R. Selective Adsorption of Water from Mixtures with 1-Alcohols by Exploitation of Molecular Packing Effects in CuBTC. *J. Phys. Chem. C* **2015**, *119*, 3658−3666.
(51) Gutiérrez-Sevillano, J. J.; Calero, S.; Krishna, R. Separation of Benzene from Mixtures with Water, Methanol, Ethanol, and Acetone: Highlighting Hydrogen Bonding and Molecular Clustering Influences in CuBTC. *Phys. Chem. Chem. Phys.* **2015**, *17*, 20114−20124.
(52) Nalaparaju, A.; Zhao, X. S.; Jiang, J. W. Molecular Understanding for the Adsorption of Water and Alcohols in Hydrophilic and Hydrophobic Zeolitic Metal-Organic Frameworks. *J. Phys. Chem. C* **2010**, *114*, 11542−11550.
(53) Arletti, R.; Vezzalini, G.; Quartieri, S.; Di Renzo, F.; Dmitriev, V. Pressure-induced water intrusion in FER-type zeolites and the influence of extraframework species on structural deformations. *Microporous Mesoporous Mater.* **2014**, *191*, 27−37.
(54) Confalonieri, G.; Quartieri, S.; Vezzalini, G.; Tabacchi, G.; Fois, E.; Daou, T. J.; Arletti, R. Differential penetration of ethanol and water in Si-chabazite: High pressure dehydration of azeotrope solution. *Microporous Mesoporous Mater.* **2019**, *284*, 161−169.
(55) Krishna, R.; van Baten, J. M. Maxwell-Stefan modeling of slowing-down effects in mixed gas permeation across porous membranes. *J. Membr. Sci.* **2011**, *383*, 289−300.
(56) Krishna, R. Diffusion in Porous Crystalline Materials. *Chem. Soc. Rev.* **2012**, *41*, 3099−3118.
(57) Krishna, R. Thermodynamically Consistent Methodology for Estimation of Diffusivities of Mixtures of Guest Molecules in Microporous Materials. *ACS Omega* **2019**, *4*, 13520−13529.
(58) Krishna, R. Using the Maxwell-Stefan formulation for Highlighting the Influence of Interspecies (1-2) Friction on Binary Mixture Permeation across Microporous and Polymeric Membranes. *J. Membr. Sci.* **2017**, *540*, 261−276.
(59) Sakuth, M.; Meyer, J.; Gmehling, J. Vapor Phase Adsorption Equilibria of Toluene + 1-Propanol Mixtures on Y-Zeolites with Different Silicon to Aluminum Ratios. *J. Chem. Eng. Data* **1995**, *40*, 895−899.
(60) Van Assche, T. R. C.; Duerinck, T.; Van der Perre, S.; Baron, G. V.; Denayer, J. F. M. Prediction of Molecular Separation of Polar−Apolar Mixtures on Heterogeneous Metal−Organic Frameworks: HKUST-1. *Langmuir* **2014**, *30*, 7878−7883.
(61) Takeuchi, Y.; Iwamoto, H.; Miyata, N.; Asano, S.; Harada, M. Adsorption of l-butanol and p-xylene vapor with high silica zeolites. *Sep. Technol.* **1995**, *5*, 23−34.
(62) Talu, O.; Myers, A. L. Rigorous Thermodynamic Treatment of Gas Adsorption. *AIChE J.* **1988**, *34*, 1887−1893.
(63) Talu, O.; Zwiebel, I. Multicomponent Adsorption Equilibria of Nonideal Mixtures. *AIChE J.* **1986**, *32*, 1263−1276.
(64) Siperstein, F. R.; Myers, A. L. Mixed-Gas Adsorption. *AIChE J.* **2001**, *47*, 1141−1159.
(65) Sochard, S.; Fernandes, N.; Reneaume, J.-M. Modeling of Adsorption Isotherm of a Binary Mixture with Real Adsorbed Solution Theory and Nonrandom Two-Liquid Model. *AIChE J.* **2010**, *56*, 3109−3119.

https://dx.doi.org/10.1021/acsomega.0c04491
ACS Omega 2020, 5, 28393−28402

Supporting Information

Water/Alcohol Mixture Adsorption in Hydrophobic Materials: Enhanced Water Ingress caused by Hydrogen Bonding

Rajamani Krishna* and Jasper M. van Baten

Van 't Hoff Institute for Molecular Sciences
University of Amsterdam
Science Park 904
1098 XH Amsterdam, The Netherlands
email: r.krishna@contact.uva.nl

Table of Contents

1 Preamble 4

2 Structural Details and CBMC Methodology 5

2.1 Structural details of host materials and pore landscapes 5

2.2 Force fields and CBMC simulation methodology 7

2.3 List of Tables for Structural Details and CBMC Methodology 9

2.4 List of Figures for Structural Details and CBMC Methodology 11

3 IAST calculations of mixture adsorption 26

3.1 Brief outline of theory 26

3.2 Selectivity for binary mixture adsorption 29

4 The Real Adsorbed Solution Theory (RAST) 30

4.1 Margules model for activity coefficients 30

5 Radial Distribution Functions of O···H distances 32

5.1 List of Figures for Radial Distribution Functions of O···H distances 34

6 CBMC data for mixture adsorption and RAST analysis 42

6.1 CBMC simulation campaigns 42

6.2 Unary isotherm fit parameters 43

6.3 Determination of activity coefficients from CBMC mixture adsorption data 43

6.4 Determination of Margules fit parameters from mixture adsorption data 44

6.5 Summary of CBMC simulation data and comparison with RAST. 44

6.6 Summary of key features for mixture adsorption with hydrogen bonding. 47

6.7 Analysis of published experimental data 50

6.8 CBMC simulation campaigns for mixtures without hydrogen bonding 51

6.9 Summary of key features for mixture adsorption without hydrogen bonding. 51

6.10 List of Tables for CBMC data for mixture adsorption and RAST analysis 54

6.11 List of Figures for CBMC data for mixture adsorption and RAST analysis..... 71

7 Nomenclature 115

8 References 117

1 Preamble

This Supplementary material accompanying our manuscript *Water/Alcohol Mixture Adsorption in Hydrophobic Materials: Enhanced Water Ingress caused by Hydrogen Bonding* provides (a) structural details of zeolites, MOFs and ZIFs, (b) details of the CBMC simulation methodology, (b) details of the IAST, and Real Adsorbed Solution Theory (RAST) calculations for mixture adsorption equilibrium, (c) unary isotherm fits for all the guest/host combinations, (d) Margules parameter fits for thermodynamic non-idealities, (e) Plots of CBMC simulation data and comparisons with IAST/RAST estimates for all guest/host combinations.

.

2 Structural Details and CBMC Methodology

2.1 Structural details of host materials and pore landscapes

All-silica FAU (= faujasite) has cages of 786 $Å^3$ volume, separated by 7.3 Å 12-ring windows; see structural information in Figure S1, and Figure S2.

CHA zeolite (all-silica), consists of cages of volume 316 $Å^3$, separated by 3.8 Å × 4.2 Å 8-ring windows; the pore landscape and structural details are provided in Figure S3, and Figure S4.[1-4]

DDR consists of cages of 277.8 $Å^3$ volume, separated by 3.65 Å × 4.37 Å 8-ring windows; the pore landscapes and structural details are provided in Figure S5, and Figure S6. The DDR structure is an orthorhombic reconstruction of the monoclinic geometry in the original paper of Gies[5], using larger unit cell dimensions.

MFI zeolite (also called silicalite-1) has a topology consisting of a set of intersecting straight channels, and zig-zag (or sinusoidal) channels of approximately 5.5 Å size. The pore landscapes and structural details are provided in Figure S7, and Figure S8. For MFI, our structural parameters correspond to those reported by van Koningsveld[6].

ZIF-8 ($Zn(MeIm)_2$, MeIm = 2-methylimidazole) has a cage-window SOD (sodalite) topology with large cavities (≈ 11.6 Å) interconnected by small six-ring-openings (≈ 3.3 Å) (see pore landscapes in Figure S9, and Figure S10). Though the crystallographic size of the windows of ZIF-8 is 3.3 Å, the windows are flexible.

ZIF-71 possess a three-dimensional pore network formed by large cages interconnected via small windows;[7] see pore landscapes in Figure S11.

CuBTC (= $Cu_3(BTC)_2$ with BTC = 1,3,5-benzenetricarboxylate, also known as HKUST-1) framework is composed of copper atoms connected by benzene-1,3,5-tricarboxylate (BTC) linkers, which form a

characteristic paddle-wheel structure: two copper atoms bonded to the oxygen atoms of four BTC linkers, generating four-connected square-planar vertexes; see Figure S12, and Figure S13.

The structural information for CuBTC simulations have been taken from Chui et al.[8] and Yang and Zhong.[9] The crystal structure of Chui et al. [8] includes axial oxygen atoms weakly bonded to the Cu atoms, which correspond to water ligands; our simulations have been performed on the dry CuBTC with these oxygen atoms removed.

The framework contains two types of large cavities (9 Å diameter) and small cavities (of 5 Å diameter). The larger cavities (L_2 and L_3) are similar in size and shape but as a result of the paddle-wheel, the copper atoms are only accessible from the L_3 cages. L_2 and L_3 cavities are connected through triangular-shaped windows. The small cavities (T_1) are tetrahedral pockets enclosed by the benzene rings; these are connected to L_3 cages by small triangular windows (3.5 Å in size), as shown in Figure S14.

The CuBTC framework is composed of copper atoms connected by benzene-1,3,5-tricarboxylate (BTC) linkers, which form a characteristic paddle-wheel structure: two copper atoms bonded to the oxygen atoms of four BTC linkers, generating four-connected square-planar vertexes. The framework contains two types of large cavities (9 Å diameter) and small cavities (of 5 Å diameter). The larger cavities (L_2 and L_3) are similar in size and shape but as a result of the paddle-wheel, the copper atoms are only accessible from the L_3 cages. L_2 and L_3 cavities are connected by windows. The small cavities (T_1) are tetrahedral pockets enclosed by the benzene rings. They are connected to L_3 cages by small triangular windows as shown in Figure S12, Figure S13, and Figure S14. The tetrahedral pockets can accommodate about 9 molecules of water, but only about 1 molecule of 1-propanol.

2.2 Force fields and CBMC simulation methodology

For simulations of adsorption of guest molecules water, methanol, and ethanol, the force field implementation follows earlier publications.[10-13] Water is modeled using the Tip5pEw potential.[14] The alcohols are described with the TraPPE force field.[15] Intramolecular potentials are included to describe the flexibility of alcohols, while the water molecules are kept rigid. The bond lengths are fixed for all molecules. Bond bending potentials are considered for methanol and ethanol, and a torsion potential is used for ethanol.[15] The force field parameters are summarized in Table S1.

Following Kiselev and co-workers,[16] the zeolite is modeled as a rigid crystal. The interactions of the guest (pseudo) atoms with the host zeolite atoms aredominated by the dispersive interactions with the oxygen atoms, these interactions are described with a Lennard-Jones potential; see Table S2.

ZIF-8 is also modelled as a rigid structure. The Lennard-Jones potentials for the framework atoms of ZIF-8 were taken from the combined works of Mayo et al.[17], Yang and Zhong [18], and Jorgensen et al.[19] as was reported in the computational study of Zhou et al.[20] The framework charges of ZIF-8 were estimated using the group-contribution procedure based on quantum mechanical calculations described in the recent paper by Xu and Zhong.[21] Table S3 provides a summary of the force fields for ZIF-8 framework atoms.

The Lorentz-Berthelot mixing rules were applied for calculating the Lennard-Jones parameters describing guest-host interactions

$$\sigma_{guest-host} = \frac{\left(\sigma_{guest} + \sigma_{host}\right)}{2}$$
$$\frac{\varepsilon_{guest-host}}{k_B} = \sqrt{\frac{\varepsilon_{guest}}{k_B} \times \frac{\varepsilon_{host}}{k_B}} \qquad \text{(S1)}$$

The Lennard-Jones potentials are shifted and cut at 12 Å. Periodic boundary conditions were employed. The Configurational-Bias Monte Carlo (CBMC) simulation technique used is identical to that used by Kuhn et al.,[13] and is described in detail by Frenkel and Smit.[22] The CBMC simulations were performed using the BIGMAC code developed by T.J.H. Vlugt[23] as basis.

Structural Details and CBMC Methodology

Additionally, we present a re-analysis of the CBMC simulations of Nalaparaju et al.[7] for water/methanol and water/ethanol mixture adsorption in ZIF-71 at 298 K. Also included in the simulations are re-analyses of CBMC data for polar guests in CuBTC as provided in our earlier works, wherein the force fields are specified.[24, 25]

2.3 List of Tables for Structural Details and CBMC Methodology

Table S1. Lennard-Jones parameters for guest pseudo-atoms. as provided in Table 1 of Kuhn et al.[13] The water model has two off-center charges that are labeled M in the Table. The name "alcohol" refers to both methanol and ethanol molecules.

Molecule	(pseudo-) atom	σ / Å	ε/k_B / K	charge
water	O	3.097	89.516	0
water	H	0	0	0.241
water	M	0	0	-0.241
methanol	CH3	3.75	98	0.265
ethanol	CH3	3.75	98	0
ethanol	CH2	3.95	46	0.265
alcohol	O	3.02	93	-0.7
alcohol	H	0	0	0.435

Table S2. Lennard-Jones parameters for host atoms in all-silica zeolites.

(pseudo-) atom	σ / Å	ε/k_B / K	charge
Si			2.05
O	3	93.53	-1.025

Table S3. The Lennard-Jones potentials for the host framework atoms of ZIF-8 were taken from the combined works of Mayo et al.[17] Yang and Zhong,[18] and Jorgensen et al.[19] as was reported in the computational study of Zhou et al.[20] The framework charges of ZIF-8 were estimated using the group-contribution procedure based on quantum mechanical calculations described by Xu and Zhong.[21]

(pseudo-) atom	σ / Å	ε/k_B / K	charge
Zn	4.54	27.59	0.749
N	3.25	85.29	-0.387
Ca	2.25	25.08	0.698
Cb	3.55	35.12	-0.0093
Cc	3.5	20.03	0.0117
Ha	2.5	15.05	-0.139
Hb	3.19	7.53	0.0627

See Cartoon below for further explanation:

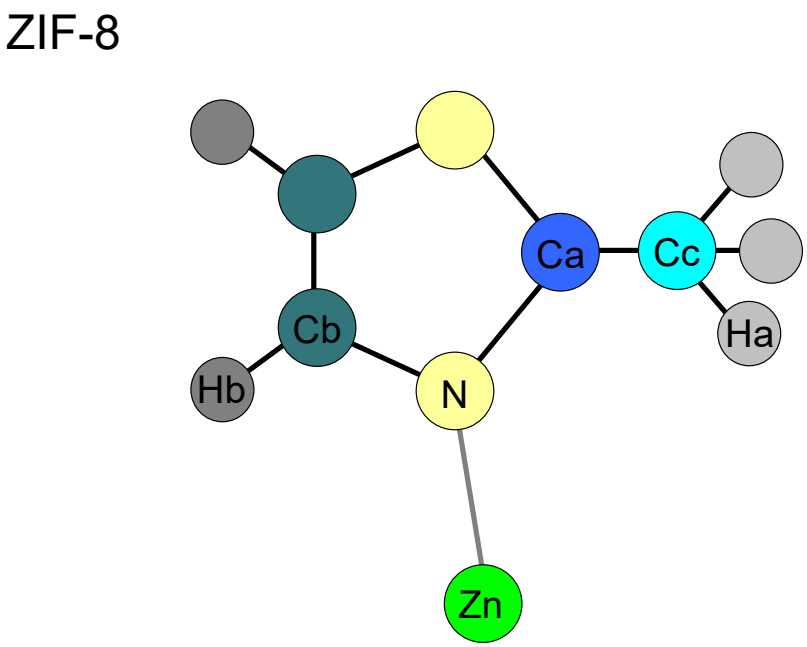

2.4 List of Figures for Structural Details and CBMC Methodology

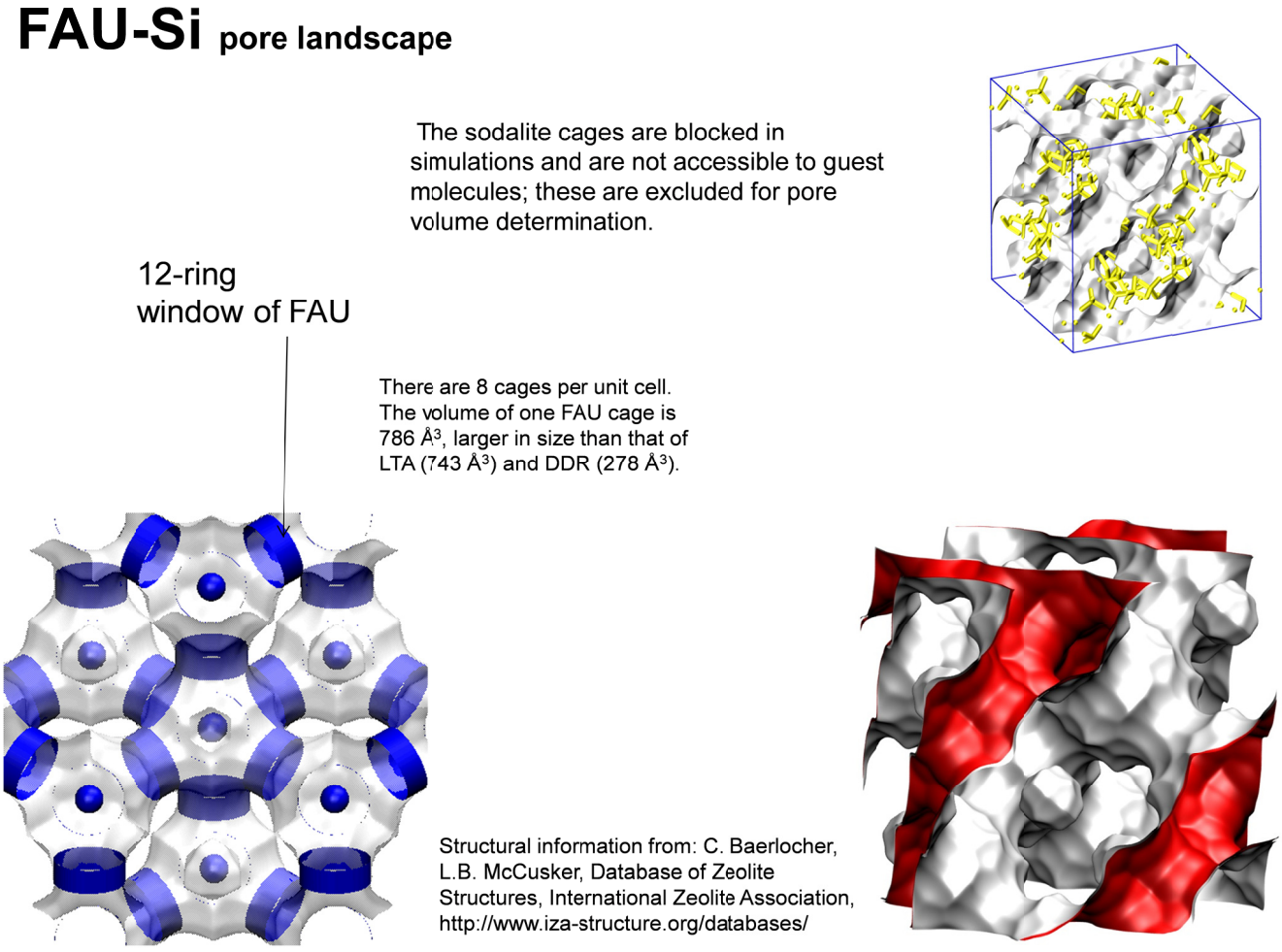

Figure S1. Pore landscape of all-silica FAU zeolite.

FAU-Si window and pore dimensions

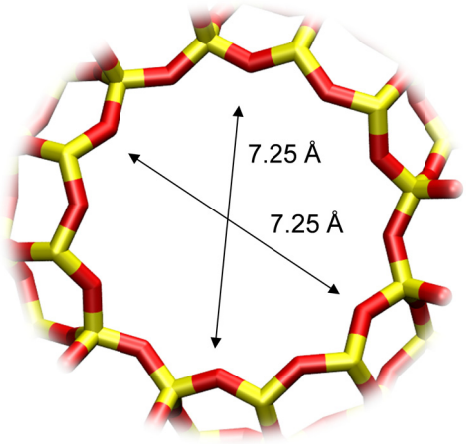

	FAU-Si
a /Å	24.28
b /Å	24.28
c /Å	24.28
Cell volume / Å^3	14313.51
conversion factor for [molec/uc] to [mol per kg Framework]	0.0867
conversion factor for [molec/uc] to [kmol/m^3]	0.2642
ρ [kg/m3]	1338.369
MW unit cell [g/mol (framework)]	11536.28
ϕ, fractional pore volume	0.439
open space / Å^3/uc	6285.6
Pore volume / cm^3/g	0.328
Surface area /m^2/g	1086.0
DeLaunay diameter /Å	7.37

Figure S2. Structural details for FAU zeolite.

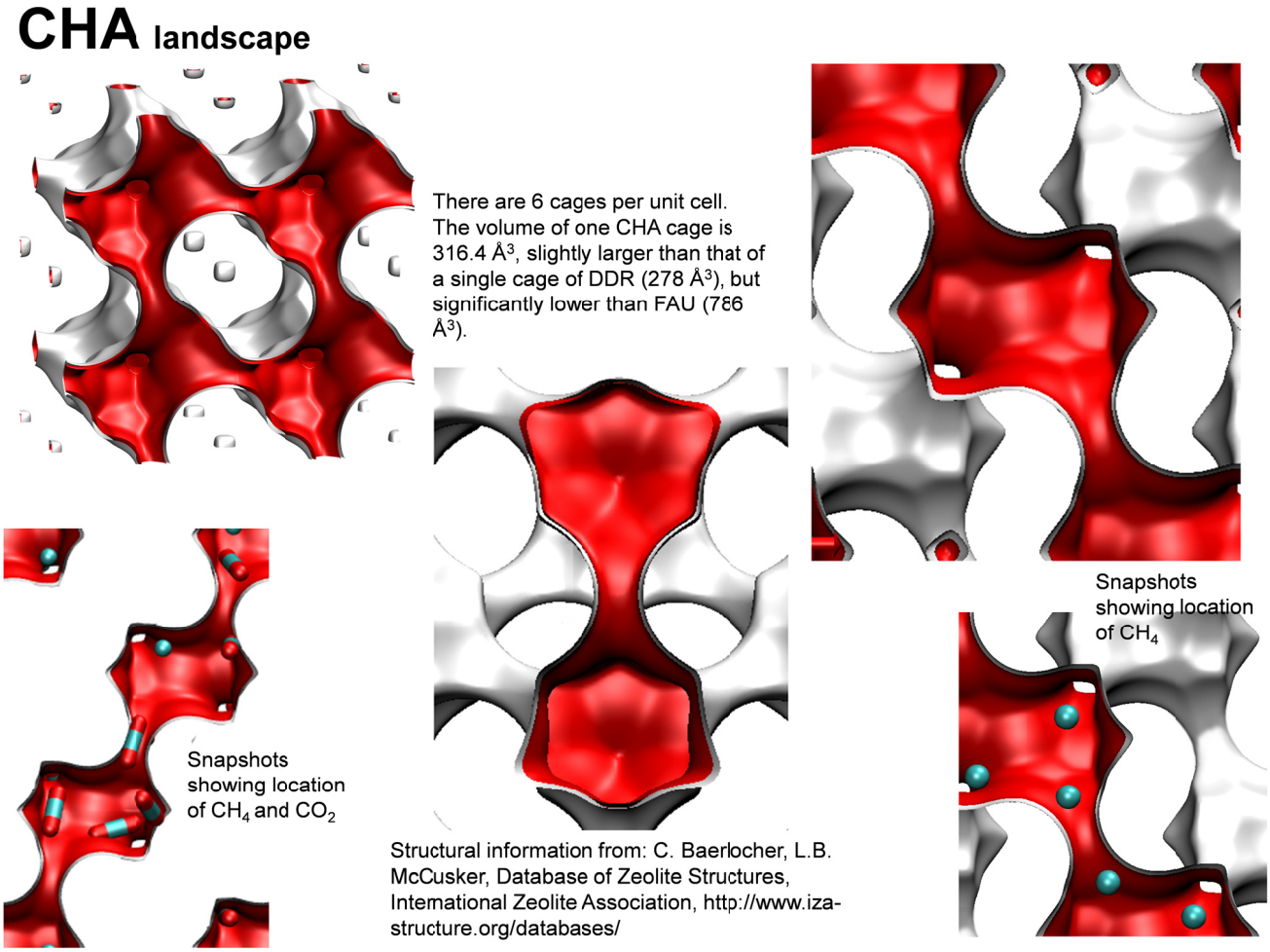

Figure S3. Pore landscape and structural details of all-silica CHA zeolite, also called SiCHA.

CHA window and pore dimensions

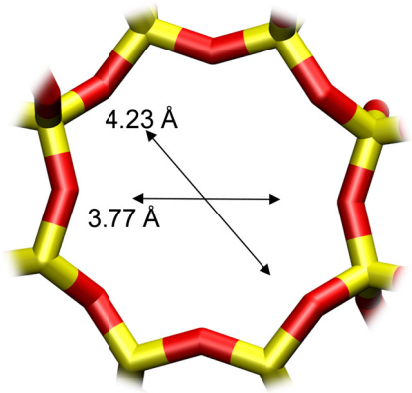

CHA

The window dimensions calculated using the van der Waals diameter of framework atoms = 2.7 Å are indicated above by the arrows.

	CHA
a /Å	15.075
b /Å	23.907
c /Å	13.803
Cell volume / Å^3	4974.574
conversion factor for [molec/uc] to [mol per kg Framework]	0.2312
conversion factor for [molec/uc] to [kmol/m^3]	0.8747
ρ [kg/m3]	1444.1
MW unit cell [g/mol(framework)]	4326.106
ψ, fractional pore volume	0.382
open space / Å^3/uc	1898.4
Pore volume / cm^3/g	0.264
Surface area /m^2/g	758.0
DeLaunay diameter /Å	3.77

Figure S4. Pore landscape and structural details of all-silica CHA zeolite, also called SiCHA.

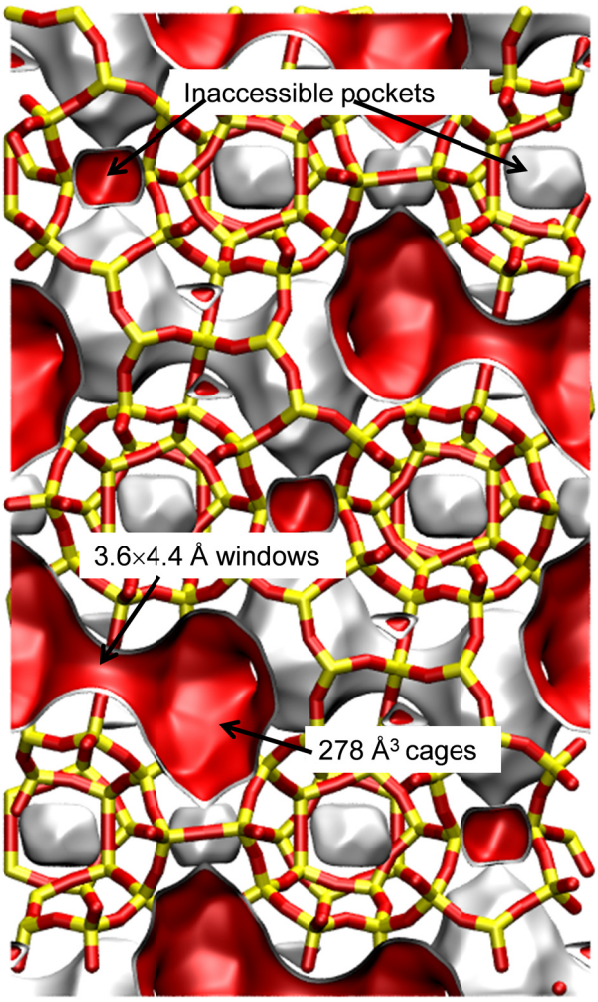

DDR landscape

To convert from molecules per unit cell to mol kg^{-1}, multiply by 0.06936.
The pore volume is 0.182 cm^3/g.

There are 12 cages per unit cell. The volume of one DDR cage is 278 Å^3, significantly smaller than that of a single cage of FAU (786 Å^3), or ZIF-8 (1168 Å^3).

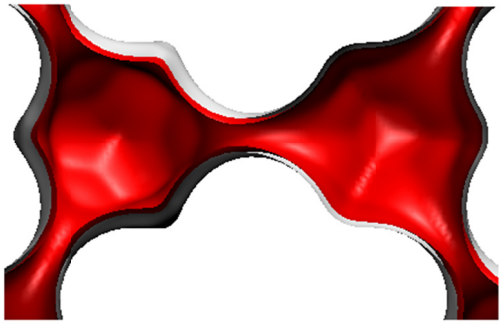

Structural information from: C. Baerlocher, L.B. McCusker, Database of Zeolite Structures, International Zeolite Association, http://www.iza-structure.org/databases/

Figure S5. Pore landscape of all-silica DDR zeolite.

DDR window and pore dimensions

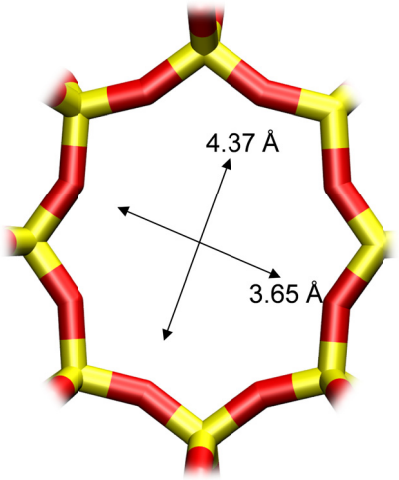

DDR

The window dimensions calculated using the van der Waals diameter of framework atoms = 2.7 Å are indicated above by the arrows.

	DDR
a /Å	24.006
b /Å	13.86
c /Å	40.892
Cell volume / Å^3	13605.72
conversion factor for [molec/uc] to [mol per kg Framework]	0.0693
conversion factor for [molec/uc] to [kmol/m^3]	0.4981
ρ [kg/m3]	1759.991
MW unit cell [g/mol(framework)]	14420.35
ϕ, fractional pore volume	0.245
open space / Å^3/uc	3333.5
Pore volume / cm^3/g	0.139
Surface area /m^2/g	350.0
DeLaunay diameter /Å	3.65

Figure S6. Structural details for DDR zeolite.

MFI pore landscape

	MFI
a /Å	20.022
b /Å	19.899
c /Å	13.383
Cell volume / Å^3	5332.025
conversion factor for [molec/uc] to [mol per kg Framework]	0.1734
conversion factor for [molec/uc] to [kmol/m^3]	1.0477
ρ [kg/m3]	1796.386
MW unit cell [g/mol(framework)]	5768.141
ϕ, fractional pore volume	0.297
open space / Å^3/uc	1584.9
Pore volume / cm^3/g	0.165
Surface area /m^2/g	487.0
DeLaunay diameter /Å	5.16

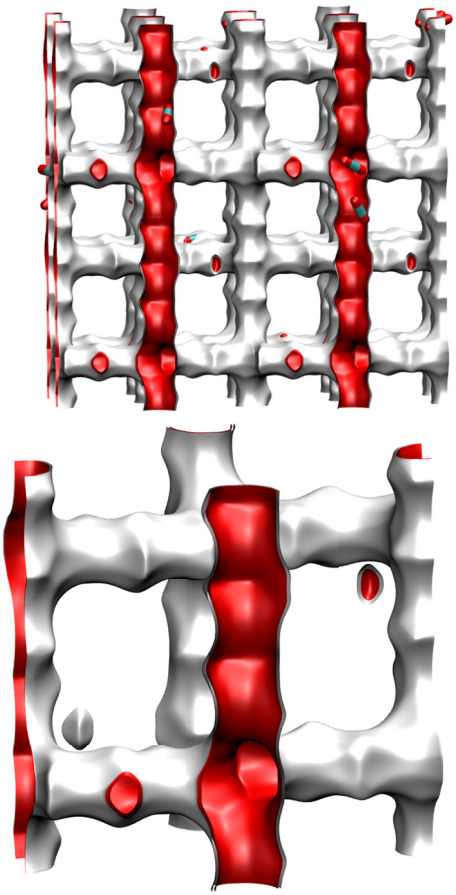

Figure S7. Structural details and pore landscape for MFI zeolite.

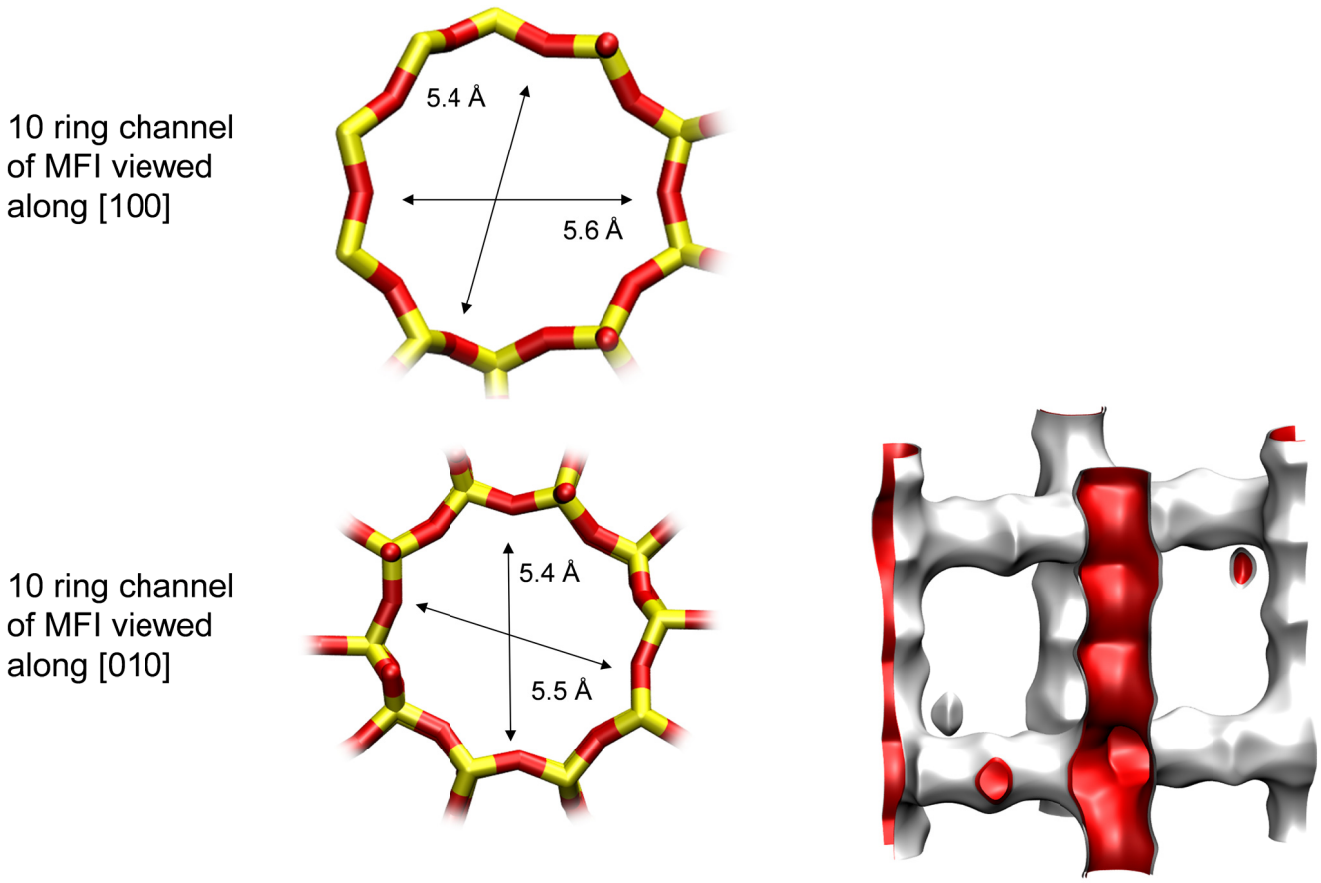

Figure S8. Structural details and pore landscape for MFI zeolite.

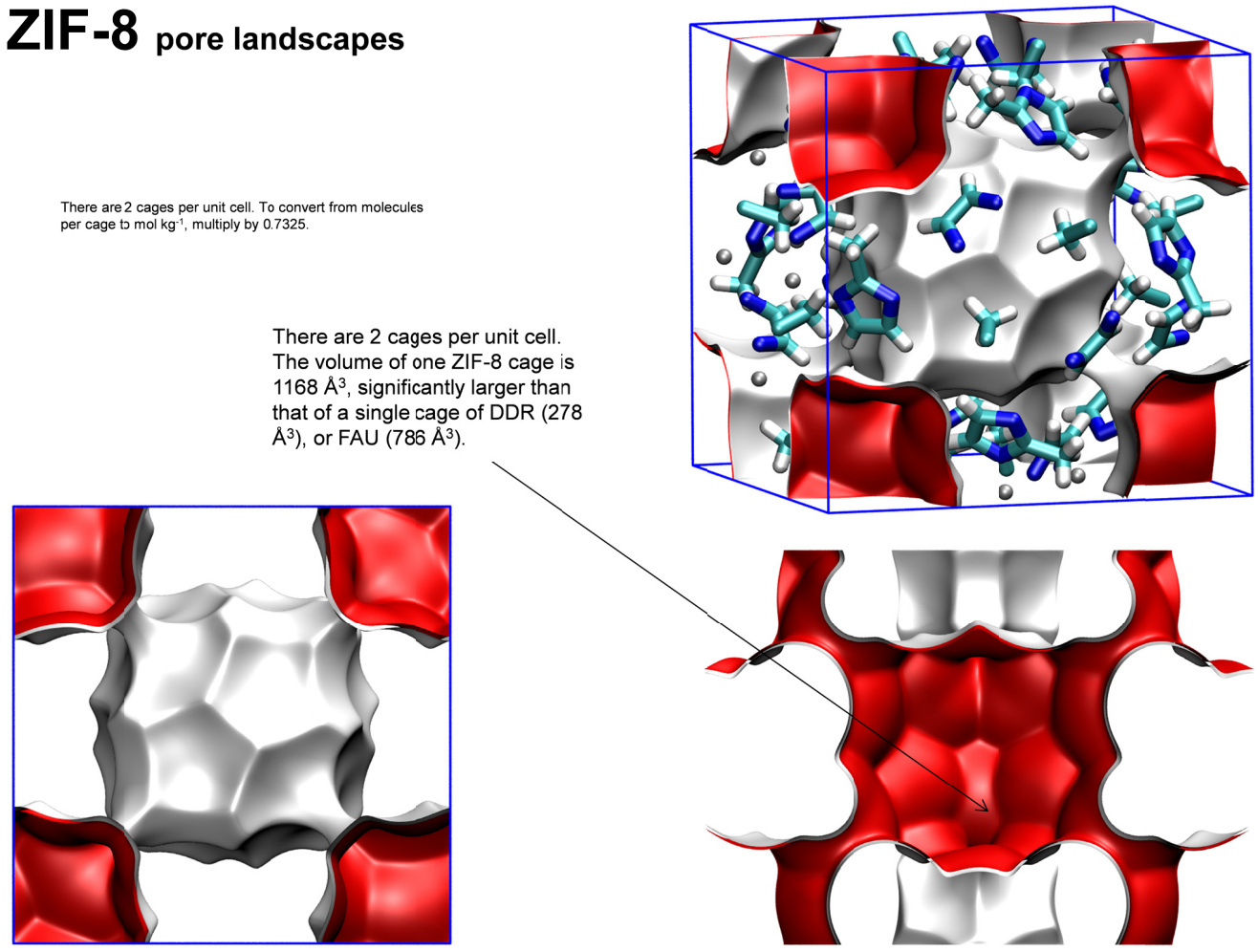

Figure S9. Pore landscape and structural details of ZIF-8.

ZIF-8 dimensions

	ZIF-8
a /Å	16.991
b /Å	16.991
c /Å	16.991
Cell volume / Å^3	4905.201
conversion factor for [molec/uc] to [mol per kg Framework]	0.3663
conversion factor for [molec/uc] to [kmol/m^3]	0.7106
ρ [kg/m3]	924.253
MW unit cell [g/mol(framework)]	2730.182
ϕ, fractional pore volume	0.476
open space / Å^3/uc	2337.0
Pore volume / cm^3/g	0.515
Surface area /m^2/g	1164.7
DeLaunay diameter /Å	3.26

Figure S10. Pore landscape and structural details of ZIF-8.

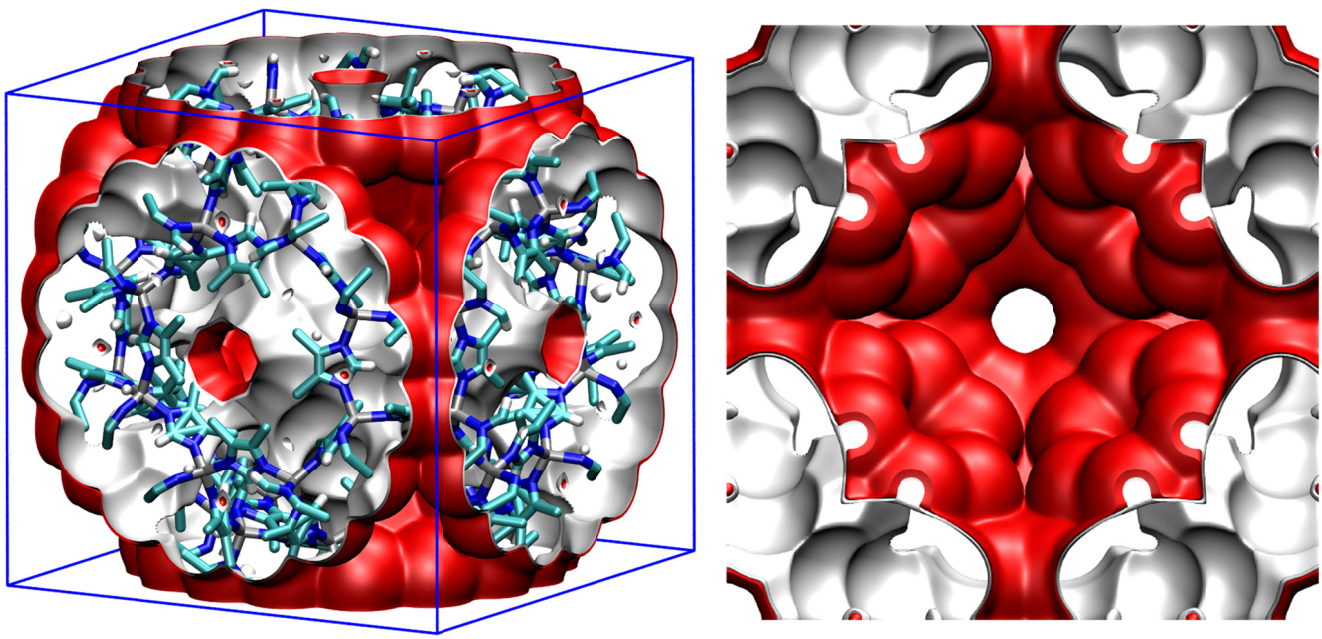

Figure S11. Pore landscape for ZIF-71.

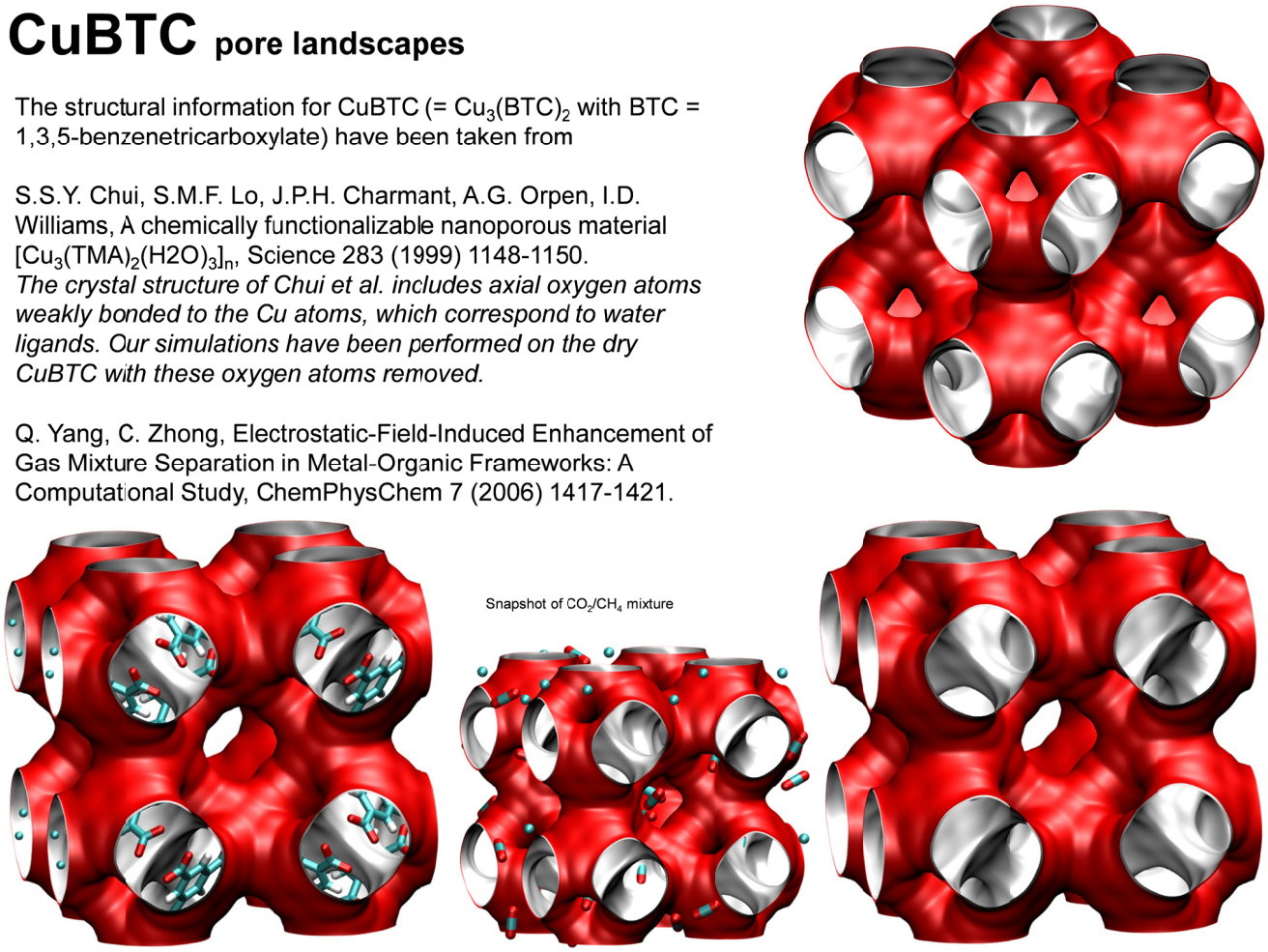

Figure S12. Structural details and pore landscape for CuBTC.

CuBTC pore dimensions

	CuBTC
a /Å	26.343
b /Å	26.343
c /Å	26.343
Cell volume / Å^3	18280.82
conversion factor for [molec/uc] to [mol per kg Framework]	0.1034
conversion factor for [molec/uc] to [kmol/m^3]	0.1218
ρ [kg/m3]	878.8298
MW unit cell [g/mol(framework)]	9674.855
ϕ, fractional pore volume	0.746
open space / Å^3/uc	13628.4
Pore volume / cm^3/g	0.848
Surface area /m^2/g	2097.0
DeLaunay diameter /Å	6.23

The CuBTC structure consists of two types of “cages” and two types of “windows” separating these cages. Large cages are inter-connected by 9 Å windows of square cross-section. The large cages are also connected to tetrahedral-shaped pockets of ca. 5 Å size through triangular-shaped windows of ca. 4.6 Å size

Figure S13. Structural details and pore landscape for CuBTC.

CuBTC framework

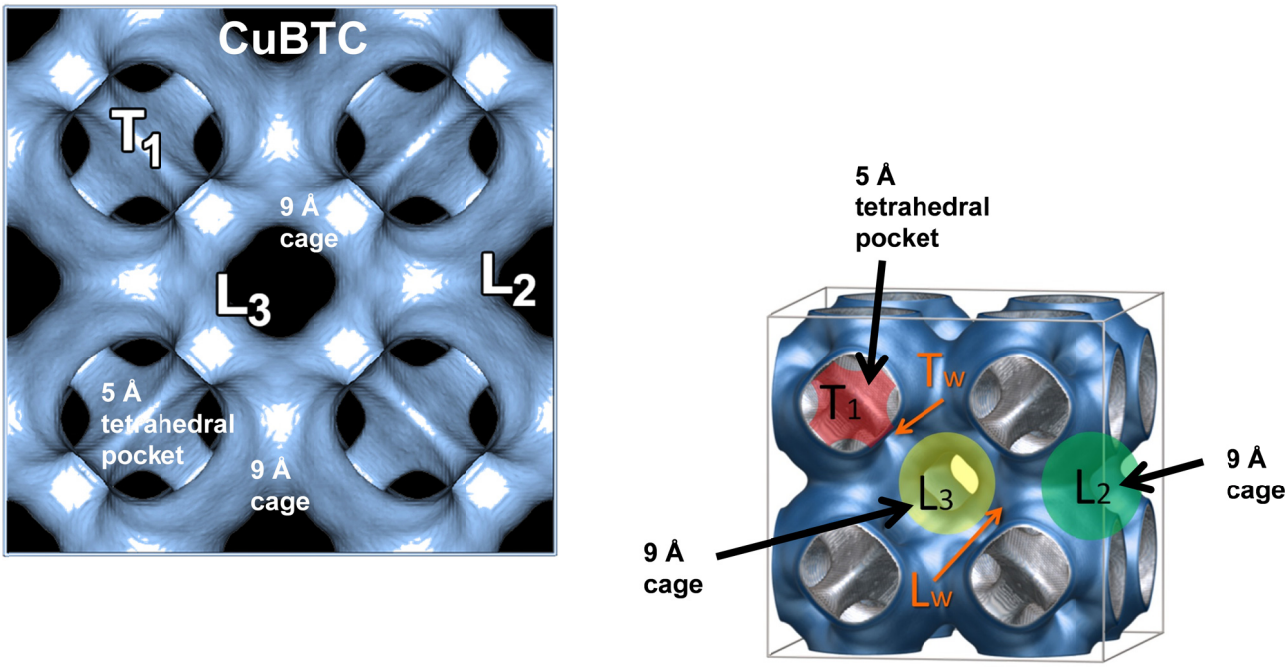

Figure S14. Structural details and pore landscape for CuBTC.

3 IAST calculations of mixture adsorption

3.1 Brief outline of theory

Within microporous crystalline materials such as zeolites and metal-organic frameworks (MOFs), the guest molecules exist in the adsorbed phase. The Gibbs adsorption equation[26] in differential form is

$$Ad\pi = \sum_{i=1}^{n} q_i d\mu_i \tag{S2}$$

The quantity A is the surface area per kg of framework, with units of m^2 per kg of the framework of the crystalline material; q_i is the molar loading of component i in the adsorbed phase with units moles per kg of framework; μ_i is the molar chemical potential of component i. The spreading pressure π has the same units as surface tension, i.e. N m^{-1}.

The chemical potential of any component in the adsorbed phase, μ_i, equals that in the bulk fluid phase. If the partial fugacities in the bulk fluid phase are f_i, we have

$$d\mu_i = RTd\ln f_i \tag{S3}$$

where R is the gas constant (= 8.314 J mol^{-1} K^{-1}).

Briefly, the basic equation of Ideal Adsorbed Solution Theory (IAST) theory of Myers and Prausnitz[27] is the analogue of Raoult's law for vapor-liquid equilibrium, i.e.

$$f_i = P_i^0 x_i; \quad i = 1,2,...n \tag{S4}$$

where x_i is the mole fraction in the adsorbed phase

$$x_i = \frac{q_i}{q_1 + q_2 + ...q_n} \tag{S5}$$

and P_i^0 is the pressure for sorption of every component i, which yields the same spreading pressure, π for each of the pure components, as that for the mixture:

IAST calculations of mixture adsorption

$$\frac{\pi A}{RT} = \int_0^{P_1^0} \frac{q_1^0(f)}{f} df = \int_0^{P_2^0} \frac{q_2^0(f)}{f} df = \int_0^{P_3^0} \frac{q_3^0(f)}{f} df = ... \tag{S6}$$

where $q_i^0(f)$ is the *pure* component adsorption isotherm. The units of $\frac{\pi A}{RT}$, also called the adsorption potential,[28] are mol kg^{-1}.

The unary isotherm may be described by say the 1-site Langmuir isotherm

$$q^0(f) = q_{sat} \frac{bf}{1+bf}; \quad \theta = \frac{bf}{1+bf} \tag{S7}$$

where we define the fractional *occupancy* of the adsorbate molecules, $\theta = q^0(f)/q_{sat}$. The superscript 0 is used to emphasize that $q^0(f)$ relates the *pure component* loading to the bulk fluid fugacity. More generally, the unary isotherms may need to be described by, say, the dual-site Langmuir-Freundlich model

$$q^0(f) = q_{A,sat} \frac{b_A f^{\nu_A}}{1+b_A f^{\nu_A}} + q_{B,sat} \frac{b_B f^{\nu_B}}{1+b_B f^{\nu_B}} \tag{S8}$$

Each of the integrals in Equation (S6) can be evaluated analytically:

$$\begin{aligned} \int_{f=0}^{P_i^0} \frac{q^0(f)}{f} df &= \frac{q_{A,sat}}{\nu_A} \ln\left(1+b_A\left(P_i^0\right)^{\nu_A}\right) + \frac{q_{B,sat}}{\nu_B} \ln\left(1+b_B\left(P_i^0\right)^{\nu_B}\right) \\ \int_{f=0}^{P_i^0} \frac{q^0(f)}{f} df &= \frac{q_{A,sat}}{\nu_A} \ln\left(1+b_A\left(\frac{f_i}{x_i}\right)^{\nu_A}\right) + \frac{q_{B,sat}}{\nu_B} \ln\left(1+b_B\left(\frac{f_i}{x_i}\right)^{\nu_B}\right) \end{aligned} \tag{S9}$$

The right hand side of eq (S9) is a function of P_i^0. For multicomponent mixture adsorption, each of the equalities on the right hand side of eq (S6) must be satisfied. These constraints may be solved using a suitable equation solver, to yield the set of values of P_1^0, P_2^0, P_3^0,.. P_n^0, all of which satisfy eq (S6). The corresponding values of the integrals using these as upper limits of integration must yield the same value of $\frac{\pi A}{RT}$ for each component; this ensures that the obtained solution is the correct one.

The adsorbed phase mole fractions x_i are then determined from eq (S4)

IAST calculations of mixture adsorption

$$x_i = \frac{f_i}{P_i^0}; \quad i = 1,2,...n \tag{S10}$$

The applicability of eqs (S4) and (S10) mandates that all of the adsorption sites within the microporous material are equally accessible to each of the guest molecules, implying a homogeneous distribution of guest adsorbates within the pore landscape, with no preferential locations of any guest species. The circumstances in which this mandate is not fulfilled are highlighted in recent works.[29-31]

A further key assumption of the IAST is that the enthalpies and surface areas of the adsorbed molecules do not change upon mixing. If the total mixture loading is q_t, the area covered by the adsorbed mixture is $\frac{A}{q_t}$ with units of m^2 (mole mixture)$^{-1}$. Therefore, the assumption of no surface area change due to mixture adsorption translates as $\frac{A}{q_t} = \frac{Ax_1}{q_1^0\left(P_1^0\right)} + \frac{Ax_2}{q_2^0\left(P_2^0\right)} + \cdots \frac{Ax_n}{q_n^0\left(P_n^0\right)}$; the total mixture loading is $q_t = q_1 + q_2 ... + q_n$ is calculated from

$$\frac{1}{q_t} = \frac{1}{\frac{x_1}{q_1^0(P_1^0)} + \frac{x_2}{q_2^0(P_2^0)} + ... + \frac{x_n}{q_n^0(P_n^0)}} \tag{S11}$$

in which $q_1^0(P_1^0)$, $q_2^0(P_2^0)$,… $q_n^0(P_n^0)$ are determined from the unary isotherm fits, using the sorption pressures for each component P_1^0, P_2^0, P_3^0 ,.. P_n^0 that are available from the solutions to Equations (S6), and (S9).

The occurrence of molecular clustering and hydrogen bonding should be expected to applicability of eq (S11) because the surface area occupied by a molecular cluster is different from that of each of the un-clustered guest molecules in the adsorbed phase.

The entire set of eqs (S4) to (S11) need to be solved numerically to obtain the loadings, q_i of the individual components in the mixture.

3.2 Selectivity for binary mixture adsorption

For binary mixtures consisting of components 1 (say water), and 2 (say ethanol), the (say ethanol/water) adsorption selectivity, S_{ads}, is defined by

$$S_{ads} = \frac{q_2/q_1}{y_2/y_1} = \frac{q_2/y_2}{q_1/y_1} \tag{S12}$$

where q_1 and q_2 are the molar loadings of the components 1, and 2 in the adsorbed phase in equilibrium with a bulk gas phase mixture with mole fractions $y_1 = \frac{f_1}{f_1 + f_2}; y_2 = \frac{f_2}{f_1 + f_2}$. In view of eqs (S10), and (S11), we may re-write eq (S12) as the ratio of the sorption pressures

$$S_{ads} = \frac{q_2/q_1}{y_2/y_1} = \frac{q_2/y_2}{q_1/y_1} = \frac{x_2/f_2}{x_1/f_1} = \frac{P_1^0}{P_2^0} \tag{S13}$$

Applying the restriction specified by eq (S6), it follows that S_{ads} is uniquely determined by the adsorption potential $\frac{\pi A}{RT}$.

4 The Real Adsorbed Solution Theory (RAST)

To account for non-ideality effects in mixture adsorption, we introduce activity coefficients γ_i into Equation (S4) [27]

$$f_i = P_i^0 x_i \gamma_i \tag{S14}$$

Following the approaches of Myers, Talu, and Sieperstein[28, 32, 33] we model the excess Gibbs free energy for binary mixture adsorption as follows

$$\frac{G^{excess}}{RT} = x_1 \ln(\gamma_1) + x_2 \ln(\gamma_2) \tag{S15}$$

4.1 Margules model for activity coefficients

The Margules model for activity coefficients is

$$\begin{aligned} \ln(\gamma_1) &= x_2^2 \left(A_{12} + 2\left(A_{21} - A_{12} \right) x_1 \right) \left(1 - \exp\left(-C \frac{\pi A}{RT} \right) \right) \\ \ln(\gamma_2) &= x_1^2 \left(A_{21} + 2\left(A_{12} - A_{21} \right) x_2 \right) \left(1 - \exp\left(-C \frac{\pi A}{RT} \right) \right) \end{aligned} \tag{S16}$$

In eq (S16) C is a constant with the units kg mol^{-1}. The introduction of $\left(1 - \exp\left(-C \frac{\pi A}{RT} \right) \right)$ imparts the correct limiting behaviors $\gamma_i \to 1$; $\frac{\pi A}{RT} \to 0$ for the activity coefficients in the Henry regime, $f_t \to 0$; $\frac{\pi A}{RT} \to 0$. As pore saturation conditions are approached, this correction factor tends to unity $\left(1 - \exp\left(-C \frac{\pi A}{RT} \right) \right) \to 1$. The choice of $A_{12} = A_{21} = 0$ in eq (S16), yields unity values for the activity coefficients.

The excess reciprocal loading for the mixture can be defined as

$$\left(\frac{1}{q_t} \right)^{excess} = \frac{1}{q_t} - \left(\frac{x_1}{q_1^0(P_1^0)} + \frac{x_2}{q_2^0(P_2^0)} \right) \tag{S17}$$

The Real Adsorbed Solution Theory (RAST)

The excess reciprocal loading for the mixture can be related to the partial derivative of the Gibbs free energy with respect to the adsorption potential at constant composition

$$\left(\frac{1}{q_t}\right)^{excess} = \left.\frac{\partial\left(\frac{G^{excess}}{RT}\right)}{\partial\left(\frac{\pi A}{RT}\right)}\right|_{T,x} = x_1 x_2 \left[A_{12}x_2 + A_{21}x_1\right] C \exp\left(-C\frac{\pi A}{RT}\right) \tag{S18}$$

For calculation of the total mixture loading $q_t = q_1 + q_2$ we need to replace eq (S11) by

$$\frac{1}{q_t} = \frac{x_1}{q_1^0(P_1^0)} + \frac{x_2}{q_2^0(P_2^0)} + x_1 x_2 \left[A_{12}x_2 + A_{21}x_1\right] C \exp\left(-C\frac{\pi A}{RT}\right) \tag{S19}$$

The parameters A_{12}, A_{21}, C can be fitted to match the experimental or CBMC data on mixture adsorption. The implementation of the activity coefficients is termed as the Real Adsorbed Solution Theory (RAST).

With the introduction of activity coefficients, the expression for the adsorption selectivity for binary mixtures is

$$S_{ads} = \frac{q_2/q_1}{y_2/y_1} = \frac{q_2/y_2}{q_1/y_1} = \frac{x_2/f_2}{x_1/f_1} = \frac{P_1^0\gamma_1}{P_2^0\gamma_2} \tag{S20}$$

5 Radial Distribution Functions of O····H distances

In order to demonstrate the occurrence of hydrogen bonding in water/methanol, and water/ethanol mixtures CBMC simulation data on the spatial locations of the guest molecules were sampled to determine the O····H distances of various pairs of molecules. distances. By sampling a total of 10^6 simulation steps, the radial distribution functions (RDF) of O····H distances were determined for water-water, water-alcohol, and alcohol-alcohol pairs. Figure S15a shows the RDF of O…H distances for molecular pairs of water(1)/methanol(2) mixture adsorption in CHA zeolite at 300 K. The partial fugacities of components 1 and 2 are f_1= 2.5 kPa, f_2= 7.5 kPa. We note the first peaks in the RDFs occur at a distance less than 2 Å, that is characteristic of hydrogen bonding.[10, 34] The heights of the first peaks are a direct reflection of the degree of hydrogen bonding between the molecular pairs. We may conclude, therefore that for water/methanol mixtures the degree of H-bonding between water-methanol pairs is significantly larger, by about an order of magnitude, than for water-water, and methanol-methanol pairs. Analogous set of conclusions can be drawn for water/ethanol mixtures, for which the RDF data are presented in Figure S15b, i.e. the degree of H-bonding between water-ethanol pairs is larger than for water-water, and ethanol-ethanol pairs. For comparison purposes, the RDF data for adsorption of methanol/ethanol mixtures are shown in Figure S15c. The magnitude of the first peaks for methanol-ethanol, methanol-methanol, ethanol-ethanol pairs are significantly lower than the water-alcohol peaks in Figure S15a,b. Therefore, the H-bonding effects should be expected to be of less importance for methanol/ethanol mixture adsorption in CHA than for water/methanol and water/ethanol mixtures.

A visual appreciation of hydrogen bonding is gleaned from the snapshots in Figure S16 for mixture adsorption in CHA.

Radial Distribution Functions of O····H distances

Figure S17 shows the corresponding results for RDF of O···H distances for molecular pairs of water(1)/ethanol(2) mixture adsorption in DDR zeolite at 300 K. The H-bonding between water/ethanol pairs is much stronger than for water/water and ethanol/ethanol pairs; these conclusions are in line with those for CHA zeolite. A visual appreciation of hydrogen bonding is gleaned from the snapshots in Figure S18 for mixture adsorption in DDR.

Figure S19 shows the data on RDF of O···H distances for molecular pairs of water(1)/ethanol(2) mixture adsorption in MFI zeolite at 300 K. We again conclude that H-bonding between water/ethanol pairs is more significant than for other pairs. Computational snapshots are provided in Figure S20.

5.1 List of Figures for Radial Distribution Functions of O····H distances

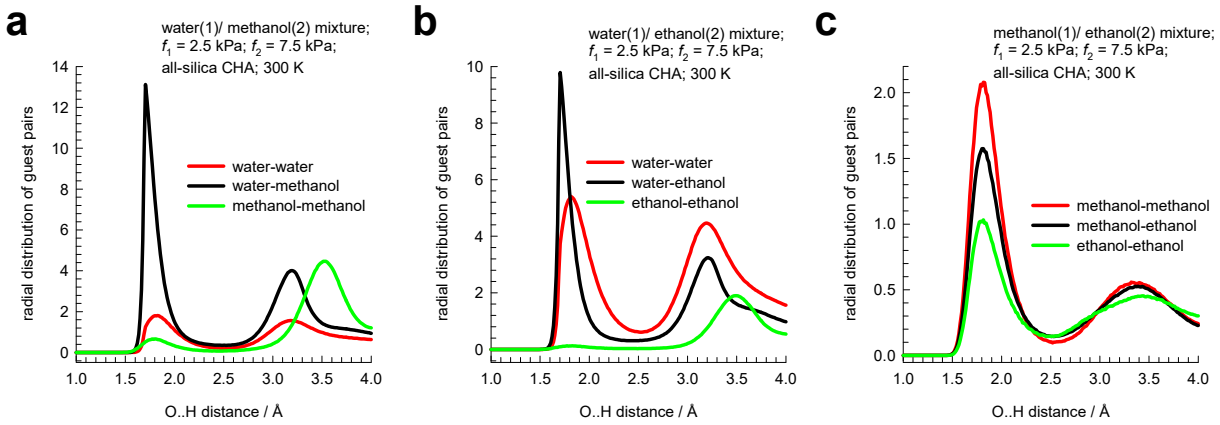

Figure S15. RDF of O···H distances for molecular pairs of (a) water(1)/methanol(2), (b) water(1)/ethanol(2), and (c) methanol(1)/ethanol(2) mixture adsorption in CHA zeolite at 300 K. For all three sets of mixtures, the partial fugacities of components 1 and 2 are f_1= 2.5 kPa, f_2= 7.5 kPa. The *y*-axes are normalized in the same manner and, therefore, the magnitudes of the first peaks is a direct reflection of the degree of hydrogen bonding between the molecular pairs.

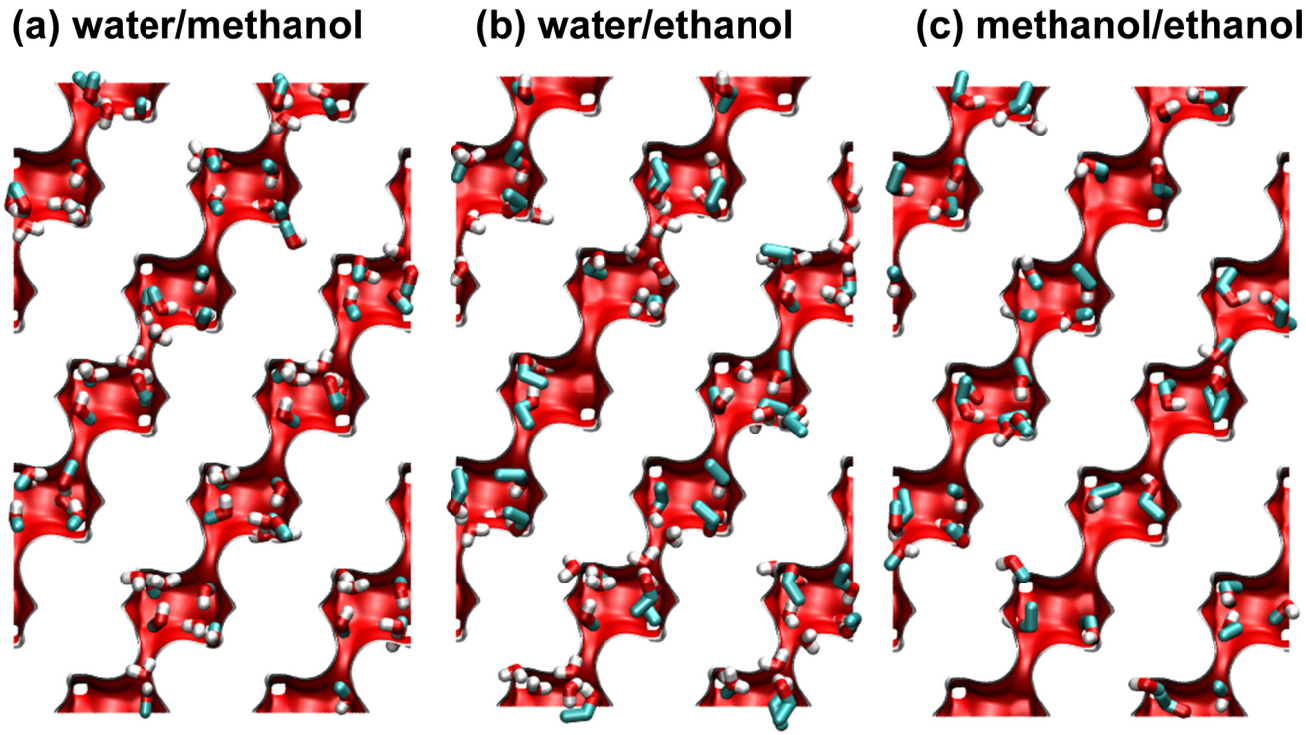

Figure S16. Snapshots showing location and conformations of guest molecules for adsorption of (a) water(1)/methanol(2), (b) water(1)/ethanol(2), and (c) methanol(1)/ethanol(2) mixture adsorption in CHA zeolite at 300 K. The partial fugacities of components 1 and 2 are f_1= 2.5 kPa, f_2= 7.5 kPa.

Radial Distribution Functions of O····H distances

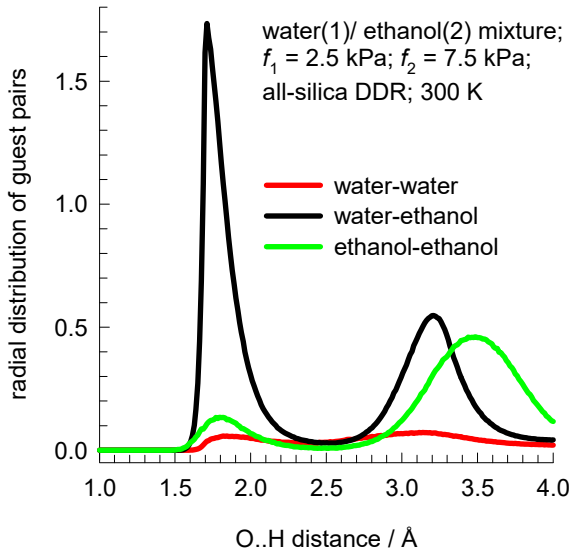

Figure S17. RDF of O····H distances for molecular pairs of water(1)/ethanol(2) mixture adsorption in DDR zeolite at 300 K. The partial fugacities of components 1 and 2 are f_1= 2.5 kPa, f_2= 7.5 kPa.

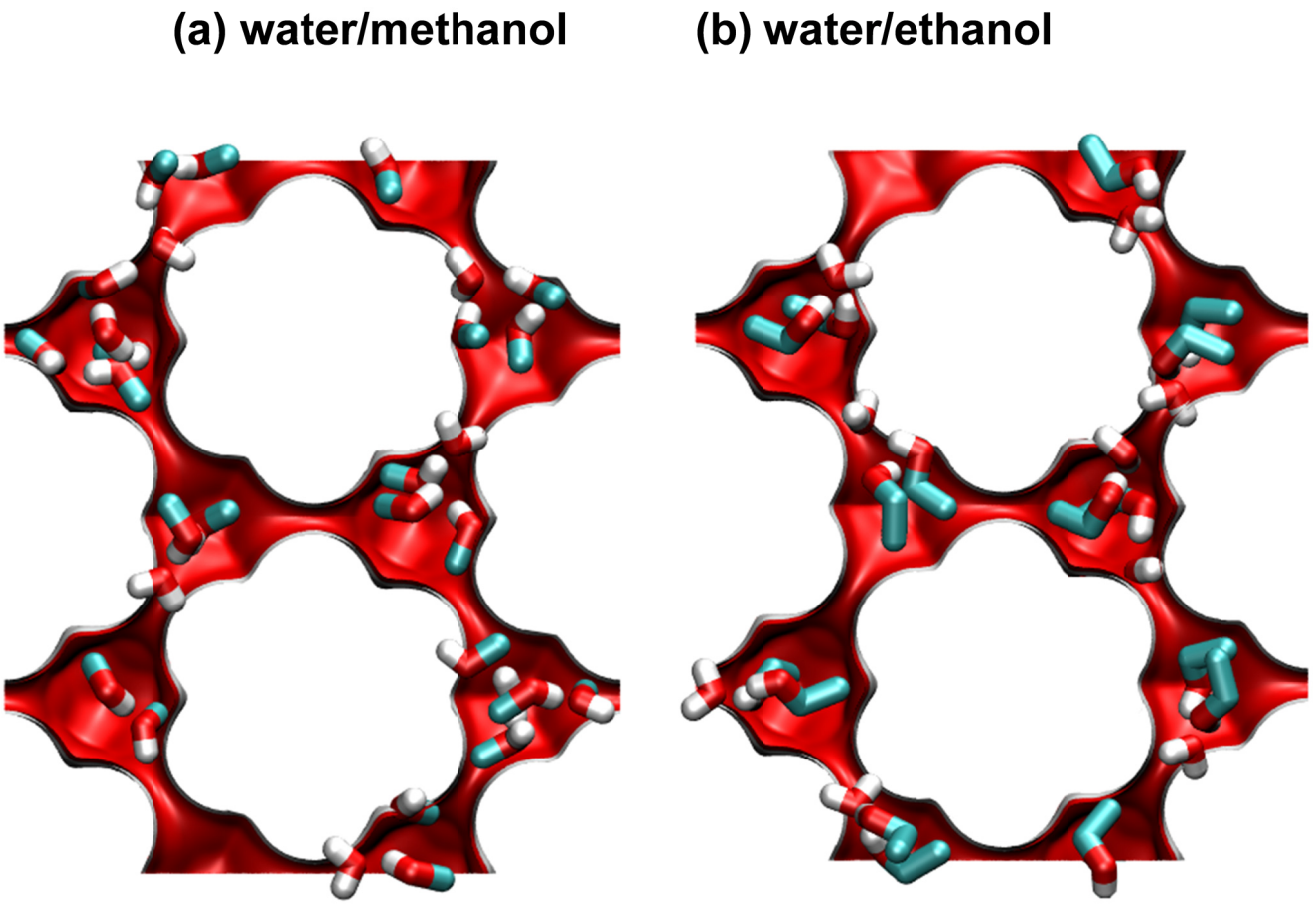

Figure S18. Snapshots showing location and conformations of guest molecules for adsorption of (a) water(1)/methanol(2), and (b) water(1)/ethanol(2) mixture adsorption in DDR zeolite at 300 K. The partial fugacities of components 1 and 2 are f_1= 2.5 kPa, f_2= 7.5 kPa.

Radial Distribution Functions of O····H distances

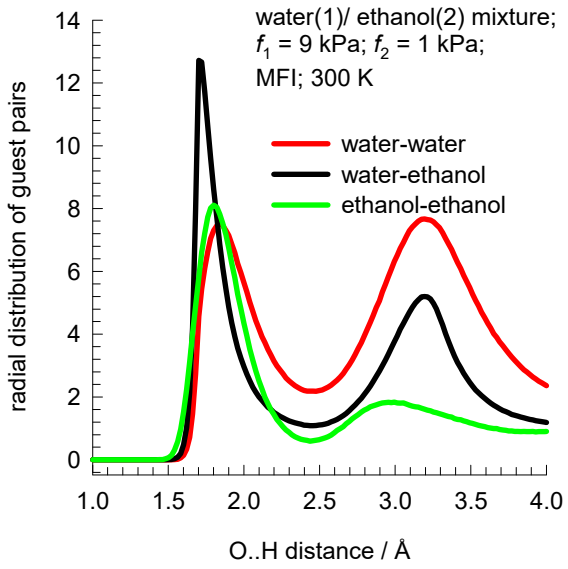

Figure S19. RDF of O····H distances for molecular pairs of water(1)/ethanol(2) mixture adsorption in MFI zeolite at 300 K. The partial fugacities of components 1 and 2 are f_1= 9 kPa, f_2= 1 kPa.

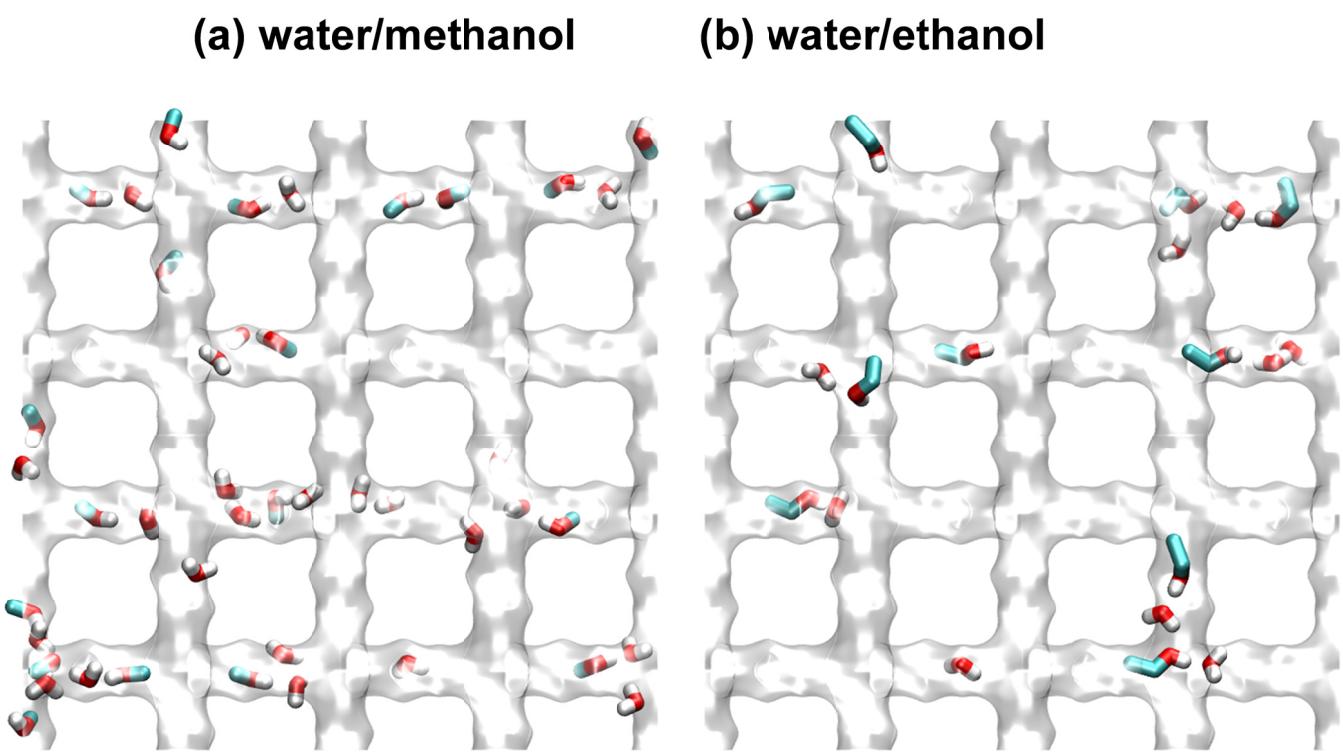

Figure S20. Snapshots showing location and conformations of guest molecules for adsorption of (a) water(1)/methanol(2), and (b) water(1)/ethanol(2) mixture adsorption in MFI zeolite at 300 K.

Radial Distribution Functions of O···H distances

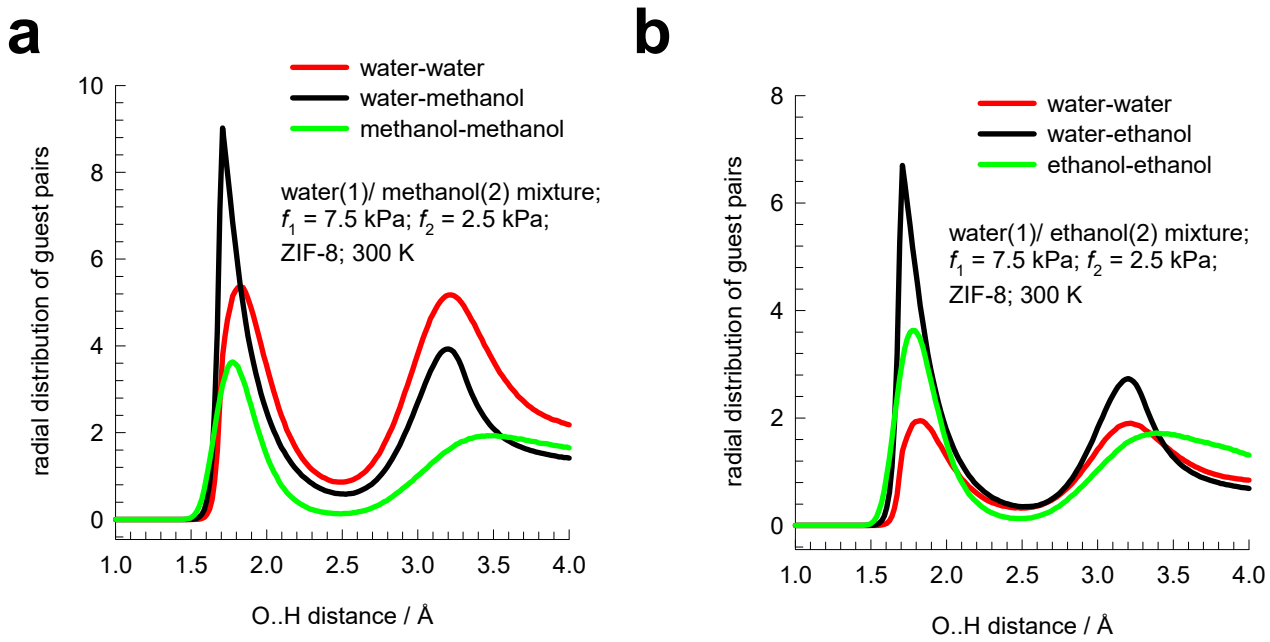

Figure S21. RDF of O···H distances for molecular pairs of (a) water(1)/methanol(2), and (b) water(1)/ethanol(2) mixture adsorption in ZIF-8 at 300 K. For both mixtures, the partial fugacities of components 1 and 2 are f_1= 7.5 kPa, f_2= 2.5 kPa. The *y*- axes are normalized in the same manner and, therefore, the magnitudes of the first peaks is a direct reflection of the degree of hydrogen bonding between the molecular pairs.

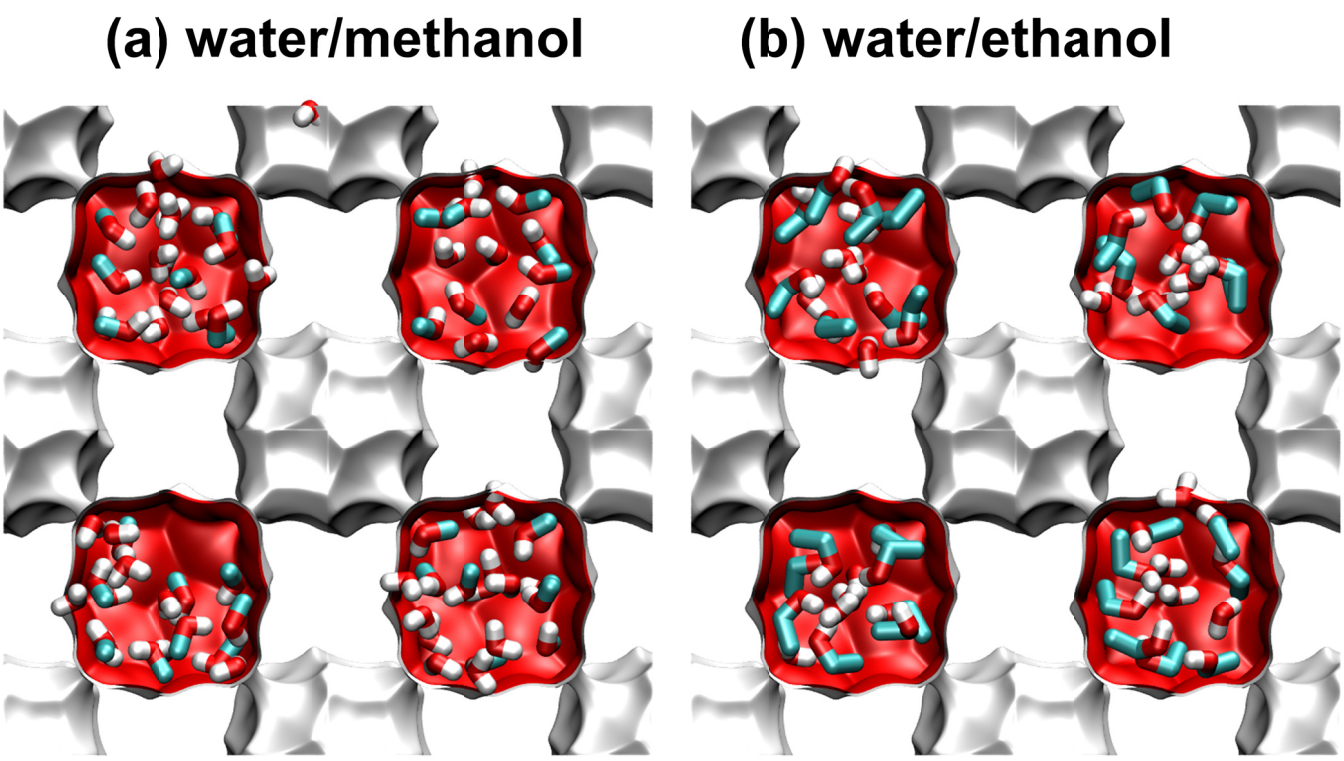

Figure S22. Snapshots showing location and conformations of guest molecules for adsorption of (a) water(1)/methanol(2), and (b) water(1)/ethanol(2) mixture adsorption in ZIF-8 at 300 K.

6 CBMC data for mixture adsorption and RAST analysis

6.1 CBMC simulation campaigns

A comprehensive campaign of CBMC simulations for adsorption of binary mixtures (water/methanol, water/ethanol) was undertaken to investigate hydrogen bonding effects in three all-silica zeolites (CHA, DDR, and FAU), and ZIF-8. Two types of mixture adsorption campaigns were conducted.

Campaign A. The bulk fluid phase composition held constant at $y_1 = y_2 = 0.5$, and the bulk fluid phase fugacity $f_t = f_1 + f_2$ was varied over a wide range from the Henry regime of adsorption, $f_t \to 0$; $\frac{\pi A}{RT} \to 0$, to pore saturation conditions, typically $\frac{\pi A}{RT} > 50$.

Campaign B. The bulk fluid phase fugacity $f_t = f_1 + f_2$ was held at a constant value, and the bulk fluid phase mixture composition y_1 was varied $0 < y_1 < 1$.

Each CBMC simulation data point, for specified partial fugacities in the bulk fluid phase, f_1, f_2, yields the component loadings, $q_{1,CBMC}; q_{2,CBMC}$, and the total mixture loading $q_{t,CBMC} = q_{1,CBMC} + q_{2,CBMC}$.

For each guest/host combination, CBMC simulations of the unary isotherms of the constituent guest molecules were also carried out.

Additionally, we present a re-analysis of the CBMC simulations of Nalaparaju et al.[7] for water/methanol and water/ethanol mixture adsorption in ZIF-71 at 298 K. Also included in the simulations are re-analyses of CBMC data for polar guests in CuBTC as published in our earlier works.[24, 25]

6.2 Unary isotherm fit parameters

The CBMC simulated unary isotherms were fitted with the dual-site Langmuir-Freundlich model, eq (S8). The unary isotherm for water adsorption in ZIF-8, and CuBTC required the use of the 3-site Langmuir-Freundlich model to capture the steep isotherm characteristics.

The unary isotherm fit parameters are provided in the following set of Tables.

Unary isotherms for water, methanol, and ethanol in CHA: Table S4

Unary isotherms for water, methanol, and ethanol in DDR: Table S5

Unary isotherms for water, methanol, and ethanol in FAU: Table S6

Unary isotherms for water, methanol, ethanol, 1-propanol, benzene, acetone in CuBTC: Table S7, and Table S8.

Unary isotherms for water, methanol, and ethanol in ZIF-8: Table S10

Unary isotherms for water, methanol, and ethanol in ZIF-71: Table S11

Figure S23a,b compare CBMC simulations of unary water isotherms in different microporous host materials, plotted as function of the fugacity of water in the bulk fluid phase. The plot clearly shows the difference between various hydrophobic hosts (all-silica zeolites, ZIF-8, ZIF-71) and hydrophilic host CuBTC.

6.3 Determination of activity coefficients from CBMC mixture adsorption data

For each CBMC mixture simulation campaign (Campaign A, or Campaign B), the mole fractions of the adsorbed phase, $x_1 = \frac{q_{1,CBMC}}{q_{t,CBMC}}; x_2 = \frac{q_{2,CBMC}}{q_{t,CBMC}}; q_{t,CBMC} = q_{1,CBMC} + q_{2,CBMC}$ are determined. The sorption pressures P_1^0, P_2^0, each of which satisfying eq (S6), can be determined from using the unary isotherm fits for each of the components in the binary mixture.

The activity coefficients of the two components $\gamma_{1,CBMC}; \gamma_{2,CBMC}$ are determined from eq (S14):

$$\gamma_{1,CBMC} = \frac{f_1}{P_1^0 x_{1,CBMC}}; \gamma_{2,CBMC} = \frac{f_2}{P_2^0 x_{2,CBMC}} \tag{S21}$$

The activity coefficients of the two components $\gamma_{1,CBMC}; \gamma_{2,CBMC}$, determined using eq (S21) are subject to a degree of scatter that is inherent in the CBMC mixture simulation data.

6.4 Determination of Margules fit parameters from mixture adsorption data

For each mixture/host combination, the set of three Margules parameters A_{12}, A_{21}, C that yield the minimum value for the objective function calculated as the sum of the mean-squared deviations between the CBMC simulated component loadings, and those predicted using RAST

$$\text{Objective Function} = \left(q_{1,CBMC} - q_{1,RAST}\right)^2 + \left(q_{2,CBMC} - q_{2,RAST}\right)^2 \quad \text{(S22)}$$

The A_{12}, A_{21}, C were determined using the Excel solver function. For determination of the Margules parameters A_{12}, A_{21}, C, the CBMC data for both Campaigns A, and B were employed. The values of the fitted Margules parameters A_{12}, A_{21}, C are tabulated in Table S4 (CHA), Table S5 (DDR), Table S6 (FAU), and Table S9 (CuBTC).

6.5 Summary of CBMC simulation data and comparison with RAST.

The CBMC simulated data, and comparison with the RAST model, with fitted Margules parameters are presented graphically in the following set of Figures.

Figure S24: Campaign A for water/methanol mixture in CHA

Figure S25: Campaign B for water/methanol mixture in CHA

Figure S26: Campaign A for water/ethanol mixture in CHA

Figure S27: Campaign B for water/ethanol mixture in CHA

Figure S28: Campaign A for methanol/ethanol mixture in CHA

Figure S29: Campaign B for methanol/ethanol mixture in CHA

Figure S30: Campaign A for water/methanol mixture in DDR

Figure S31: Campaign B for water/methanol mixture in DDR

Figure S32: Campaign A for water/ethanol mixture in DDR

Figure S33: Campaign B for water/ethanol mixture in DDR

CBMC data for mixture adsorption and RAST analysis

Figure S34: Campaign A for water/methanol mixture in FAU

Figure S35: Campaign B for water/methanol mixture in FAU

Figure S36: Campaign A for water/ethanol mixture in FAU

Figure S37: Campaign A for water/methanol mixture in CuBTC

Figure S38: Campaign A for water/ethanol mixture in CuBTC

Figure S39: Campaign A for methanol/ethanol mixture in CuBTC

Figure S40: Campaign A for water/1-propanol mixture in CuBTC

Figure S41: Campaign A for water/benzene mixture in CuBTC

Figure S42: Campaign A for methanol/benzene mixture in CuBTC

Figure S43: Campaign A for ethanol/benzene mixture in CuBTC

Figure S44: Campaign A for acetone/benzene mixture in CuBTC

Figure S45: Campaign A for water/methanol mixture in ZIF-8

Figure S46: Campaign B for water/methanol mixture in ZIF-8

Figure S47: Campaign A for water/ethanol mixture in ZIF-8

Figure S48: Campaign B for water/ethanol mixture in ZIF-8

Figure S49: Campaign A for water/methanol mixture in ZIF-71

Figure S50: Campaign A for water/ethanol mixture in ZIF-71

For Campaign A, each of the Figures contains the following six sub-figures:

(a) CBMC simulated unary isotherms along the isotherm fits, plotted as function of the bulk fluid phase fugacity

(b) CBMC simulated component loadings $q_{1,CBMC}; q_{2,CBMC}$ (filled symbols) for binary mixture plotted as function of the corresponding partial fugacities, $f_1 = f_2$ in the bulk fluid phase. Also shown with open symbols are the corresponding CBMC unary isotherms data.

(c) Adsorption selectivity, S_{ads}, determined from CBMC mixture simulations (symbols) along with calculations using the IAST (dashed line) and RAST (continuous solid line). The *x*-axis represents the total bulk fluid phase fugacity $f_t = f_1 + f_2$.

(d) CBMC simulated component loadings $q_{1,CBMC}; q_{2,CBMC}$ (filled symbols) for binary mixture plotted as function of the total bulk fluid phase, $f_t = f_1 + f_2$. The continuous solid lines are the RAST calculations using the fitted Margules parameters.

(e) Comparison of the activity coefficients determined directly from CBMC mixture simulations, $\gamma_{1,CBMC}; \gamma_{2,CBMC}$ (filled symbols) and the activity coefficients calculated using the RAST with fitted Margules parameters (continuous solid lines). The *x*-axis represents the total bulk fluid phase fugacity $f_t = f_1 + f_2$. RAST calculations of the ratio of activity coefficients, γ_1/γ_2, for water/alcohol mixtures in different hosts are summarized in Figure S53. It is noteworthy that γ_1/γ_2 displays a minimum, a characteristic of hydrogen bonding effects.

(f) Comparison of the activity coefficients determined directly from CBMC mixture simulations, $\gamma_{1,CBMC}; \gamma_{2,CBMC}$ (filled symbols) and the activity coefficients calculated using the RAST with fitted Margules parameters (continuous solid lines). The *x*-axis represents the mole fraction of component 1 in the adsorbed phase. For CBMC data, $\gamma_{1,CBMC}; \gamma_{2,CBMC}$ are plotted against $x_1 = \frac{q_{1,CBMC}}{q_{t,CBMC}}$; for RAST the $\gamma_1; \gamma_2$ are plotted against the corresponding calculations of the adsorbed phase mole fraction, x_1.

For Campaign B, each of the Figures contains the following three sub-figures:

(a) CBMC simulated component loadings $q_{1,CBMC}; q_{2,CBMC}$ (filled symbols) for binary mixtures, plotted as function of the mole fraction of component 1 in the bulk fluid phase, y_1. The dashed lines are the loadings calculated from the IAST. The continuous solid lines are the RAST calculations using the fitted Margules parameters.

(b) Adsorption selectivity, S_{ads}, determined from CBMC mixture simulations (symbols) along with calculations using the IAST (dashed line) and RAST (continuous solid line). The *x*-axis represents the mole fraction of component 1 in the bulk fluid phase, y_1.

(c) Comparison of the activity coefficients determined directly from CBMC mixture simulations, $\gamma_{1,CBMC};\gamma_{2,CBMC}$ (filled symbols) and the activity coefficients calculated using the RAST with fitted Margules parameters (continuous solid lines). The *x*-axis represents the mole fraction of component 1 in the adsorbed phase. For CBMC data, $\gamma_{1,CBMC};\gamma_{2,CBMC}$ are plotted against $x_{1,CBMC}=\frac{q_{1,CBMC}}{q_{t,CBMC}}$; for RAST the $\gamma_1;\gamma_2$ are plotted against the corresponding calculations of the adsorbed phase mole fraction, x_1.

6.6 Summary of key features for mixture adsorption with hydrogen bonding.

For the simulation results for Campaign A, the following major generic characteristics emerge for the various mixture/host combinations. These characteristics are deduced from the six sub-figures, discussed below in turn.

(a) Due to hydrogen bonding effects, the unary isotherms for water are very steep; detailed explanations for the underlying reasons are provided in our earlier publications.[10, 24, 25, 35, 36] The steepness is particularly pronounced in CuBTC, and the water isotherm requires a 3-site Langmuir-Freundlich isotherm model for fitting. The alcohol isotherms are also steep in some guest frameworks, but the steepness is less pronounced than for water.

(b) For a range of partial fugacities, f_1 in the bulk fluid phase, the component loading for water in the mixture (filled symbols) exceeds that of the pure component. This is directly ascribable to the high degree of hydrogen bonding between the water/methanol and water/ethanol pairs. The enhancement of the water loading in the mixture, calculated by dividing CBMC data for water loading in mixture by the unary water loading (determined from unary isotherm fits using the

partial fuagacity of water, f_1, in the bulk fluid phase) is plotted in Figure S51 for water/alcohol mixtures in different host materials. The enhancement in water loading, due to hydrogen bonding, can be as high as two orders of magnitudes.

(c) Generally speaking, the alcohol/water adsorption selectivity, S_{ads}, determined from CBMC mixture simulations (symbols) has a tendency to undergo selectivity reversal in favor of water at high values of the bulk fluid phase fugacity $f_t = f_1 + f_2$, as saturation conditions are approached. Figure S52 illustrates the selectivity reversal for a variety of water/alcohol mixtures in different host materials. The selectivity reversal in favor of the smaller guest molecule is the consequence of entropy effects that favor the guest species with the higher packing efficiency, as explained in earlier works.[29, 36-40] The selectivity reversal phenomena is also anticipated by the IAST model (shown by the dashed line). An important characteristic observed in most, but not all, mixture/host combinations is that the IAST over-predicts the alcohol/water selectivity at values of $f_t = f_1 + f_2$ lower than that at which selectivity reversal occurs. For values of $f_t = f_1 + f_2$ higher than that at selectivity reversal, the IAST estimates lie below the values determined from CBMC. The conclusion to be drawn is that IAST exaggerates entropy effects. Put another way, hydrogen bonding effects tend to moderate the influence of entropy effects because of molecular clustering attendant with mixture adsorption. As is to be expected the RAST model captures the right trends in the dependence of S_{ads} on $f_t = f_1 + f_2$. The aforementioned comments regarding alcohol/water selectivity also apply to ethanol/methanol selectivity in CHA; see Figure S28. Following eq (S20) we note that the alcohol/water selectivity is proportional to $\frac{\gamma_1}{\gamma_2}$. RAST calculations of the ratio of activity coefficients, γ_1/γ_2, for water/alcohol mixtures in different hosts are summarized in Figure S53. It is noteworthy that γ_1/γ_2 displays a minimum, a characteristic of hydrogen bonding effects.

(d) For all binary mixtures investigated, the RAST estimates of the component loadings are in reasonably good agreement with CBMC simulated component loadings $q_{1,CBMC}; q_{2,CBMC}$ (filled symbols). This is to be expected because the model parameters are chosen to fit the CBMC simulated component loadings. The success of the RAST model is therefore to be regarded as testimony to the applicability of the Margules model to describe the activity coefficients for mixture adsorption.

(e) Both activity coefficients tend to unity in the Henry regime, as $\gamma_i \to 1$; $f_t \to 0$. The activity coefficient of water, γ_1, displays a minimum when plotted against the total bulk fluid phase fugacity $f_t = f_1 + f_2$. The activity coefficient of alcohol tends to decrease to low values as $f_t = f_1 + f_2$ increases. RAST calculations of the ratio of activity coefficients, γ_1/γ_2, for water/alcohol mixtures in different hosts are summarized in Figure S53; the *x*-axis is the adsorption potential, $\frac{\pi A}{RT}$. It is noteworthy that γ_1/γ_2 displays a minimum, a characteristic of hydrogen bonding effects.

(f) The activity coefficient of water, γ_1, tends to unity as the adsorbed phase mole fraction $x_1 \to 1$; it displays a minimum. The activity coefficient of alcohol, γ_2, tends to unity as the adsorbed phase mole fraction $x_2 = (1 - x_1) \to 1$, decreasing in magnitude as $x_1 \to 1$.

For the simulation results for Campaign B, the following generic characteristics emerge for all the mixture/host combinations. These characteristics are discussed below.

(a) The RAST calculations (continuous solid line) of the component loadings are, broadly speaking, in reasonable agreement with CBMC simulated component loadings $q_{1,CBMC}; q_{2,CBMC}$ (filled symbols) for binary mixture plotted as function of the mole fraction of component 1 in the bulk fluid phase, y_1. The continuous solid lines are the RAST calculations using the fitted Margules parameters.

(b) Adsorption selectivity, S_{ads}, determined from CBMC mixture simulations (symbols) along with calculations using the IAST (dashed line) and RAST (continuous solid line). The *x*-axis represents the mole fraction of component 1 in the bulk fluid phase, y_1. For some host materials, the alcohol/water adsorption selectivity experiences a selectivity reversal; see summary of CBMC data on S_{ads} in Figure S54a. The occurrence of selectivity reversal is caused by hydrogen bonding; the manifestation of hydrogen bonding is that ratio of activity coefficients, $\frac{\gamma_1}{\gamma_2}$ increases with the mole fraction of water (component 1) in the bulk fluid phase, y_1; see Figure S54b.

6.7 Analysis of published experimental data

Experimental evidence of the influence of hydrogen bonding on mixture adsorption in zeolites and MOFs is available in some published data. Figure S55 presents an analysis of the experimental of of van Assche et al.[41] for adsorption of methanol, and n-hexane at 313 K in CuBTC, The IAST overestimates the methanol/n-hexane adsorption selectivity to a significant extent.

Figure S56 presents an analysis of the experimental data of Sakuth et al.[42, 43] for toluene(1)/1-propanol(2) mixture adsorption in DAY-13 (dealuminated Y zeolite, with FAU topology) at T = 298.15 K and two different total pressure of 1.06 kPa. The IAST calculations anticipate that the selectivity is in favor of toluene for the entire range of bulk fluid phase compositions. The experimental data, on the other hand, displays selectivity reversal in favor of 1-propanol for bulk fluid phase compositions y_1 > 0.4. The IAST does not anticipate the reversal in the toluene/1-propanol selectivity with increased mole fraction of the aromatic in the bulk fluid mixture.

The experimental data of Takeuchi et al.[44] for adsorption of 1-butanol(1)/p-xylene(2) mixtures in high silica Y zeolite, obtained at 298 K and total pressure of 60 Pa present further evidence of thermodynamic non-idealities in mixture adsorption; Figure S57. The IAST calculations anticipate that the selectivity is in favor of 1-butanol(1) for the entire range of bulk fluid phase compositions. The

experimental data, on the other hand, displays selectivity reversal in favor of p-xylene(2) for bulk vapor phase compositions $y_1 > 0.5$.

6.8 CBMC simulation campaigns for mixtures without hydrogen bonding

In order to underscore the differences in the characteristics of thermodynamic non-idealities caused by hydrogen bonding with (a) thermodynamically ideal systems and (b) mixtures in which non-idealities are engendered by congregartion and segregation effects, CBMC simulation data for mixture adsorption from were performed and analyzed for the following systems:

CH_4/C_3H_8 mixture adsorption in MFI zeolite at 300 K; see Figure S58

CH_4/C_2H_6 mixture adsorption in NaX zeolite at 300 K; see Figure S59

CH_4/C_3H_8 mixture adsorption in NaX zeolite at 300 K; see Figure S60

CO_2/C_3H_8 mixture adsorption in NaX zeolite at 300 K; see Figure S61, Figure S62

n-butane(nC4)/iso-butane(iC4) mixture adsorption in MFI zeolite at 300 K; see Figure S63

n-hexane(nC6)/2-methylpentane(2MP) mixture adsorption in MFI zeolite at 300 K; see Figure S64

For all mixtures listed above, the following CBMC mixture campaign A was undertaken. Here, the bulk fluid phase composition held constant at $y_1 = y_2 = 0.5$, and the bulk fluid phase fugacity $f_t = f_1 + f_2$ was varied over a wide range from the Henry regime of adsorption, $f_t \to 0$; $\frac{\pi A}{RT} \to 0$, to pore saturation conditions, typically $\frac{\pi A}{RT} > 50$.

In addition, for CO_2/C_3H_8 mixture adsorption in NaX zeolite at 300 K, Campaign B was undertaken in which the bulk fluid phase fugacity $f_t = f_1 + f_2$ was held at a constant value of 1 MPa, and the bulk fluid phase mixture composition y_1 was varied $0 < y_1 < 1$.

6.9 Summary of key features for mixture adsorption without hydrogen bonding.

For adsorption of CH_4/C_2H_6, and CH_4/C_3H_8 mixtures in MFI and NaX zeolites, there are no thermodynamic non-idealities and the IAST provides a good quantitative description of mixture

adsorption; see Figure S58, Figure S59, and Figure S60. The decrease in the C_2H_6/CH_4, and C_3H_8/CH_4 adsorption selectivities with increased bulk fluid phase fugacity $f_t = f_1 + f_2$ is attributable to entropy effects that become stronger as pore saturation conditions are approached; the explanation of entropy effects is available in our earlier publications.[36, 37, 40] Also noteworthy, from examination of Figure S58b, Figure S59b, and Figure S60b is that the component loadings in the mixture are lower than the values determined from unary adsorption, when compared at the same partial fugacities in the bulk fluid phase.

Thermodynamic non-idealities in CO_2/C_3H_8 mixture adsorption in NaX zeolite (see Figure S61, Figure S62) are caused due to congregation of CO_2 around the Na^+ cations. Such congregation effects are elucidated in our earlier publications.[29-31] Such congregation effects have the effect of reducing the competition between CO_2, and C_3H_8; consequently, the IAST overestimates the adsorption selectivity; the IAST assumes a homogeneous distribution of adsorbates.

For nC4/iC4 and nC6/2MP mixture adsorption in MFI zeolite (cf. Figure S63, Figure S64) the preferential location of the branched alkanes at the channel intersections engenders thermodynamic non-idealities.[35, 40]

Thermodynamic non-idealities caused by congregation or segregation effects have different characteristics compared to those for mixtures for which hydrogen bonding effects occur. One manifestation of the differences is highlighted by comparison of the ratio of activity coefficients as a function of the adsorption potential $\frac{\pi A}{RT}$ for systems with hydrogen bonding and those induced by congregation/segregation effects. Figure S65 compares RAST Margules model calculations of the ratio of activity coefficients γ_1/γ_2 for (a, b) water/alcohol mixtures, and (b) mixtures subject to non-idealities induced by congregation/segregation effects. For mixtures subject to hydrogen bonding, γ_1/γ_2 exhibits a pronounced minimum, whereas for mixtures not influenced by hydrogen bonding, no such minimum is displayed.

Also noteworthy, from examination of Figure S61b, Figure S63b, and Figure S64b is that the component loadings in the mixture are lower than the values determined from unary adsorption, when compared at the same partial fugacities in the bulk fluid phase. This finding is distinctly different from adsorption of water/alcohol mixtures for which the water loadings in the mixture may exceed that of the pure water.

6.10 List of Tables for CBMC data for mixture adsorption and RAST analysis

Table S4. Dual-site Langmuir-Freundlich parameters for unary 1-alcohols in CHA at 300 K. The fit parameters are based on the CBMC simulations of pure component isotherms presented in earlier work.[39]

	Site A			Site B		
	$q_{A,sat}$ mol kg^{-1}	b_A Pa$^{-\nu_A}$	ν_A	$q_{B,sat}$ mol kg^{-1}	b_B Pa$^{-\nu_B}$	ν_B
water	16.8	3.031E-54	15.6	4.6	2.218E-05	1
methanol	3.7	4.281E-11	3.37	3.7	4.545E-04	1
ethanol	2.5	8.578E-06	1.07	2.9	3.505E-03	1.1

Fitted Margules non-ideality parameters for binary mixture adsorption in CHA at 300 K. The fits are based on combining CBMC Campaigns A and B for each mixture.

	C / kg mol^{-1}	A_{12}	A_{21}
water/methanol	1.128	-8.716	-0.081
water/ethanol	0.112	-7.286	-3.611
methanol/ethanol	0.012	-4.836	-4.645

CBMC data for mixture adsorption and RAST analysis

Table S5. Dual-site Langmuir-Freundlich parameters for pure component water, methanol, and ethanol at 300 K in all-silica DDR zeolite. The fit parameters are based on the CBMC simulations of pure component isotherms presented in earlier work.[10]

	Site A			Site B		
	$q_{A,sat}$ mol kg^{-1}	b_A Pa$^{-\nu_A}$	ν_A	$q_{B,sat}$ mol kg^{-1}	b_B Pa$^{-\nu_B}$	ν_B
water	6.45	2.776E-17	4.3	2.4	1.300E-05	1.06
methanol	1.7	1.186E-04	1.3	1.7	6.055E-04	0.78
ethanol	1.6	9.962E-03	0.88	1.2	9.160E-05	0.66

Fitted Margules non-ideality parameters for binary mixture adsorption in DDR at 300 K. The fits are based on combining CBMC Campaigns A and B for each mixture.

	C / kg mol^{-1}	A_{12}	A_{21}
water/methanol	10.277	-2.497	-2.046
water/ethanol	0.764	-4.426	-1.991

CBMC data for mixture adsorption and RAST analysis

Table S6. Dual-site Langmuir-Freundlich parameters for adsorption of water, methanol, and ethanol at 300 K in all-silica FAU zeolite. The fit parameters are based on the CBMC simulations of pure component isotherms presented in earlier work.[10]

Adsorbate	Site A			Site B		
	$q_{A,sat}$ mol kg^{-1}	b_A Pa$^{-\nu_A}$	ν_A	$q_{B,sat}$ mol kg^{-1}	b_B Pa$^{-\nu_B}$	ν_B
water	16	1.54×10^{-121}	33	4.6	624×10^{-5}	1
methanol	3.4	6.36×10^{-16}	4.6	5.8	1.68×10^{-4}	1
ethanol	2.5	3.19×10^{-13}	4.9	2.9	1×10^{-3}	1.05

Fitted Margules non-ideality parameters for binary mixture adsorption in FAU at 300 K. The fits are based on combining CBMC Campaigns A and B for mixtures.

	C / kg mol^{-1}	A_{12}	A_{21}
water/methanol	0.675	-1.722	-2.554
water/ethanol	0.332	-0.869	-1.068

Table S7. 3-site Langmuir-Freundlich isotherm fits for adsorption of water in CuBTC at 298 K.

	Site A			Site B			Site C		
	$q_{A,sat}$ mol kg^{-1}	b_A Pa$^{-\nu_{iA}}$	ν_A	$q_{B,sat}$ mol kg^{-1}	b_B Pa$^{-\nu_{iB}}$	ν_B	$q_{C,sat}$ mol kg^{-1}	b_C Pa$^{-\nu_C}$	ν_C
water	22	5.48 $\times 10^{-4}$	1	22	6.24 $\times 10^{-32}$	10	10	2.51 $\times 10^{-4}$	0.6

CBMC data for mixture adsorption and RAST analysis

Table S8. Dual-site Langmuir-Freundlich parameters for adsorption of methanol, ethanol, 1-propanol, acetone, and benzene at 298 K in CuBTC.

Adsorbate	Site A			Site B		
	$q_{A,sat}$ mol kg^{-1}	b_A Pa$^{-\nu_A}$	ν_A	$q_{B,sat}$ mol kg^{-1}	b_B Pa$^{-\nu_B}$	ν_B
methanol	8.4	3.82×10^{-4}	1.03	11.5	9.3×10^{-16}	6.5
ethanol	5	2.29×10^{-3}	0.97	8	6.41×10^{-7}	3.2
1-propanol	8	4.83×10^{-4}	2.7	2	2.07×10^{-2}	0.5
acetone	5	4.83×10^{-17}	7.5	4.9	1.39×10^{-2}	0.7
benzene	4.6	2.76×10^{-6}	3.1	2.1	3.96×10^{-3}	1

Table S9. Fitted Margules non-ideality parameters for binary mixture adsorption in CuBTC at 298 K.

	C / kg mol^{-1}	A_{12}	A_{21}
water/methanol	0.005	-20.565	-10.590
water/ethanol	0.068	-12.427	-5.443
methanol/ethanol	0.002	-12.500	-8.068
water/1-propanol	0.049	-18.882	-6.752
water/benzene	0.002	-144.760	-70.527
methanol/benzene	0.019	-7.821	-13.592
ethanol/benzene	0.019	-10.220	-9.023
acetone/benzene	0.029	-7.791	-5.977

CBMC data for mixture adsorption and RAST analysis

Table S10. 3-site and 2-site Langmuir-Freundlich parameters for adsorption of water, methanol, and ethanol at 300 K in ZIF-8.

	Site A			Site B			Site C		
	$q_{A,sat}$ mol kg^{-1}	b_A Pa$^{-\nu_{iA}}$	ν_A	$q_{B,sat}$ mol kg^{-1}	b_B Pa$^{-\nu_{iB}}$	ν_B	$q_{C,sat}$ mol kg^{-1}	b_C Pa$^{-\nu_C}$	ν_C
water	22	2.08 $\times 10^{-57}$	13.4	3.6	1.327 $\times 10^{-15}$	3.2	69	1.20 $\times 10^{-7}$	1

Adsorbate	Site A			Site B		
	$q_{A,sat}$ mol kg^{-1}	b_A Pa$^{-\nu_A}$	ν_A	$q_{B,sat}$ mol kg^{-1}	b_B Pa$^{-\nu_B}$	ν_B
methanol	8.4	1.736E-43	12	3.9	2.920E-05	1
ethanol	4.6	2.372E-12	3.9	2.3	2.396E-04	1

Fitted Margules non-ideality parameters for binary mixture adsorption in ZIF-8 at 300 K. The fits are based on combining CBMC Campaigns A for each mixture.

	C / kg mol^{-1}	A_{12}	A_{21}
water/methanol	1.577	-0.946	-1.098
water/ethanol	1.252	-2.636	-0.654

CBMC data for mixture adsorption and RAST analysis

Table S11. Dual-site Langmuir-Freundlich parameters for adsorption of water, methanol, and ethanol at 298 K in ZIF-71. The fit parameters are based on the CBMC simulations of pure component isotherms of Nalaparaju et al.[7]

Adsorbate	Site A			Site B		
	$q_{A,sat}$ mol kg^{-1}	b_A Pa$^{-\nu_A}$	ν_A	$q_{B,sat}$ mol kg^{-1}	b_B Pa$^{-\nu_B}$	ν_B
water	20	2.626E-63	14	0.45	4.290E-06	1
methanol	5.8	5.159E-63	15	3.2	2.973E-05	1
ethanol	2.9	5.674E-46	12.6	3	1.285E-03	0.81

CBMC data for mixture adsorption and RAST analysis

Table S12. Dual-site Langmuir parameters for pure components CO_2, and C_3H_8 at 300 K in NaX zeolite containing 86 Na^+/uc with Si/Al=1.23. The fit parameters are based on the CBMC simulations of pure component isotherms.

	Site A		Site B	
	$q_{A,sat}$ mol kg^{-1}	b_A Pa^{-1}	$q_{B,sat}$ mol kg^{-1}	b_B Pa^{-1}
CO_2	1.7	1.39×10^{-5}	4.2	4.78×10^{-4}
C_3H_8	3.1	8.91×10^{-4}	0.65	4.09×10^{-6}

Fitted Margules non-ideality parameters for binary CO_2/C_3H_8 mixture adsorption in NaX at 300 K.

	C / kg mol^{-1}	A_{12}	A_{21}
CO_2/C_3H_8 in NaX	1.066	-1.609	-1.194

Table S13. Dual-site Langmuir-Freundlich parameters for guest molecules in MFI at 300 K. To convert from molecules uc^{-1} to mol kg^{-1}, multiply by 0.173367.

	Site A			Site B		
	$\Theta_{A,sat}$ molecules uc^{-1}	b_A $Pa^{-\nu_A}$	ν_A dimensionless	$\Theta_{B,sat}$ molecules uc^{-1}	b_B $Pa^{-\nu_A}$	ν_B dimensionless
nC4H10	1.5	2.24E-03	0.57	8.7	9.75E-03	1.12
iso-C4H10	4	2.29E-02	1	6	2.87E-05	1
nC6H14	6.6	7.08E-01	0.83	1.4	1.66E+01	1.5
2MP	4	4.513	1.05	4	7.92E-05	1.13

Margules non-ideality parameters for binary mixtures in all-silica MFI zeolite at 300 K.

	C / kg mol^{-1}	A_{12}	A_{21}
nC4/iC4	0.190	0.578	-3.175
nC6/2MP	0.386	1.340	1.580

CBMC data for mixture adsorption and RAST analysis

Table S14. Dual-site Langmuir-Freundlich parameters for adsorption of methanol, and n-hexane at 313 K in CuBTC. The unary isotherm fits are based on the data scanned from Figure 2 of van Assche et al.[41]

Adsorbate	Site A			Site B		
	$q_{A,sat}$ mol kg^{-1}	b_A Pa$^{-\nu_A}$	ν_A dimensionless	$q_{B,sat}$ mol kg^{-1}	b_B Pa$^{-\nu_B}$	ν_B dimensionless
methanol	13.5	8.57×10^{-3}	0.62	6.5	2.5×10^{-3}	1.56
n-hexane	2.3	1.06×10^{-1}	0.6	2.8	4.81×10^{-8}	6.85

The fitted Margules parameters using the data scanned from Figure 4 of van Assche et al.[41] The units of C are kg mol^{-1}.

	C / kg mol^{-1}	A_{12}	A_{21}
Methanol/n-hexane	0.305	-5.336	-13.279

CBMC data for mixture adsorption and RAST analysis

Table S15. Langmuir-Freundlich fits of the unary isotherms of toluene, and 1-propanol in DAY-13 zeolite at 298 K. The parameters were obtained by fitting the unary isotherm data in Table 1 of Sakuth et al.[42]

	q_{sat} mol kg^{-1}	b Pa$^{-\nu}$	ν dimensionless
toluene	2.26	0.2585	0.74
1-propanol	3.26	0.09743	0.56

The fitted Margules parameters using the data from Table 3 of Sakuth et al.[42] for toluene/1-propanol mixture adsorption in DAY-13.

	C / kg mol^{-1}	A_{12}	A_{21}
Toluene/1-propanol	1.100	-4.652	0.195

CBMC data for mixture adsorption and RAST analysis

Table S16. Langmuir fits of the unary isotherms of 1-butanol, and p-xylene in Y zeolite (sample A) at 298 K. The parameters correspond to those presented in Table 4 of Takeuchi et al.[44] for dry conditions in the vapor phase.

	q_{sat} mol kg^{-1}	b Pa^{-1}
1-butanol	2.17	0.2239
p-xylene	1.39	0.5268

Table S17. Dual-site Langmuir-Freundlich parameters for linear alkanes in NaX zeolite at 300 K. Per unit cell of NaX zeolite we have 106 Si, 86 Al, 86 Na^+ with Si/Al=1.23. To convert from molecules uc^{-1} to mol kg^{-1}, multiply by 0.074524437.

	Site A			Site B		
	$\Theta_{A,sat}$ molecules uc^{-1}	b_A $Pa^{-\nu}$	ν_A dimensionless	$\Theta_{B,sat}$ molecules uc^{-1}	b_B $Pa^{-\nu}$	ν_B dimensionless
CH4	70	2.460E-06	1	24.5	6.840E-09	1.1
C2H6	56	1.233E-05	1.1	17	9.240E-06	0.72
C3H8	32	1.863E-04	1.35	20	1.248E-03	0.61

CBMC data for mixture adsorption and RAST analysis

Table S18. Dual-site Langmuir parameters for pure components CO_2, and CH_4 at 300 K in NaX zeolite containing 86 Na^+/uc with Si/Al=1.23. The fit parameters are based on the CBMC simulations of pure component isotherms.

	Site A		Site B	
	$q_{A,sat}$ mol kg^{-1}	b_A Pa^{-1}	$q_{B,sat}$ mol kg^{-1}	b_B Pa^{-1}
CO_2	1.7	1.39×10^{-5}	4.2	4.78×10^{-4}
CH_4	5.8	2.07×10^{-6}		

Fitted Margules non-ideality parameters for binary CO_2/CH_4 mixture adsorption in NaX at 300 K.

	C / kg mol^{-1}	A_{12}	A_{21}
CO_2/CH_4 in NaX	1.021	-0.632	-0.693

CBMC data for mixture adsorption and RAST analysis

Table S19. Dual-site Langmuir-Freundlich parameters for pure components CO_2, and C_3H_8 at 300 K in LTA-4A zeolite (96 Si, 96 Al, 96 Na^+, Si/Al=1). The fit parameters are based on the CBMC simulations of pure component isotherms.

	Site A			Site B		
	$q_{A,sat}$ mol kg^{-1}	b_A $Pa^{-\nu_A}$	ν_A dimensionless	$q_{B,sat}$ mol kg^{-1}	b_B $Pa^{-\nu_B}$	ν_B dimensionless
CO_2	3.1	4.13×10^{-4}	1	1.7	2.095×10^{-7}	1
C_3H_8	2.5	2.21×10^{-2}	1	0.9	6.18×10^{-6}	1

Fitted Margules non-ideality parameters for binary CO_2/C_3H_8 mixture adsorption in LTA-4A at 300 K.

	C / kg mol^{-1}	A_{12}	A_{21}
CO_2/C_3H_8 in LTA-4A	0.899	-3.574	-0.521

Table S20. Dual-site Langmuir-Freundlich parameters for linear alkanes in MFI at 300 K. To convert from molecules uc^{-1} to mol kg^{-1}, multiply by 0.173367.

	Site A			Site B		
	$\Theta_{A,sat}$ molecules uc^{-1}	b_A $Pa^{-\nu_A}$	ν_A dimensionless	$\Theta_{B,sat}$ molecules uc^{-1}	b_B $Pa^{-\nu_A}$	ν_B dimensionless
CH_4	7	5.00E-09	1	16	3.10E-06	1
C_2H_6	3.3	4.08E-07	1	13	7.74E-05	1
C_3H_8	1.4	3.35E-04	0.67	10.7	6.34E-04	1.06

6.11 List of Figures for CBMC data for mixture adsorption and RAST analysis

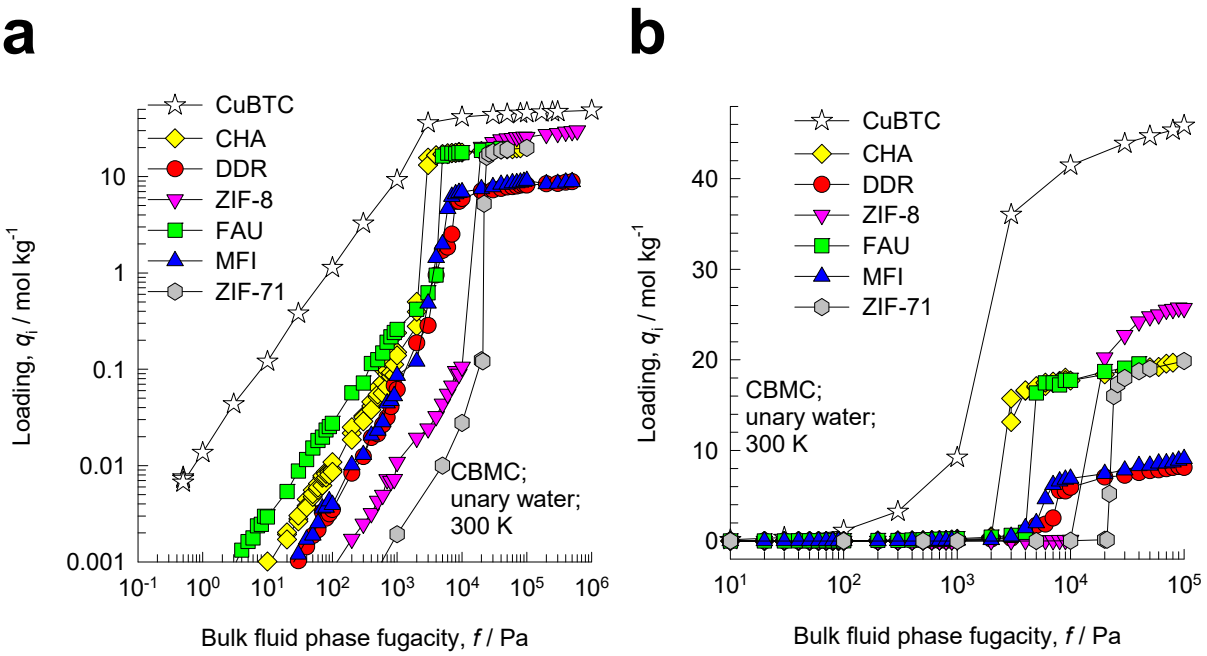

Figure S23. (a, b) CBMC simulations of unary water isotherms in different microporous host materials, plotted as function of the fugacity of water in the bulk fluid phase. The *y*-axes are plotted in (a) logarithmic, and (b) linear scales.

CBMC data for mixture adsorption and RAST analysis

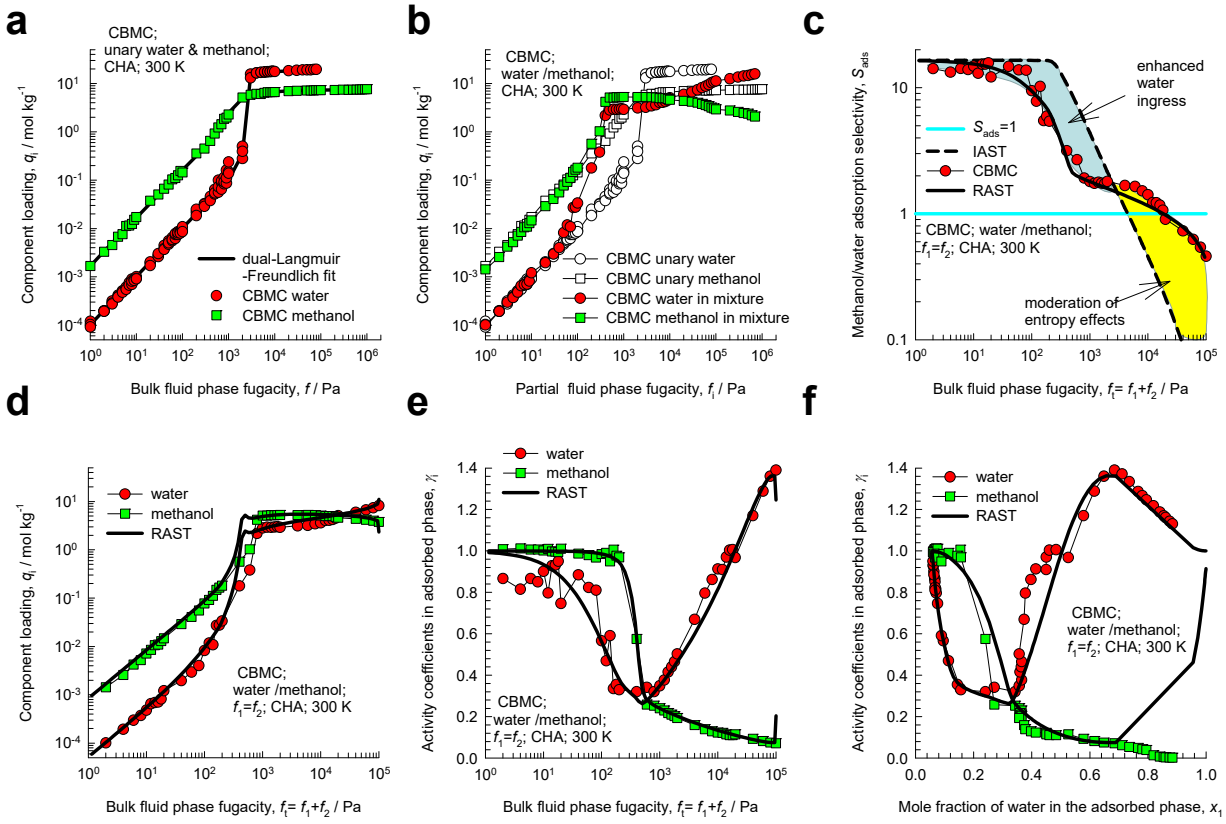

Figure S24. CBMC simulation data and analysis for Campaign A (y_1= 0.5) for water/methanol mixture in CHA at 300 K. (a) Unary isotherms and fits. (b) Component loadings in mixture compared with CBMC simulations of unary isotherms. (c) CBMC data for alcohol/water selectivity compared with IAST and RAST estimates. (d) CBMC data for component loadings in mixture compared with RAST estimates. (e. f) Activity coefficients from CBMC compared with RAST model calculations.

CBMC data for mixture adsorption and RAST analysis

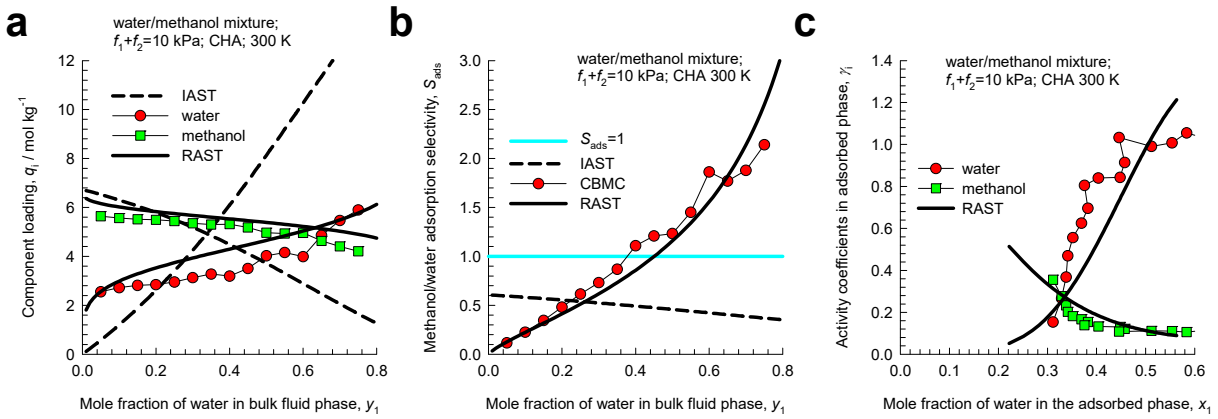

Figure S25. CBMC simulation data and analysis for Campaign B (f_t = 10 kPa) for water/methanol mixture in CHA at 300 K. CBMC data on (a) component loadings, and (b) alcohol/water selectivity compared with IAST and RAST estimates. (c) Activity coefficients from CBMC compared with RAST model calculations.

CBMC data for mixture adsorption and RAST analysis

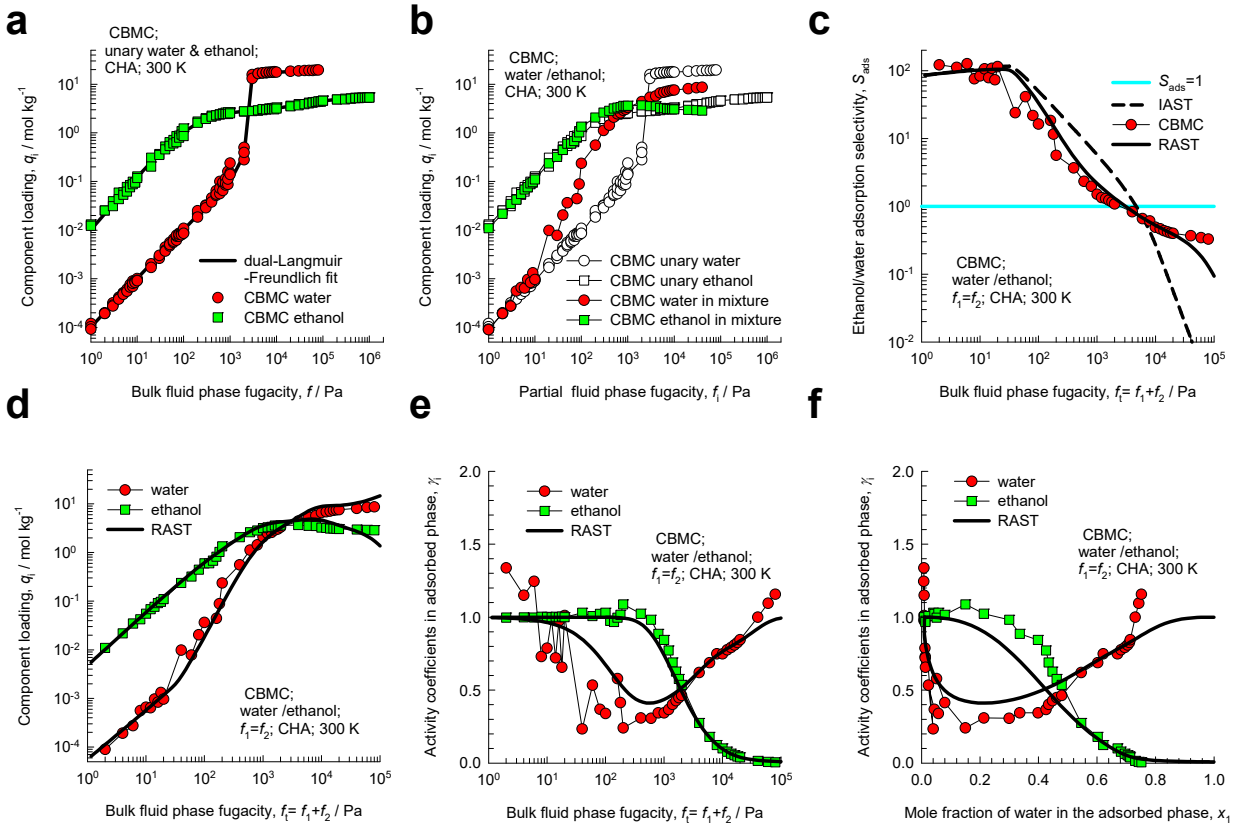

Figure S26. CBMC simulation data and analysis for Campaign A (y_1= 0.5) for water/ethanol mixture in CHA at 300 K. (a) Unary isotherms and fits. (b) Component loadings in mixture compared with CBMC simulations of unary isotherms. (c) CBMC data for alcohol/water selectivity compared with IAST and RAST estimates. (d) CBMC data for component loadings in mixture compared with RAST estimates. (e. f) Activity coefficients from CBMC compared with RAST model calculations.

CBMC data for mixture adsorption and RAST analysis

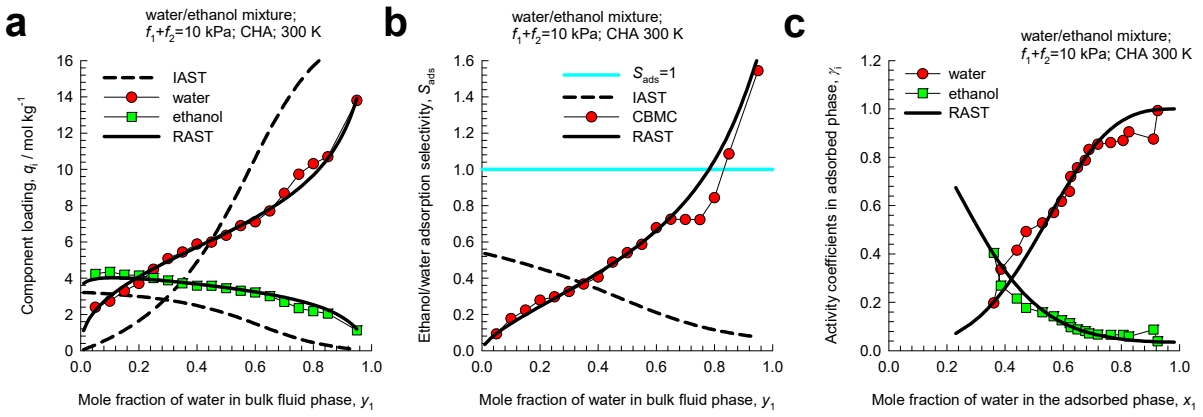

Figure S27. CBMC simulation data and analysis for Campaign B (f_t = 10 kPa) for water/ethanol mixture in CHA at 300 K. CBMC data on (a) component loadings, and (b) alcohol/water selectivity compared with IAST and RAST estimates. (c) Activity coefficients from CBMC compared with RAST model calculations.

CBMC data for mixture adsorption and RAST analysis

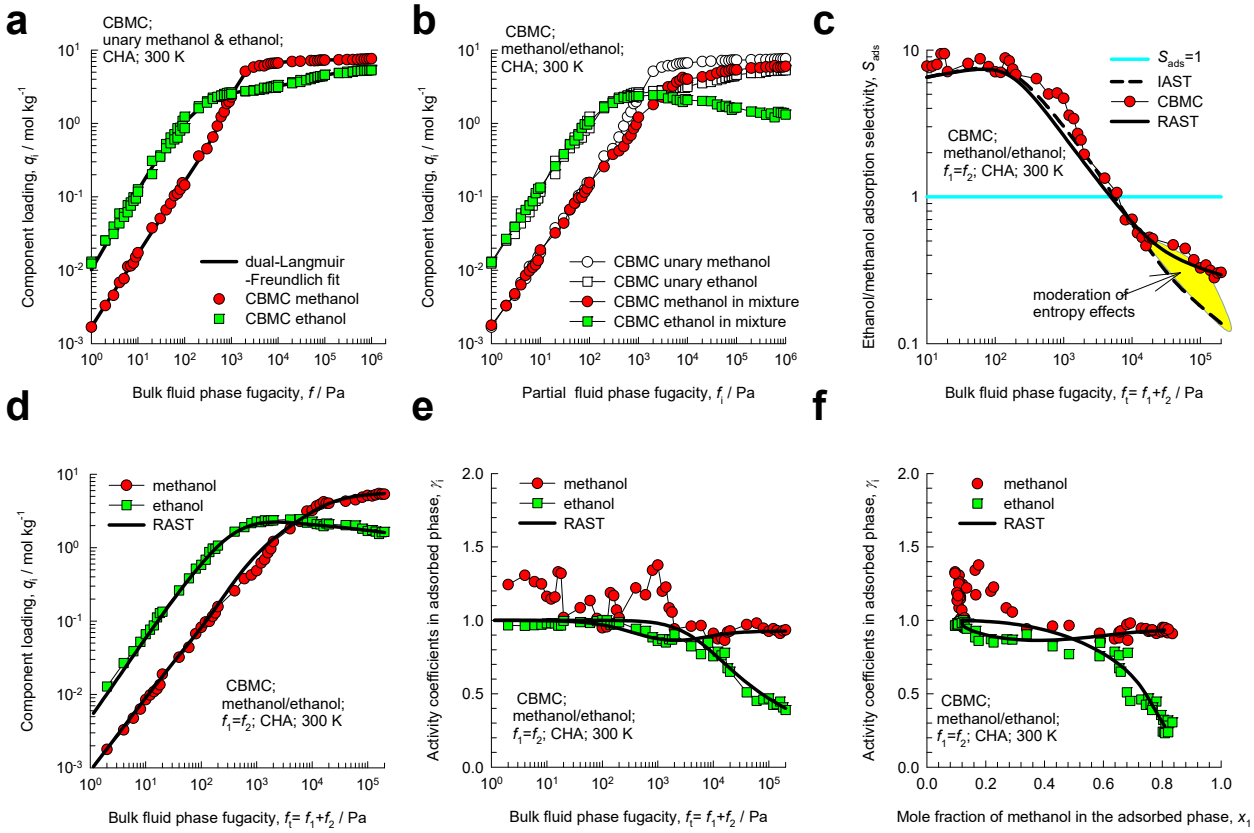

Figure S28. CBMC simulation data and analysis for Campaign A (y_1= 0.5) for methanol/ethanol mixture in CHA at 300 K. (a) Unary isotherms and fits. (b) Component loadings in mixture compared with CBMC simulations of unary isotherms. (c) CBMC data for alcohol/water selectivity compared with IAST and RAST estimates. (d) CBMC data for component loadings in mixture compared with RAST estimates. (e. f) Activity coefficients from CBMC compared with RAST model calculations.

CBMC data for mixture adsorption and RAST analysis

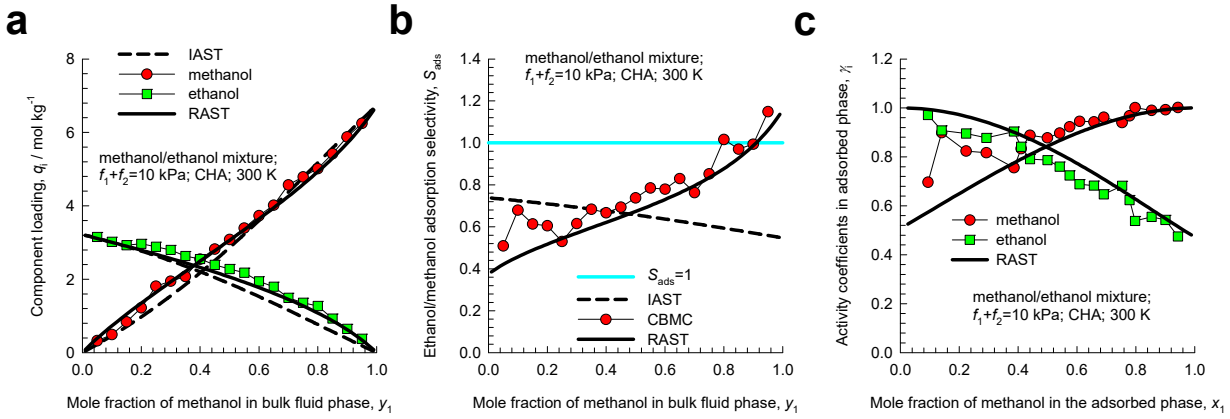

Figure S29. CBMC simulation data and analysis for Campaign B (f_t = 10 kPa) for methanol/ethanol mixture in CHA at 300 K. CBMC data on (a) component loadings, and (b) ethanol/methanol selectivity compared with IAST and RAST estimates. (c) Activity coefficients from CBMC compared with RAST model calculations.

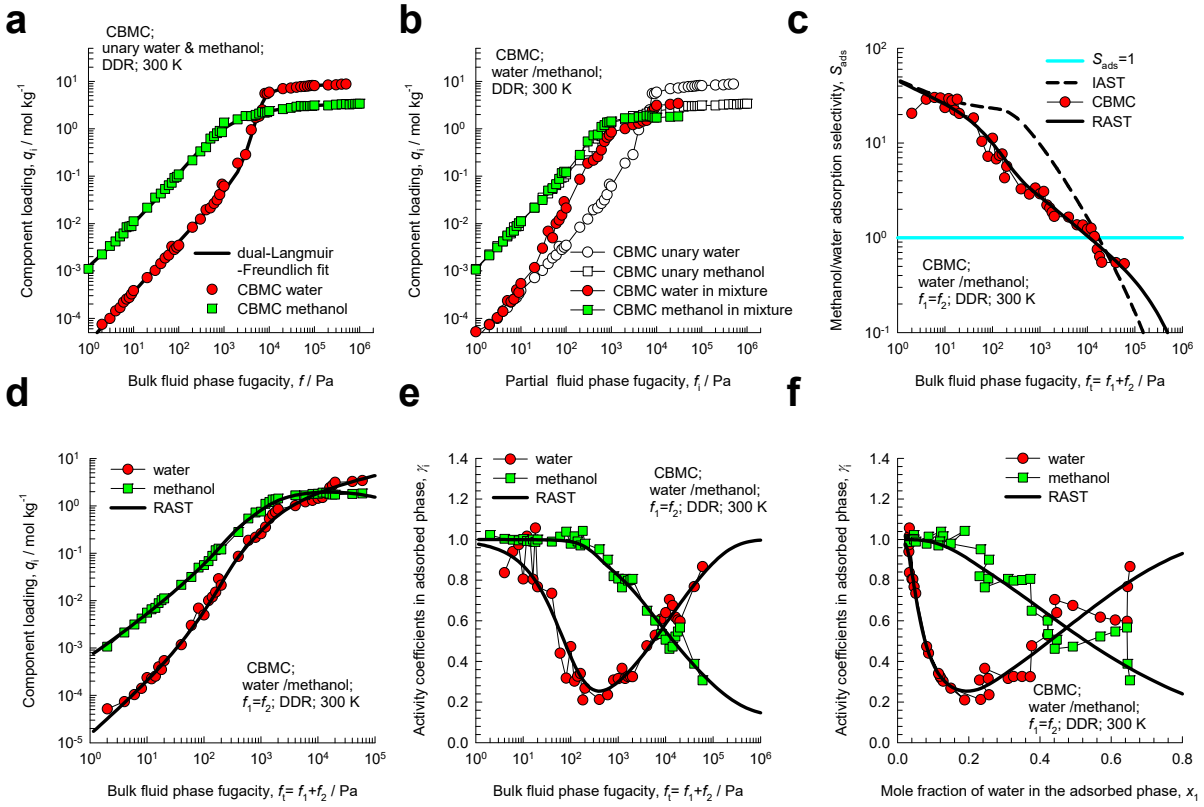

Figure S30. CBMC simulation data and analysis for Campaign A (y_1= 0.5) for water/methanol mixture in DDR at 300 K. (a) Unary isotherms and fits. (b) Component loadings in mixture compared with CBMC simulations of unary isotherms. (c) CBMC data for alcohol/water selectivity compared with IAST and RAST estimates. (d) CBMC data for component loadings in mixture compared with RAST estimates. (e. f) Activity coefficients from CBMC compared with RAST model calculations. For the RAST calculations, the Margules parameters were determined by fitting only the Campaign A CBMC data, as reported in Table S5.

CBMC data for mixture adsorption and RAST analysis

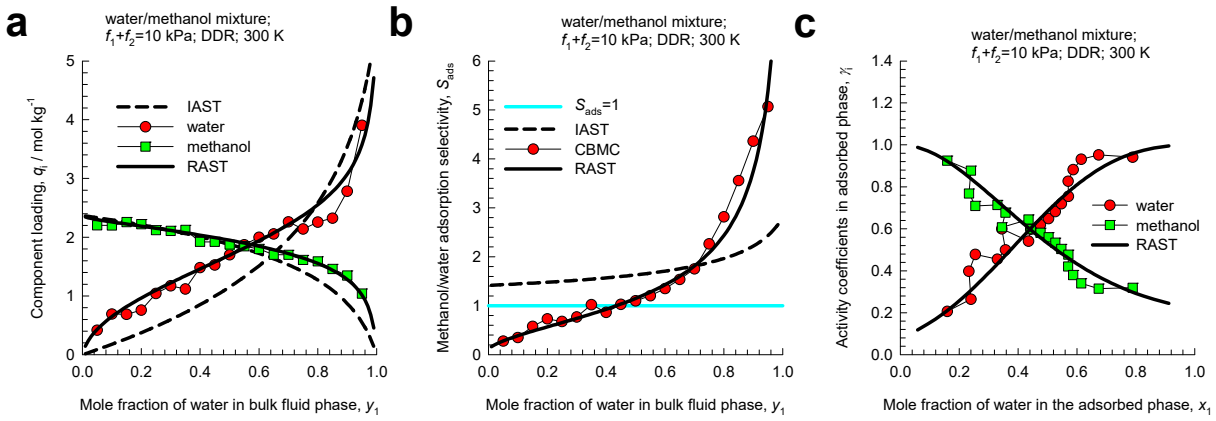

Figure S31. CBMC simulation data and analysis for Campaign B (f_t = 10 kPa) for water/methanol mixture in DDR at 300 K. CBMC data on (a) component loadings, and (b) alcohol/water selectivity compared with IAST and RAST estimates. (c) Activity coefficients from CBMC compared with RAST model calculations. For the RAST calculations, the Margules parameters were determined by fitting only the Campaign B CBMC data.

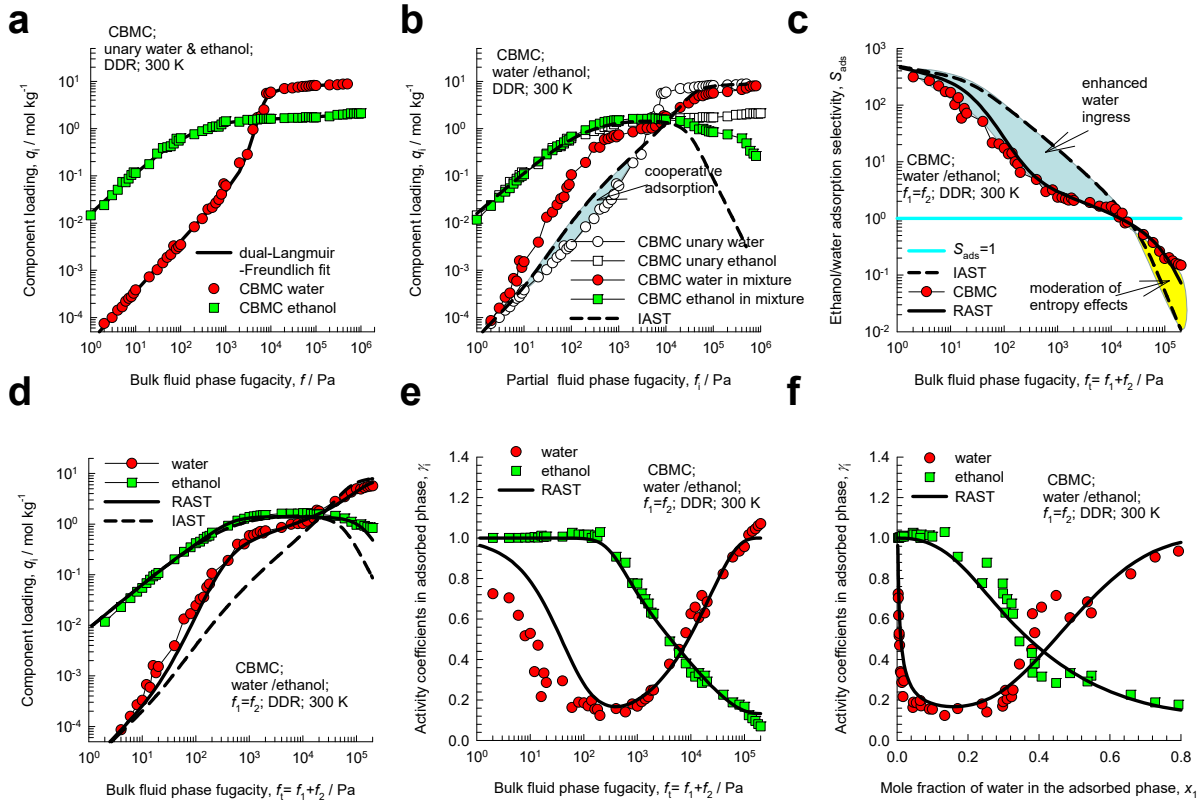

Figure S32. CBMC simulation data and analysis for Campaign A (y_1= 0.5) for water/ethanol mixture in DDR at 300 K. (a) Unary isotherms and fits. (b) Component loadings in mixture compared with CBMC simulations of unary isotherms. (c) CBMC data for alcohol/water selectivity compared with IAST and RAST estimates. (d) CBMC data for component loadings in mixture compared with RAST estimates. (e. f) Activity coefficients from CBMC compared with RAST model calculations.

CBMC data for mixture adsorption and RAST analysis

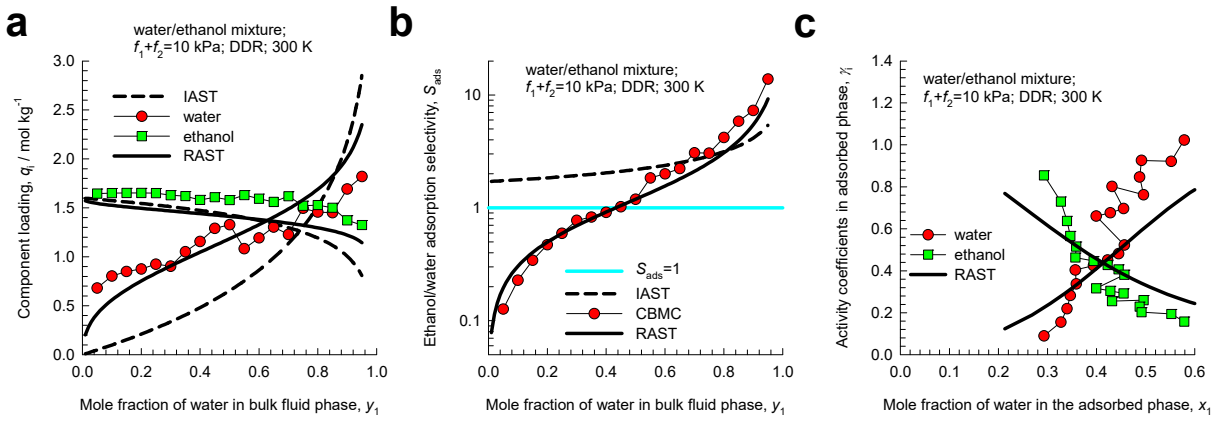

Figure S33. CBMC simulation data and analysis for Campaign B (f_t = 10 kPa) for water/ethanol mixture in DDR at 300 K. CBMC data on (a) component loadings, and (b) alcohol/water selectivity compared with IAST and RAST estimates. (c) Activity coefficients from CBMC compared with RAST model calculations.

CBMC data for mixture adsorption and RAST analysis

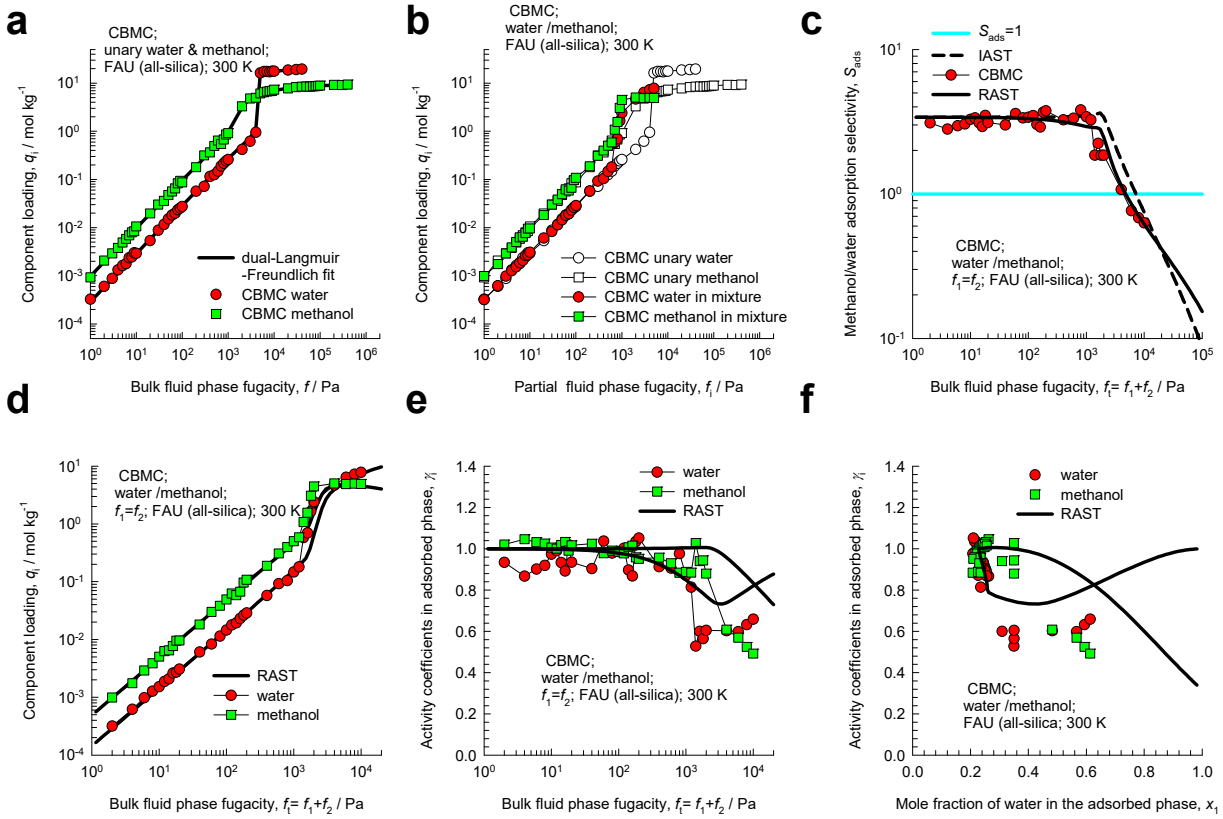

Figure S34. CBMC simulation data and analysis for Campaign A (y_1= 0.5) for water/methanol mixture in FAU (all-silica) at 300 K. (a) Unary isotherms and fits. (b) Component loadings in mixture compared with CBMC simulations of unary isotherms. (c) CBMC data for alcohol/water selectivity compared with IAST and RAST estimates. (d) CBMC data for component loadings in mixture compared with RAST estimates. (e. f) Activity coefficients from CBMC compared with RAST model calculations.

CBMC data for mixture adsorption and RAST analysis

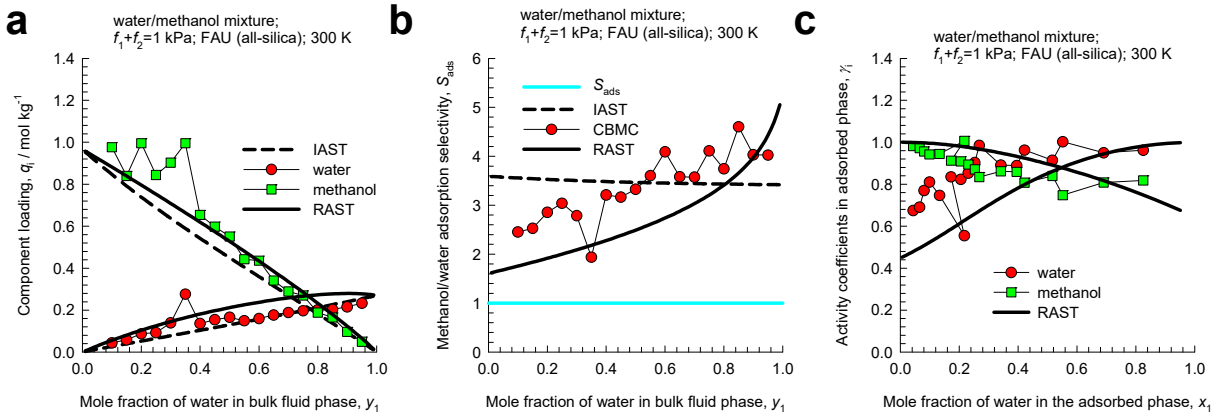

Figure S35. CBMC simulation data and analysis for Campaign B (f_t = 1 kPa) for water/methanol mixture in FAU (all-silica) at 300 K. CBMC data on (a) component loadings, and (b) alcohol/water selectivity compared with IAST and RAST estimates. (c) Activity coefficients from CBMC compared with RAST model calculations.

CBMC data for mixture adsorption and RAST analysis

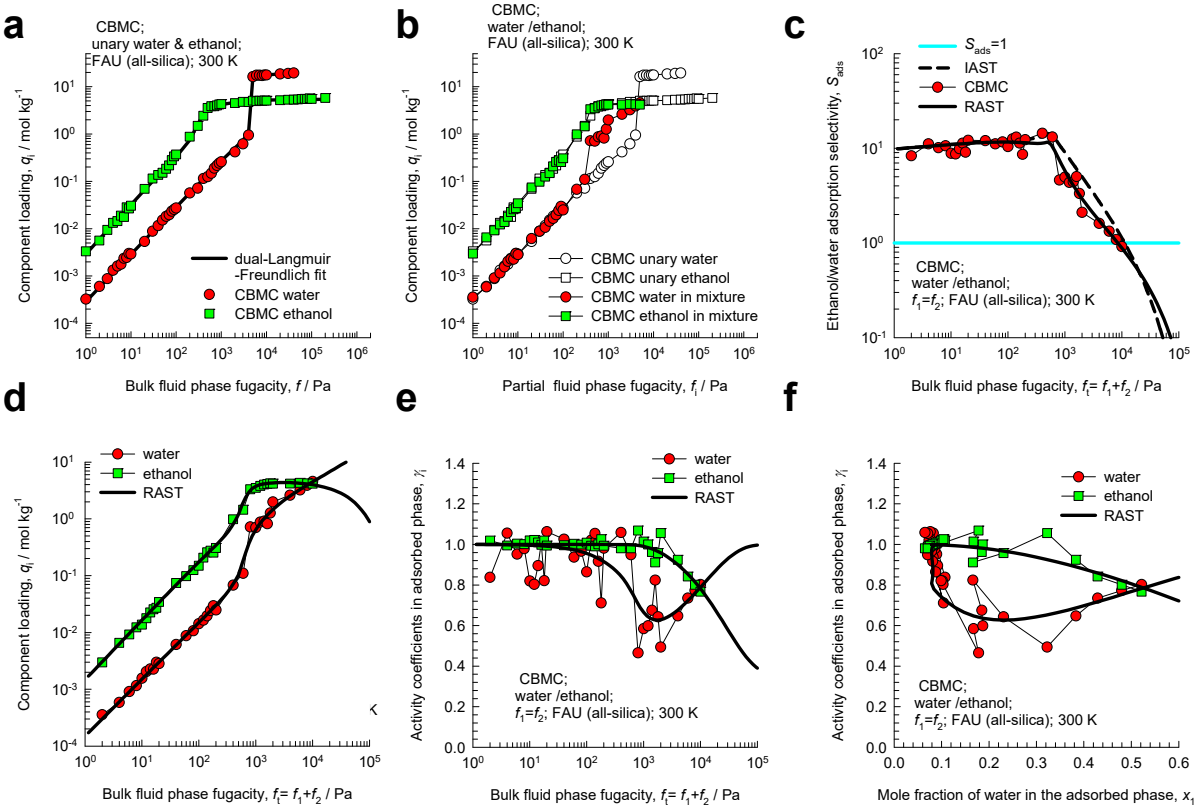

Figure S36. CBMC simulation data and analysis for Campaign A (y_1= 0.5) for water/ethanol mixture in FAU (all-silica) at 300 K. (a) Unary isotherms and fits. (b) Component loadings in mixture compared with CBMC simulations of unary isotherms. (c) CBMC data for alcohol/water selectivity compared with IAST and RAST estimates. (d) CBMC data for component loadings in mixture compared with RAST estimates. (e. f) Activity coefficients from CBMC compared with RAST model calculations.

CBMC data for mixture adsorption and RAST analysis

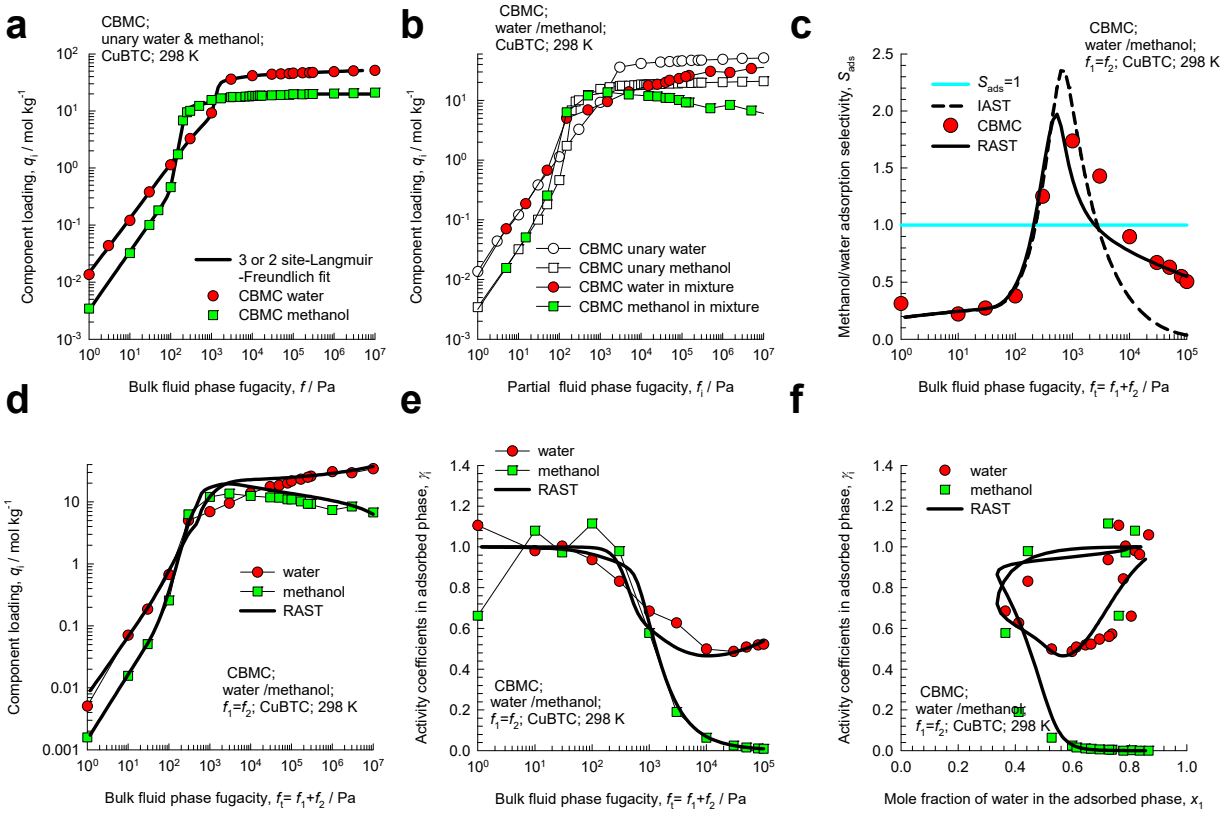

Figure S37. CBMC simulation data and analysis for Campaign A (y_1= 0.5) for water/methanol mixture in CuBTC at 298 K. (a) Unary isotherms and fits. (b) Component loadings in mixture compared with CBMC simulations of unary isotherms. (c) CBMC data for alcohol/water selectivity compared with IAST and RAST estimates. (d) CBMC data for component loadings in mixture compared with RAST estimates. (e. f) Activity coefficients from CBMC compared with RAST model calculations.

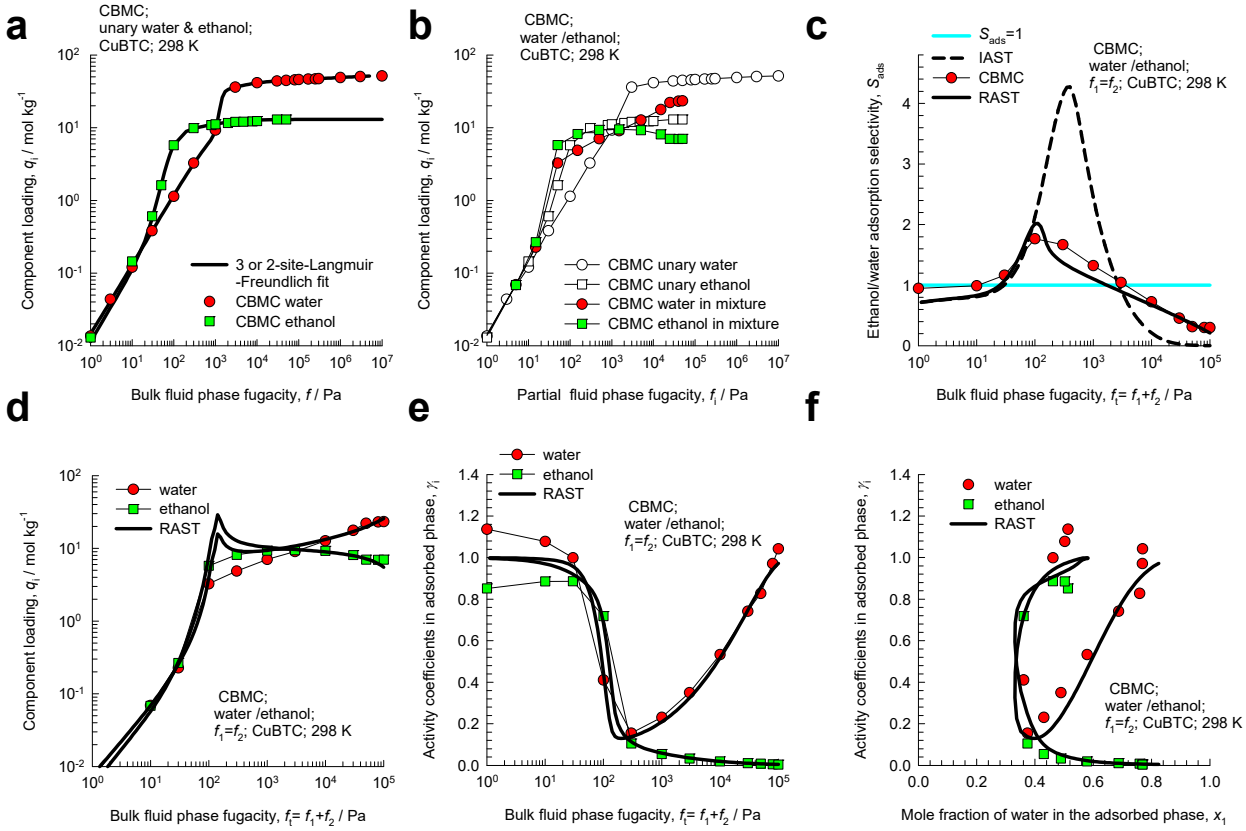

Figure S38. CBMC simulation data and analysis for Campaign A (y_1= 0.5) for water/ethanol mixture in CuBTC at 298 K. (a) Unary isotherms and fits. (b) Component loadings in mixture compared with CBMC simulations of unary isotherms. (c) CBMC data for alcohol/water selectivity compared with IAST and RAST estimates. (d) CBMC data for component loadings in mixture compared with RAST estimates. (e. f) Activity coefficients from CBMC compared with RAST model calculations.

CBMC data for mixture adsorption and RAST analysis

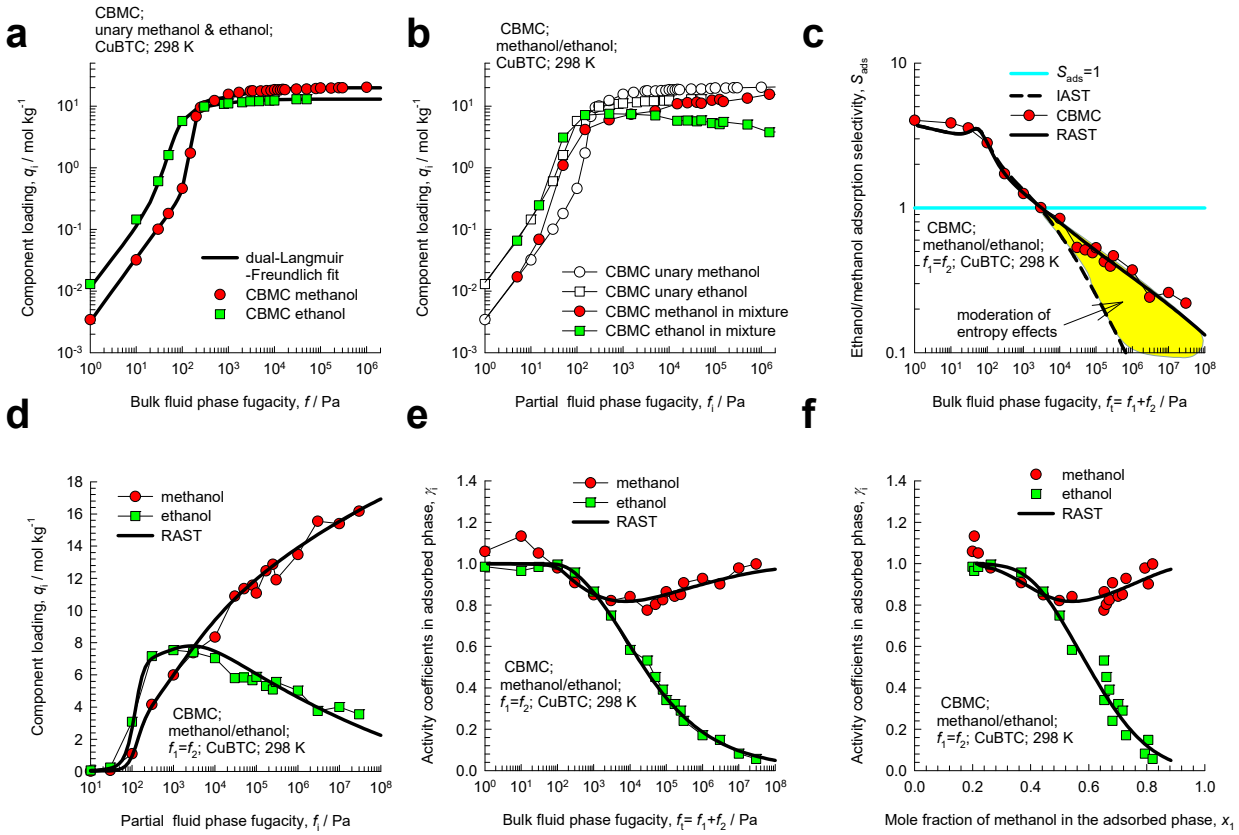

Figure S39. CBMC simulation data and analysis for Campaign A (y_1= 0.5) for methanol/ethanol mixture in CuBTC at 298 K. (a) Unary isotherms and fits. (b) Component loadings in mixture compared with CBMC simulations of unary isotherms. (c) CBMC data for ethanol/methanol selectivity compared with IAST and RAST estimates. (d) CBMC data for component loadings in mixture compared with RAST estimates. (e. f) Activity coefficients from CBMC compared with RAST model calculations.

.

CBMC data for mixture adsorption and RAST analysis

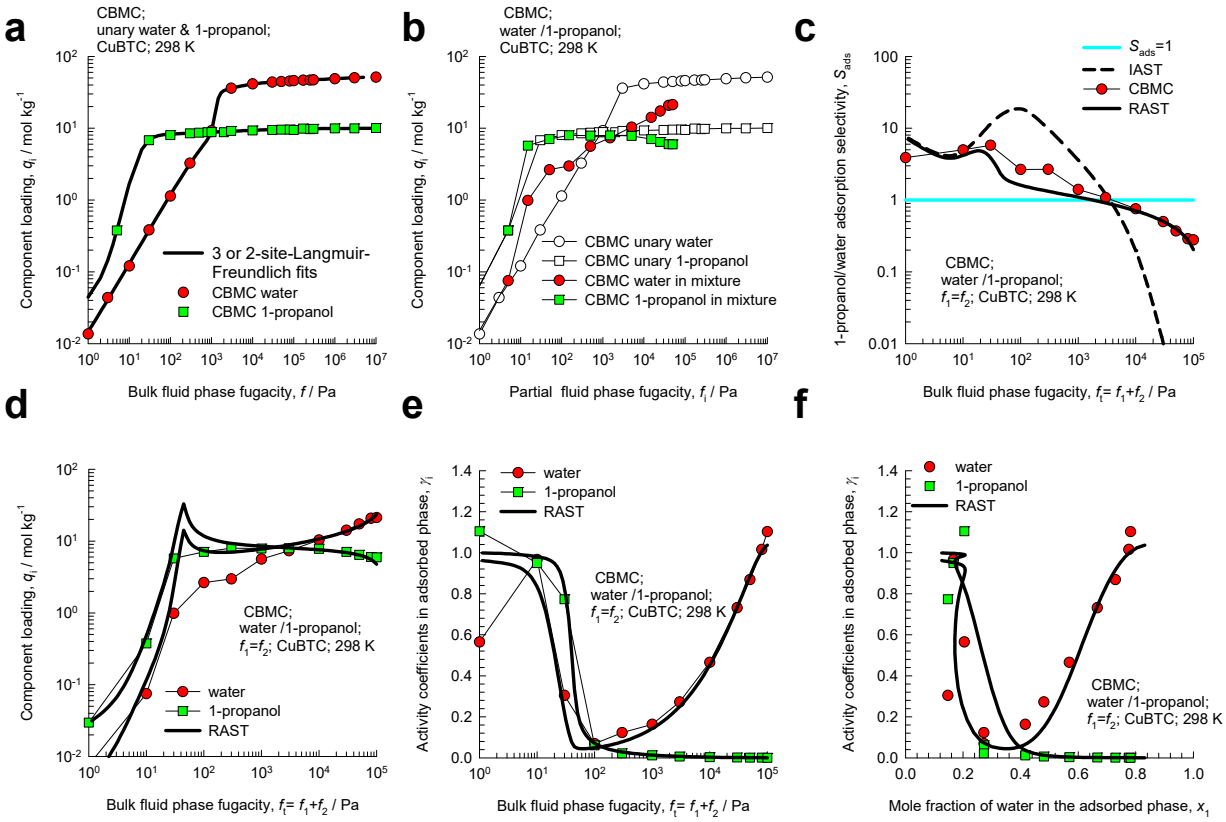

Figure S40. CBMC simulation data and analysis for Campaign A (y_1= 0.5) for water/1-propanol mixture in CuBTC at 298 K. (a) Unary isotherms and fits. (b) Component loadings in mixture compared with CBMC simulations of unary isotherms. (c) CBMC data for alcohol/water selectivity compared with IAST and RAST estimates. (d) CBMC data for component loadings in mixture compared with RAST estimates. (e. f) Activity coefficients from CBMC compared with RAST model calculations.

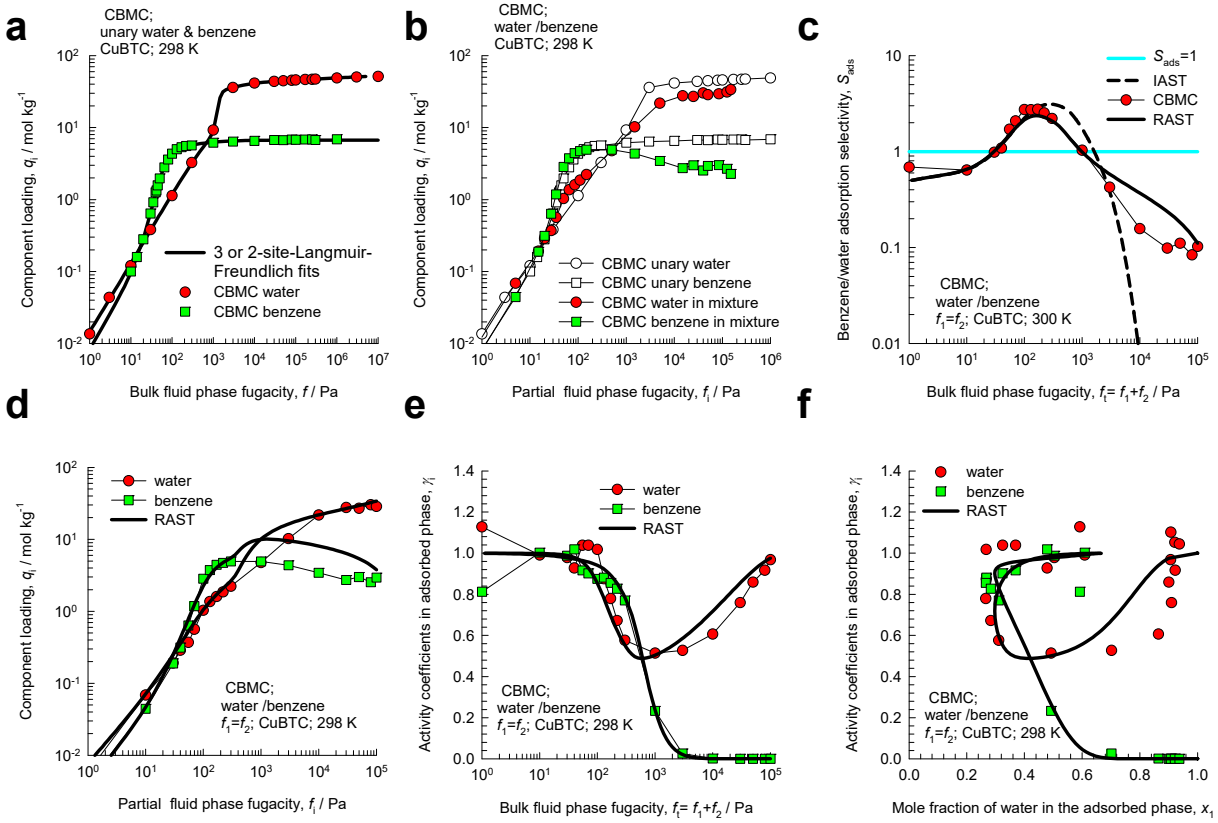

Figure S41. CBMC simulation data and analysis for Campaign A (y_1= 0.5) for water/benzene mixture in CuBTC at 298 K. (a) Unary isotherms and fits. (b) Component loadings in mixture compared with CBMC simulations of unary isotherms. (c) CBMC data for benzene/water selectivity compared with IAST and RAST estimates. (d) CBMC data for component loadings in mixture compared with RAST estimates. (e. f) Activity coefficients from CBMC compared with RAST model calculations.

CBMC data for mixture adsorption and RAST analysis

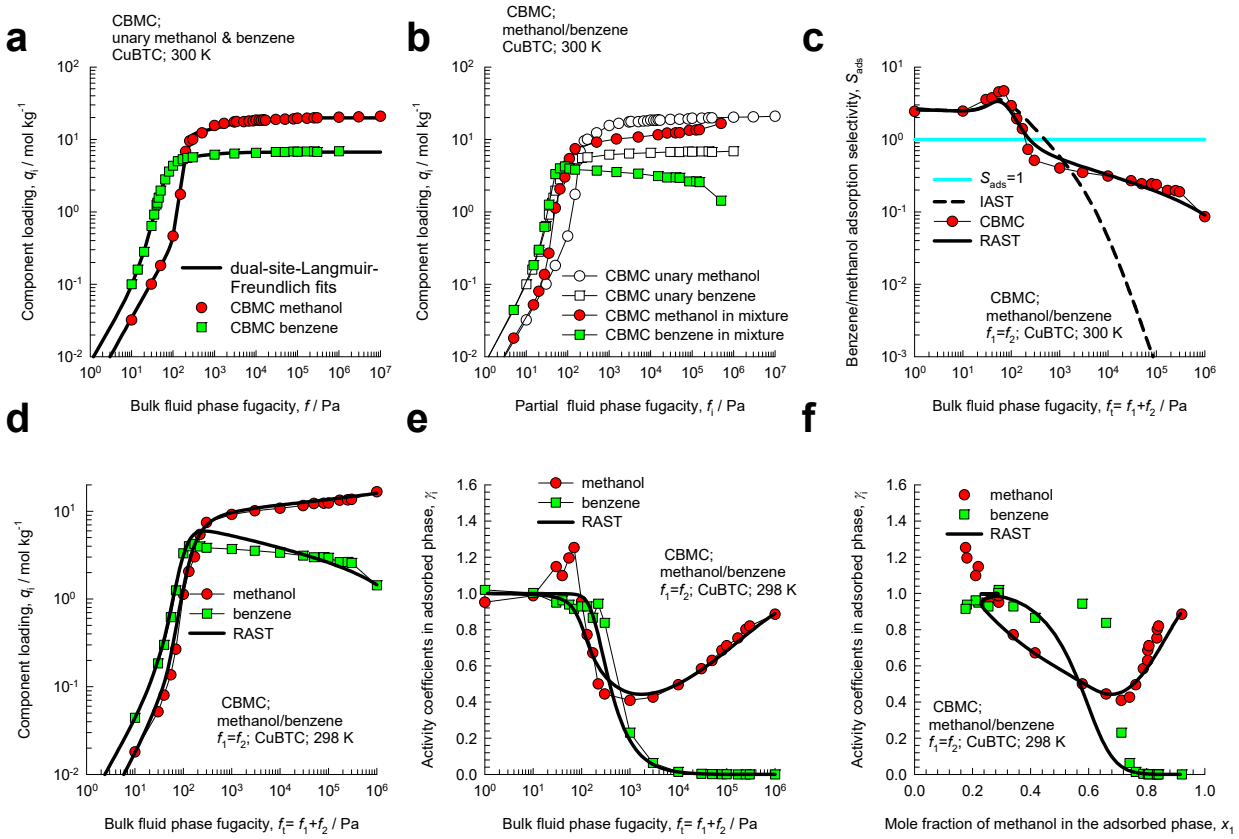

Figure S42. CBMC simulation data and analysis for Campaign A (y_1= 0.5) for methanol/benzene mixture in CuBTC at 298 K. (a) Unary isotherms and fits. (b) Component loadings in mixture compared with CBMC simulations of unary isotherms. (c) CBMC data for benzene/methanol selectivity compared with IAST and RAST estimates. (d) CBMC data for component loadings in mixture compared with RAST estimates. (e. f) Activity coefficients from CBMC compared with RAST model calculations.

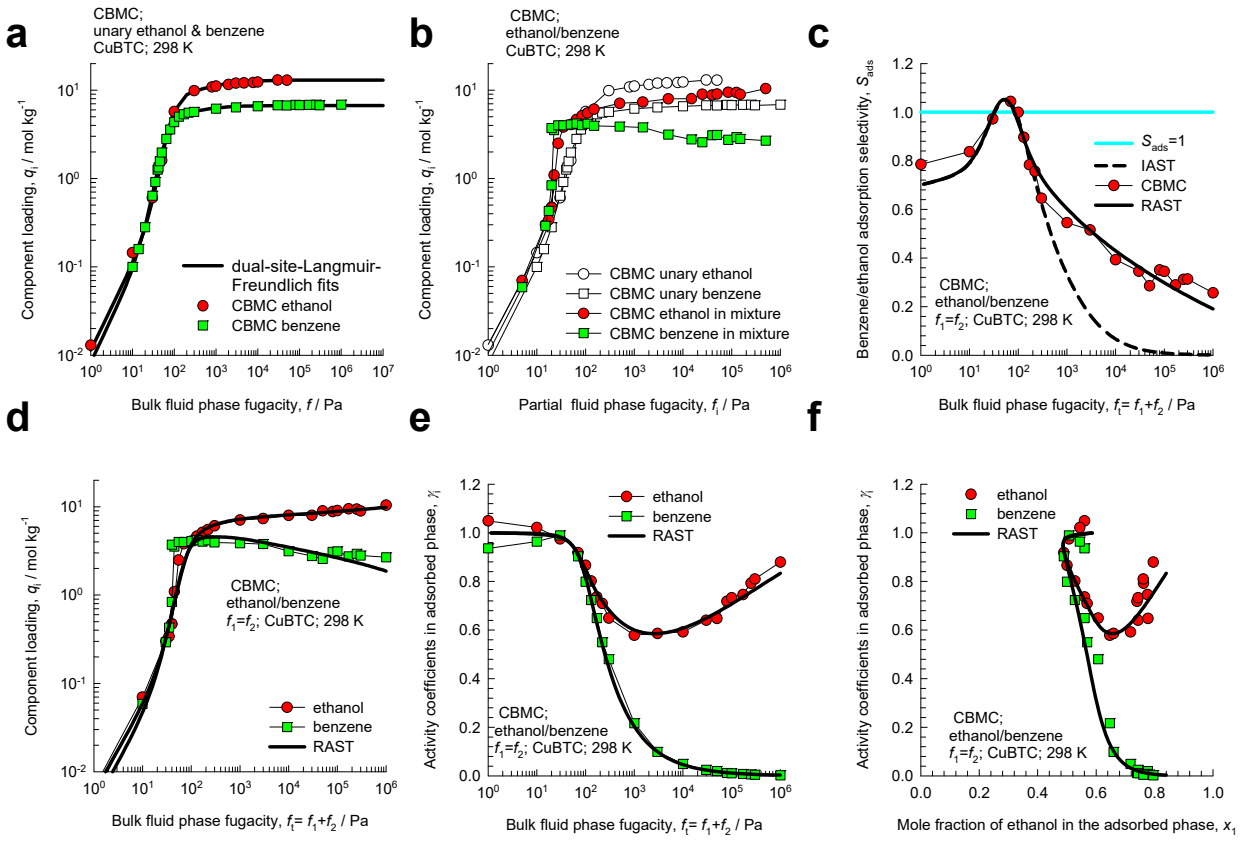

Figure S43. CBMC simulation data and analysis for Campaign A (y_1= 0.5) for ethanol/benzene mixture in CuBTC at 298 K. (a) Unary isotherms and fits. (b) Component loadings in mixture compared with CBMC simulations of unary isotherms. (c) CBMC data for benzene/ethanol selectivity compared with IAST and RAST estimates. (d) CBMC data for component loadings in mixture compared with RAST estimates. (e. f) Activity coefficients from CBMC compared with RAST model calculations.

CBMC data for mixture adsorption and RAST analysis

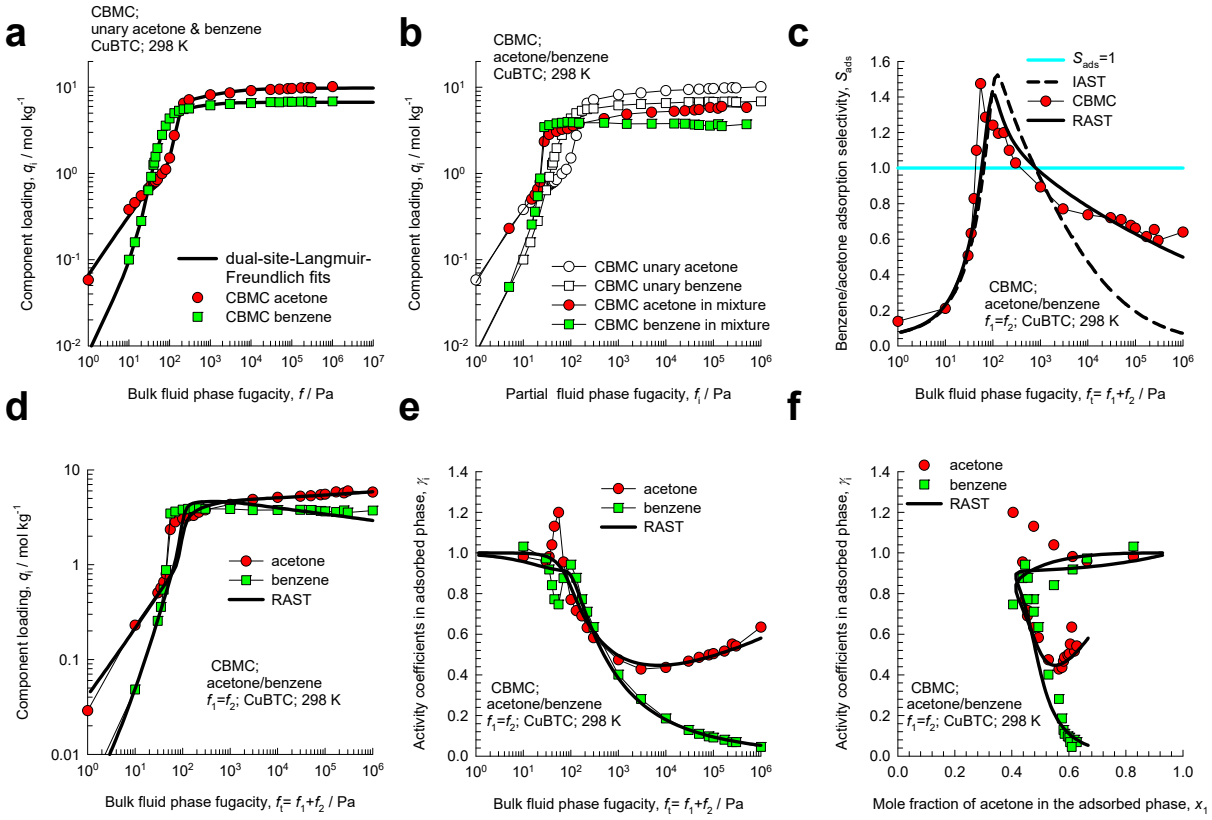

Figure S44. CBMC simulation data and analysis for Campaign A (y_1= 0.5) for acetone/benzene mixture in CuBTC at 298 K. (a) Unary isotherms and fits. (b) Component loadings in mixture compared with CBMC simulations of unary isotherms. (c) CBMC data for benzene/acetone selectivity compared with IAST and RAST estimates. (d) CBMC data for component loadings in mixture compared with RAST estimates. (e. f) Activity coefficients from CBMC compared with RAST model calculations.

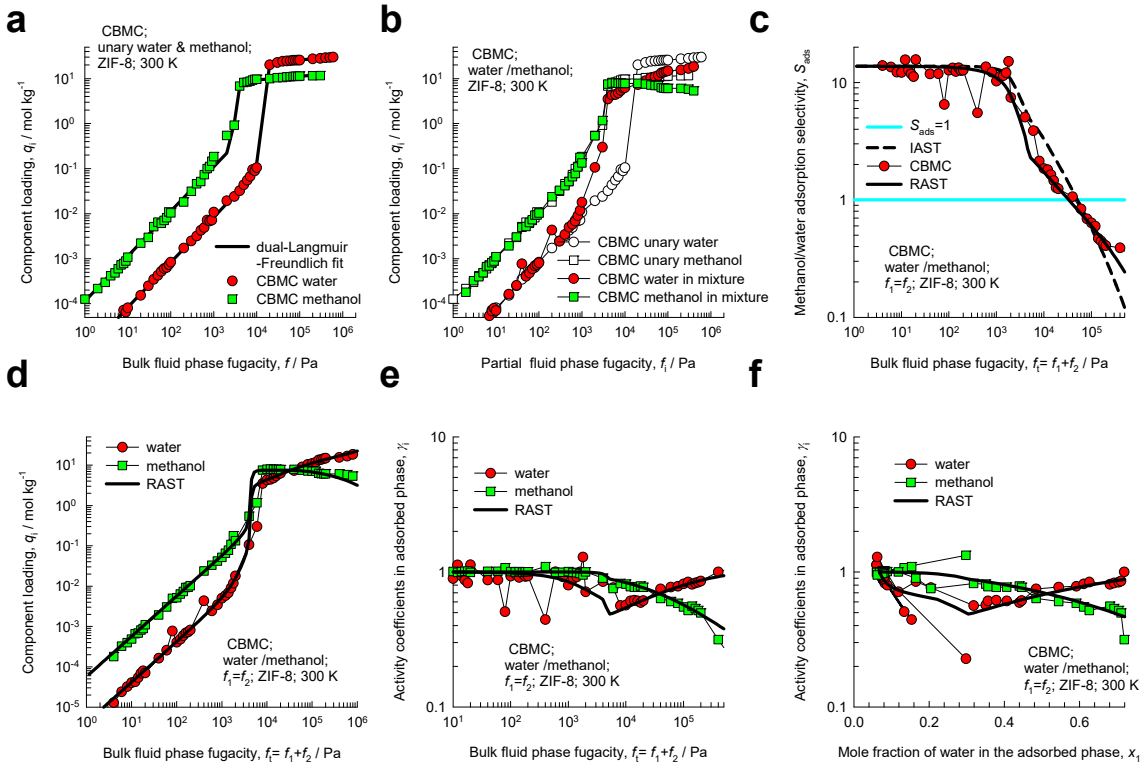

Figure S45. CBMC simulation data and analysis for Campaign A (y_1= 0.5) for water/methanol mixture adsorption in ZIF-8 at 300 K. (a) Unary isotherms and fits. (b) Component loadings in mixture compared with CBMC simulations of unary isotherms. (c) CBMC data for methanol/water selectivity compared with IAST and RAST estimates. (d) CBMC data for component loadings in mixture compared with RAST estimates. (e. f) Activity coefficients from CBMC compared with RAST model calculations.

CBMC data for mixture adsorption and RAST analysis

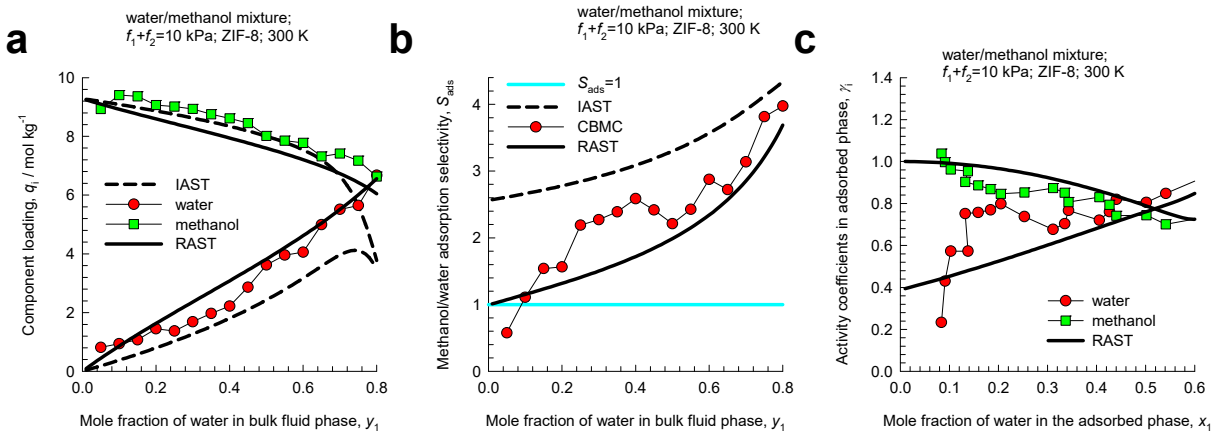

Figure S46. CBMC simulation data and analysis for Campaign B (f_t = 10 kPa) for water/methanol mixture in ZIF-8 at 300 K. CBMC data on (a) component loadings, and (b) methanol/water selectivity compared with IAST and RAST estimates. (c) Activity coefficients from CBMC data.

CBMC data for mixture adsorption and RAST analysis

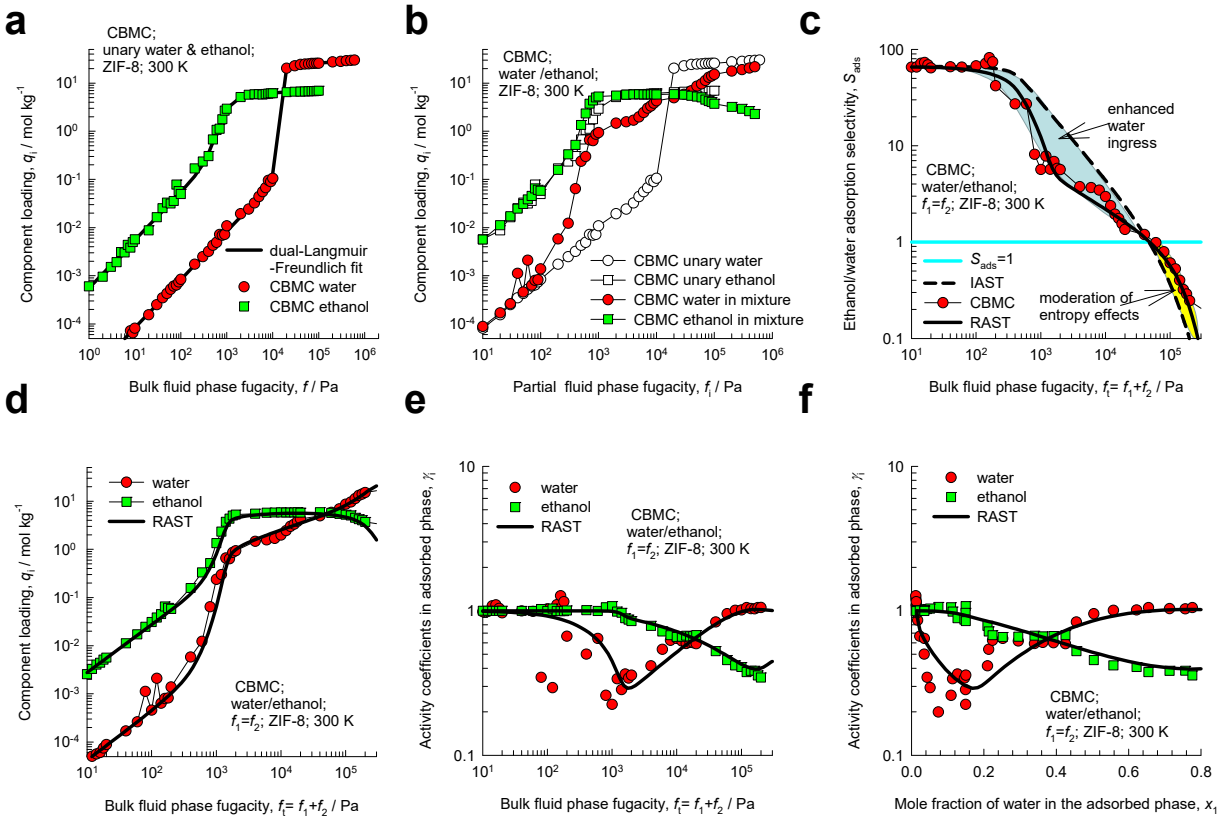

Figure S47. CBMC simulation data and analysis for Campaign A (y_1= 0.5) for water/ethanol mixture adsorption in ZIF-8 at 300 K. (a) Unary isotherms and fits. (b) Component loadings in mixture compared with CBMC simulations of unary isotherms. (c) CBMC data for ethanol/water selectivity compared with IAST and RAST estimates. (d) CBMC data for component loadings in mixture compared with RAST estimates. (e. f) Activity coefficients from CBMC compared with RAST model calculations.

CBMC data for mixture adsorption and RAST analysis

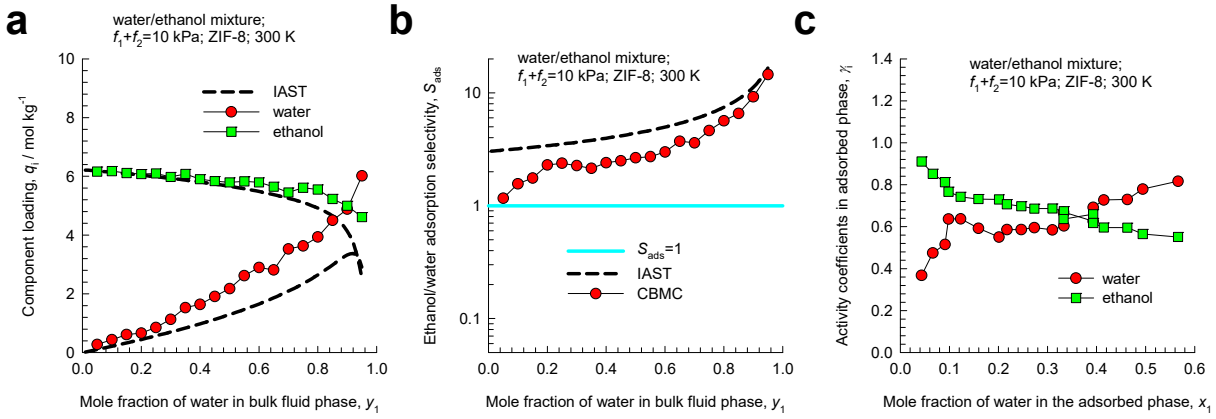

Figure S48. CBMC simulation data and analysis for Campaign B (f_t = 10 kPa) for water/ethanol mixture in ZIF-8 at 300 K. CBMC data on (a) component loadings, and (b) ethanol/water selectivity compared with IAST and RAST estimates. (c) Activity coefficients from CBMC data.

CBMC data for mixture adsorption and RAST analysis

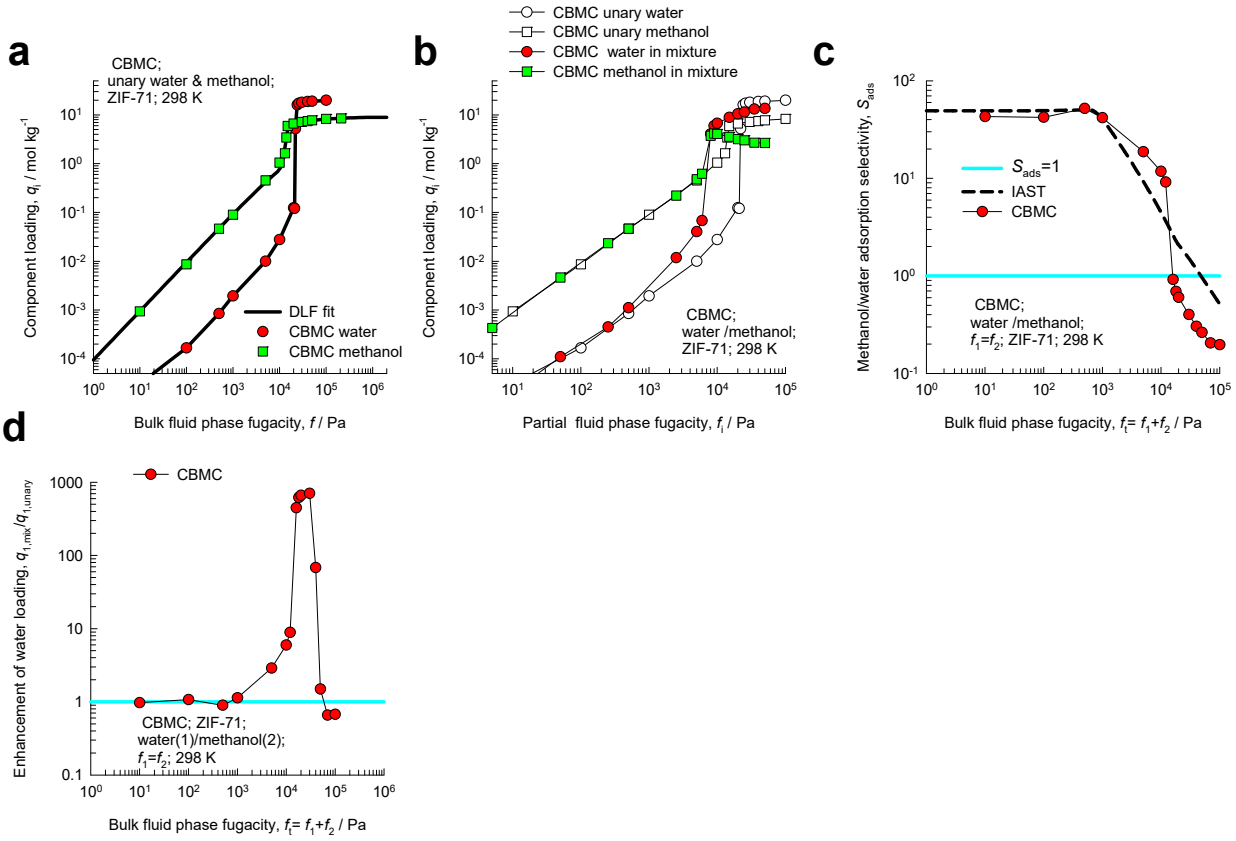

Figure S49. CBMC simulation data and analysis for Campaign A (y_1= 0.5) for water/methanol mixture adsorption in ZIF-71 at 298 K; the CBMC data are culled from Nalaparaju et al.[7] (a) Unary isotherms and fits. (b) Component loadings in mixture compared with CBMC simulations of unary isotherms. (c) CBMC data for alcohol/water selectivity compared with IAST estimates. (d) Enhancement in water loading as function of f_t.

CBMC data for mixture adsorption and RAST analysis

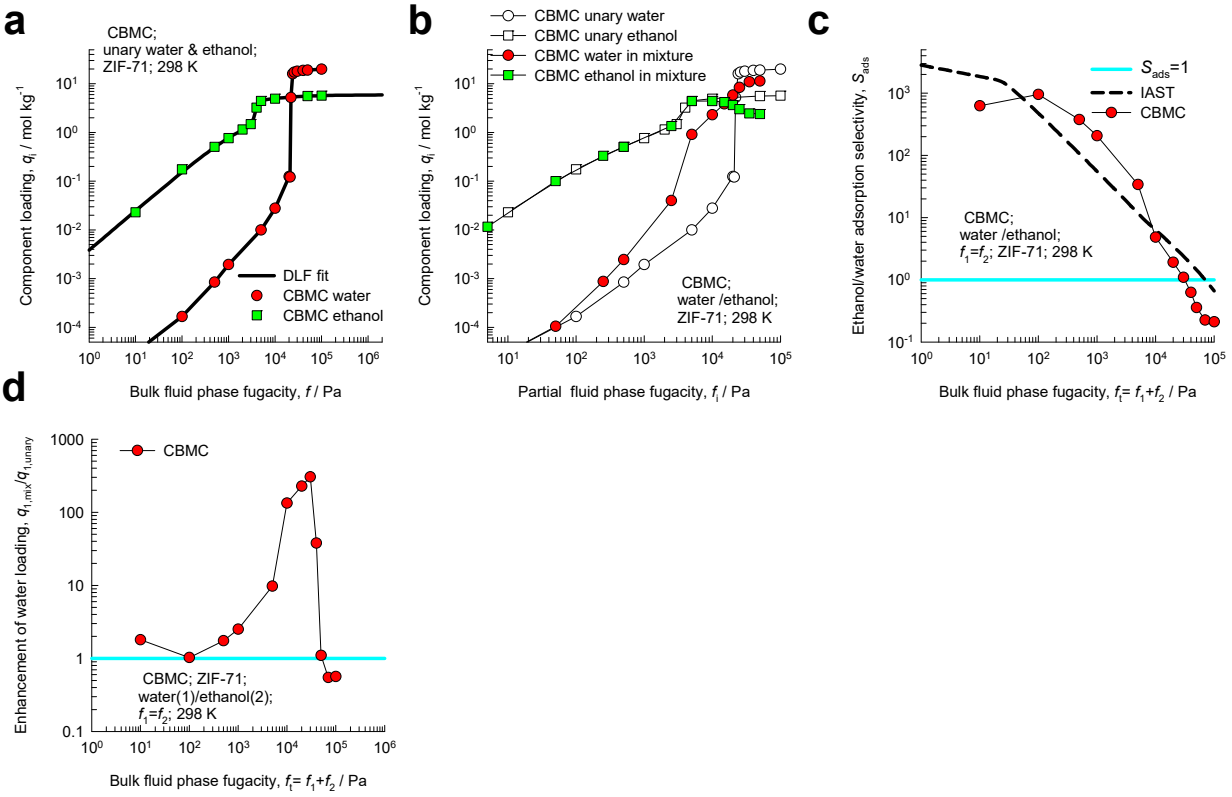

Figure S50. CBMC simulation data and analysis for Campaign A (y_1= 0.5) for water/ethanol mixture adsorption in ZIF-71 at 298 K; the CBMC data are culled from Nalaparaju et al.[7] (a) Unary isotherms and fits. (b) Component loadings in mixture compared with CBMC simulations of unary isotherms. (c) CBMC data for alcohol/water selectivity compared with IAST estimates. (d) Enhancement in water loading as function of f_t.

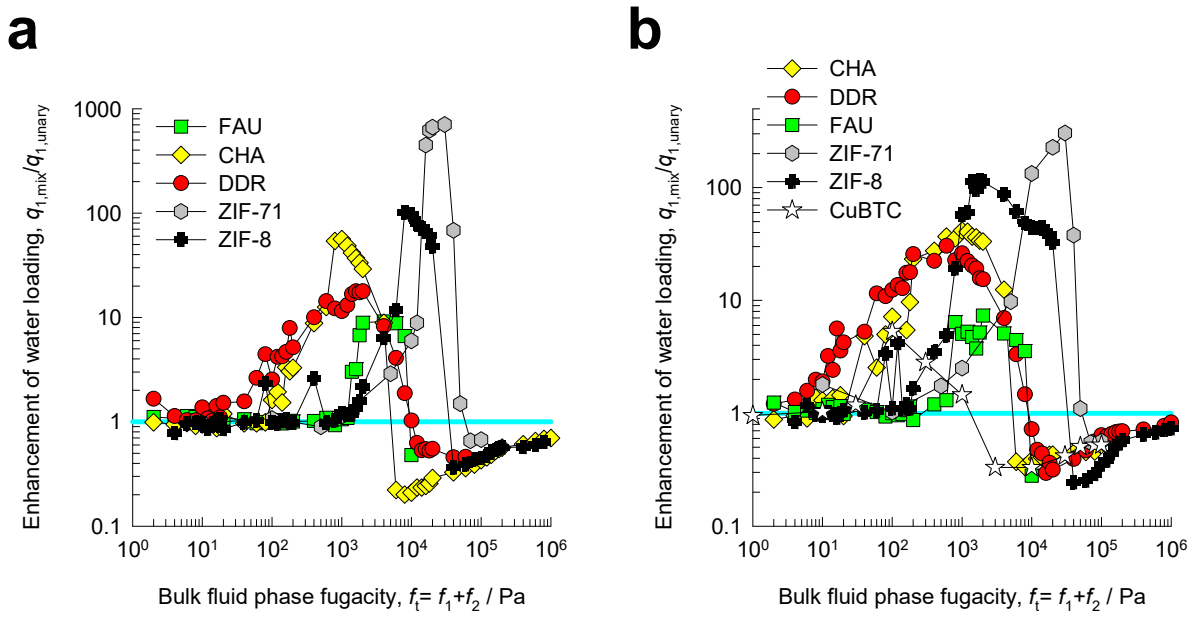

Figure S51. (a, b) Enhancement of water loading in (a) water/methanol, and (b) water/ethanol mixtures, determined from CBMC simulations (Campaign A, y_1= 0.5), in various host materials, with respect to unary loading, using the bulk fugacity f_t as x-axis.

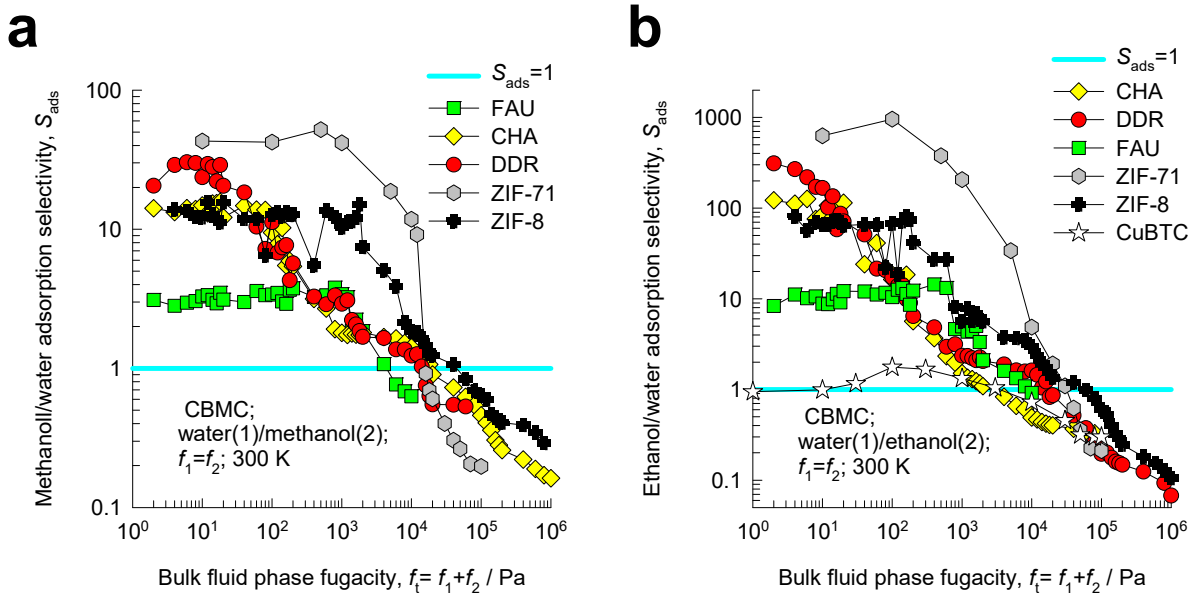

Figure S52. (a, b) Alcohol/water adsorption selectivity for (a) water/methanol, and (b) water/ethanol mixtures, determined from CBMC simulations (Campaign A, y_1= 0.5), in various host materials, using the bulk fugacity f_t as x-axis.

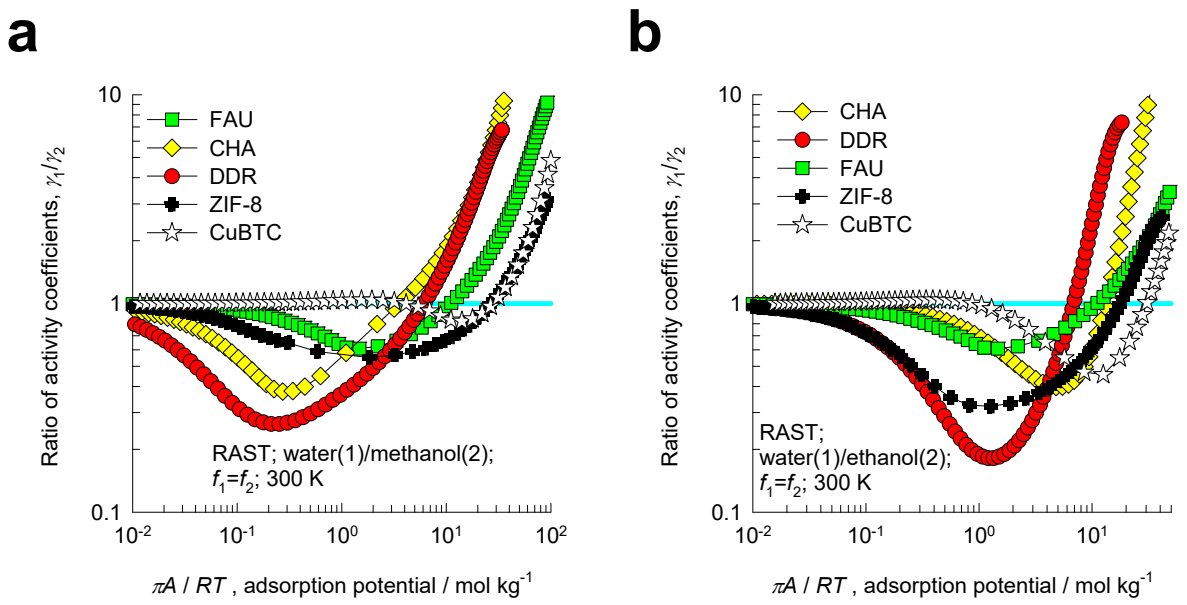

Figure S53. (a, b) RAST calculations, using the Margules model, for the ratios of activity coefficients, γ_1/γ_2 , for various (a) water/methanol and (b) water/ethanol mixtures in various host materials. The *x*-axis.is the adsorption potential, $\pi A/RT$.

CBMC data for mixture adsorption and RAST analysis

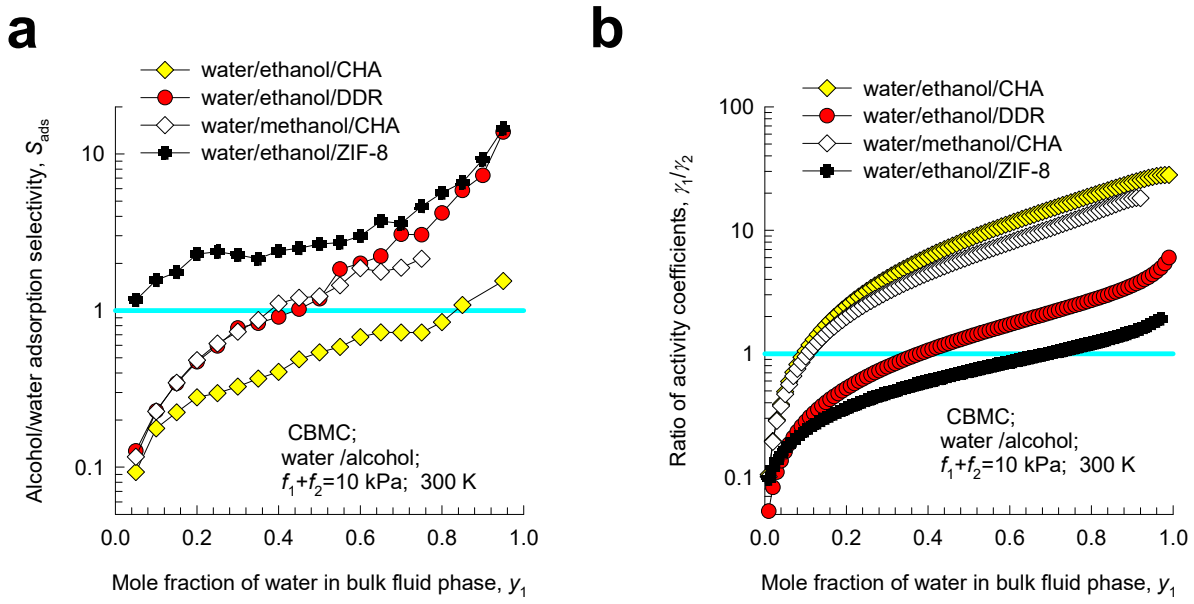

Figure S54. (a) Alcohol/water adsorption selectivity for various water/alcohol mixtures, determined from CBMC simulations (Campaign B, f_t= constant), in various host material. The *x*-axis.is the mole fraction of water(1) in the bulk fluid phase mixture, y_1. Also, plotted in (a) are the CBMC data for ethanol/methanol selectivities. (b) RAST calculations, using the Margules model, for the ratios of activity coefficients, γ_1/γ_2 , for various water/alcohol mixtures in various host materials.

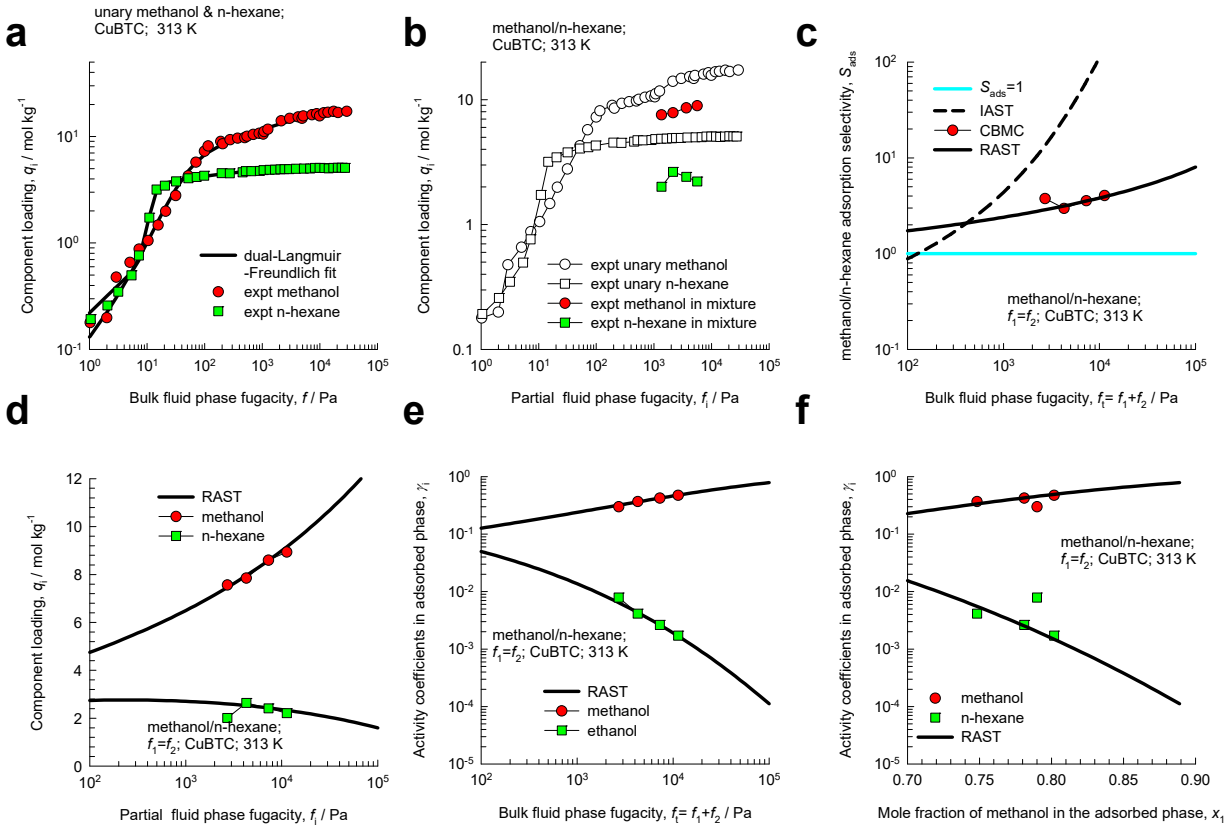

Figure S55. (a) Unary isotherm data of van Assche et al.[41] for adsorption of methanol, and n-hexane at 313 K in CuBTC; the dual-site Langmuir-Freundlich parameters are provided in Table S14. (b) Experimental data of van Assche et al.[41] for component loadings for methanol/n-hexane mixture adsorption in CuBTC as a function of the total pressure, p_t; the partial fugacities in the bulk phase are equal, i.e. p_1=p_2. These loadings are compared with the unary isotherm data. (c) Comparison of the experimental data on the methanol/n-hexane adsorption selectivity, as a function of the total pressure, p_t, with IAST and RAST calculations. (d) Component loadings in mixture compared with RAST model. (e, f) Experimentally determined activity coefficients compared with RAST model calculations.

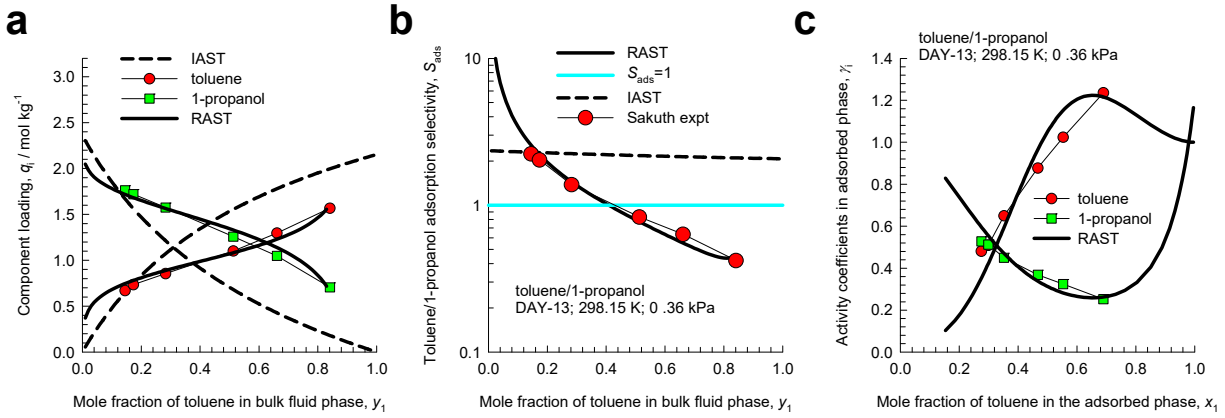

Figure S56. (a, b) Experimental data of Sakuth et al.[42] for (a) component loadings and (b) adsorption selectivity S_{ads} of toluene/1-propanol mixture adsorption in DAY-13 (dealuminated Y zeolite) at T = 298.15 K and total pressure of p_t = 1.06 kPa. (c) The adsorption selectivity S_{ads} plotted as a function of the adsorption potential $\pi A/RT$. Also shown in (a, b) are IAST (dashed lines) and RAST calculations (continuous solid lines) of loadings and S_{ads}. The unary isotherm fit parameters, along with the Margules parameters, are specified in Table S15. (c) Experimental data compared with RAST calculations of the activity coefficients in the adsorbed phase as function of the mole fraction of toluene in the adsorbed phase, x_1.

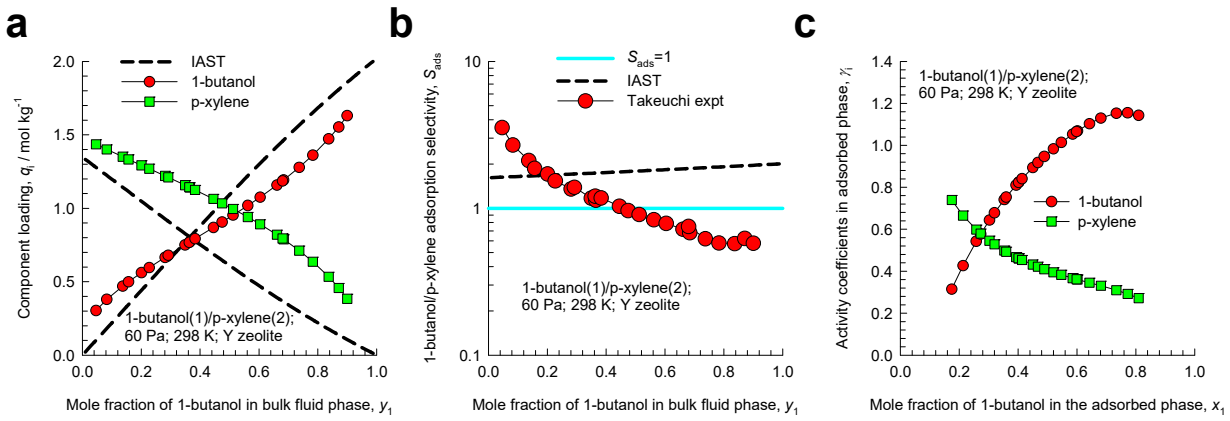

Figure S57. Experimental data of Takeuchi et al.[44] for adsorption of 1-butanol(1)/p-xylene(2) mixtures in high silica Y zeolite, obtained at 298 K and total pressure of 60 Pa. (a) Component loadings in the adsorbed phase plotted as function of the mole fracation of 1-butanol in the bulk vapor phase mixture, y_1. (b) The 1-butanol/p-xylene adsorption selectivity S_{ads} plotted as function as function of mole fraction of 1-butanol(1) in the bulk vapor mixture, y_1. Also shown in (a, b) are IAST (dashed lines) and RAST calculations (continuous solid lines) of loadings and S_{ads}. (c) Experimental data compared with RAST calculations of the activity coefficients in the adsorbed phase as function of the mole fraction of toluene in the adsorbed phase, x_1. The unary isotherm parameters are specified in Table S16.

CBMC data for mixture adsorption and RAST analysis

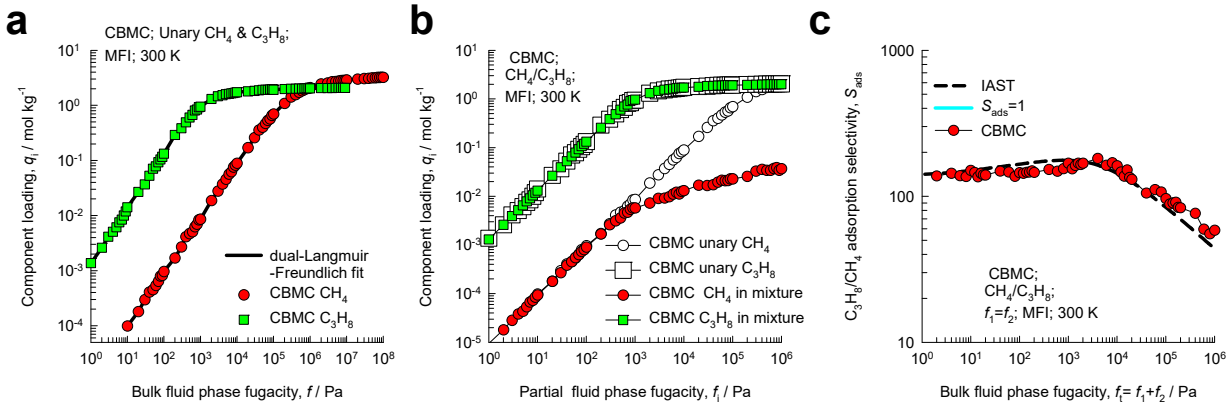

Figure S58. CBMC simulation data and analysis for Campaign A (y_1= 0.5) for CH_4(1)/C_3H_8(2) mixture adsorption in MFI zeolite at 300 K. (a) Unary isotherms and fits. (b) Component loadings in mixture compared with CBMC simulations of unary isotherms. (c) CBMC data for C_3H_8(2)/CH_4(1) selectivity compared with IAST estimates. The unary isotherm data fits are provided in Table S20.

CBMC data for mixture adsorption and RAST analysis

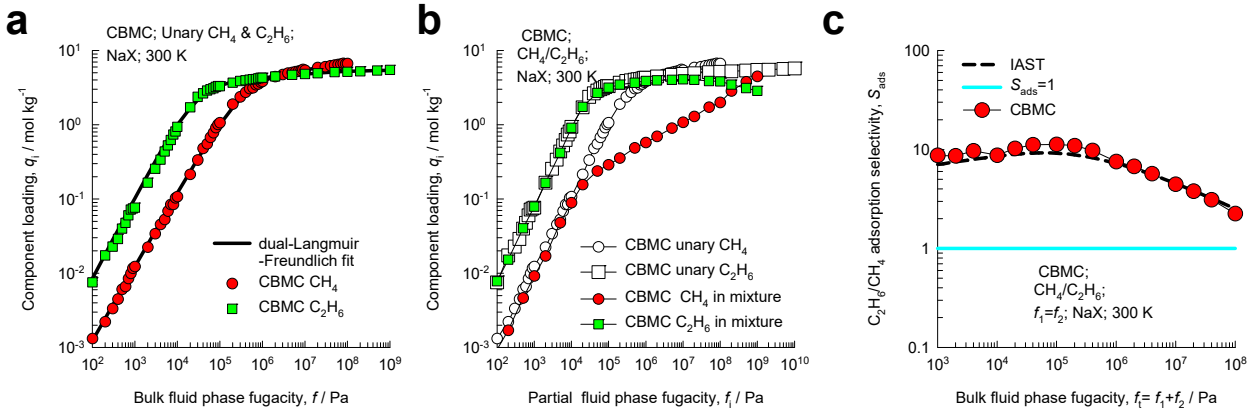

Figure S59. CBMC simulation data and analysis for Campaign A (y_1= 0.5) for CH_4(1)/C_2H_6(2) mixture adsorption in NaX (106 Si, 86 Al, 86 Na^+, Si/Al=1.23) at 300 K. (a) Unary isotherms and fits. (b) Component loadings in mixture compared with CBMC simulations of unary isotherms. (c) CBMC data for C_2H_6(2)/CH_4(1) selectivity compared with IAST estimates. The unary isotherm data fits are provided in Table S17.

CBMC data for mixture adsorption and RAST analysis

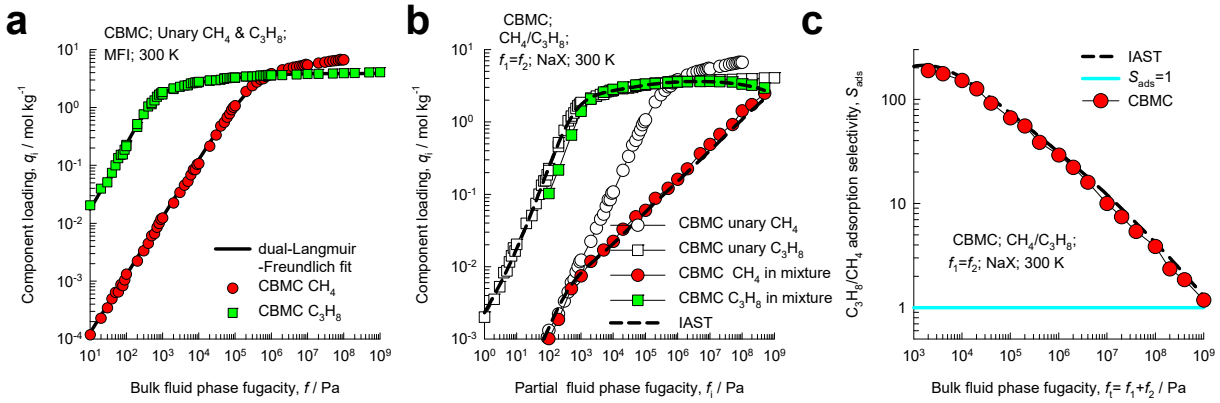

Figure S60. CBMC simulation data and analysis for Campaign A (y_1= 0.5) for CH_4(1)/C_3H_8(2) mixture adsorption in NaX (106 Si, 86 Al, 86 Na^+, Si/Al=1.23) at 300 K. (a) Unary isotherms and fits. (b) Component loadings in mixture compared with CBMC simulations of unary isotherms. (c) CBMC data for C_3H_8(2)/CH_4(1) selectivity compared with IAST estimates. The unary isotherm data fits are provided in Table S17.

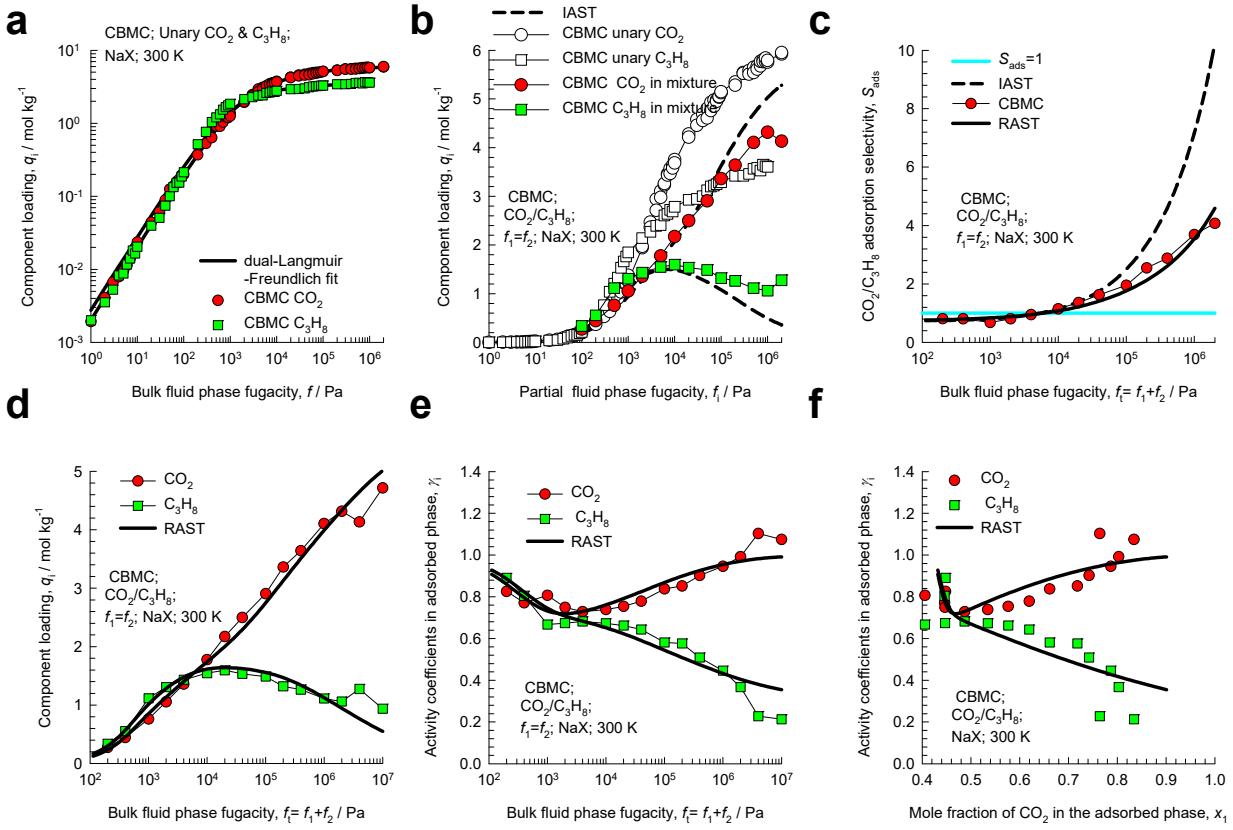

Figure S61. CBMC simulation data and analysis for Campaign A (y_1= 0.5) for CO_2(1)/C_3H_8(2) mixture adsorption in NaX (106 Si, 86 Al, 86 Na^+, Si/Al=1.23) at 300 K. (a) Unary isotherms and fits. (b) Component loadings in mixture compared with CBMC simulations of unary isotherms. (c) CBMC data for CO_2(1)/C_3H_8(2) selectivity compared with IAST and RAST estimates. (d) CBMC data for component loadings in mixture compared with RAST estimates. (e. f) Activity coefficients from CBMC compared with RAST model calculations. The unary isotherm data fits and Margules parameters are provided in in Table S12.

CBMC data for mixture adsorption and RAST analysis

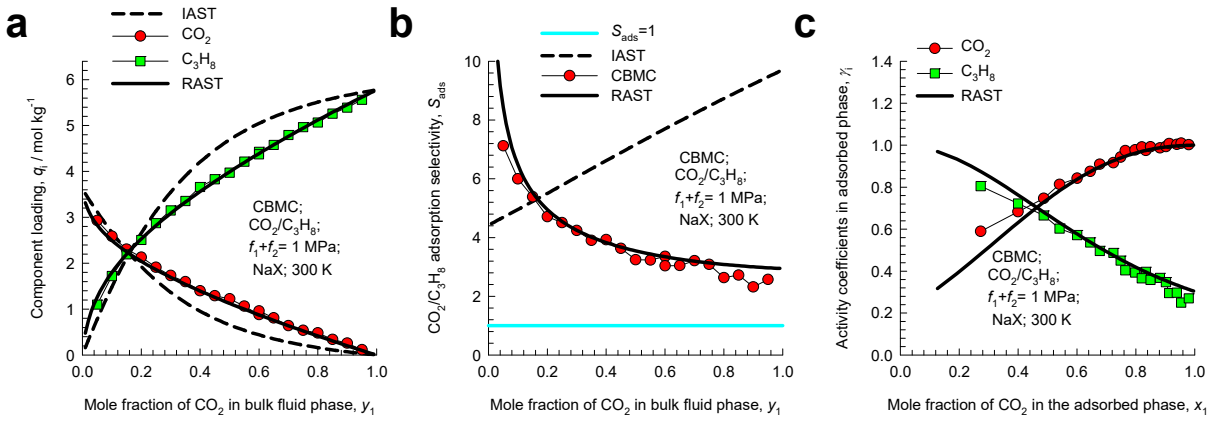

Figure S62. CBMC simulation data and analysis for Campaign B (f_t = 1 MPa) for CO_2(1)/C_3H_8(2) mixture adsorption in NaX (106 Si, 86 Al, 86 Na^+, Si/Al=1.23) at 300 K. CBMC data for (a) component loadings and (b) CO_2(1)/C_3H_8(2) selectivity compared with IAST and RAST estimates. (c) Activity coefficients from CBMC compared with RAST model calculations. The unary isotherm data fits and Margules parameters are provided in in Table S12.

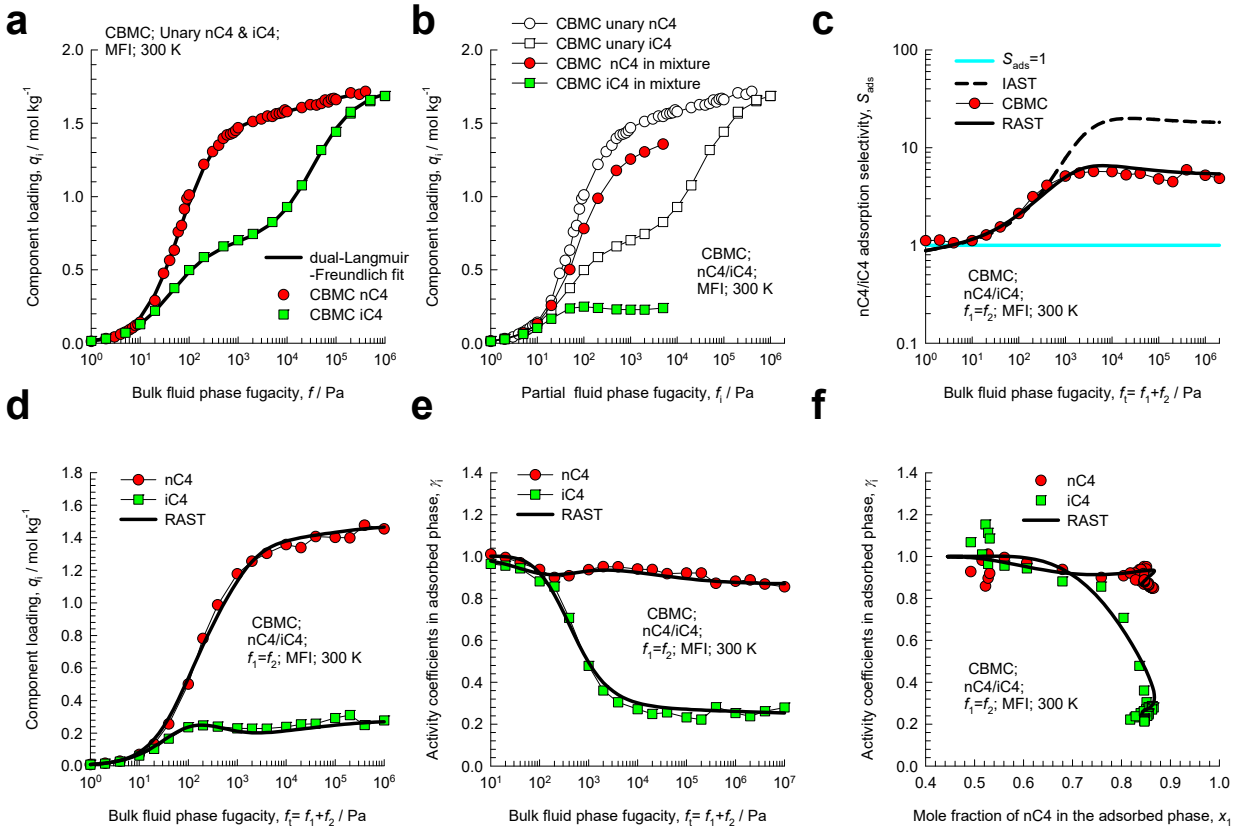

Figure S63. CBMC simulation data and analysis for Campaign A (y_1= 0.5) for binary nC4/iC4 mixtures in MFI zeolite at 300 K. (a) Unary isotherms and fits. (b) Component loadings in mixture compared with CBMC simulations of unary isotherms. (c) CBMC data for nC4(1)/iC4(2) selectivity compared with IAST and RAST estimates. (d) CBMC data for component loadings in mixture compared with RAST estimates. (e. f) Activity coefficients from CBMC compared with RAST model calculations. The unary isotherm data fits and Margules parameters are provided in Table S13.

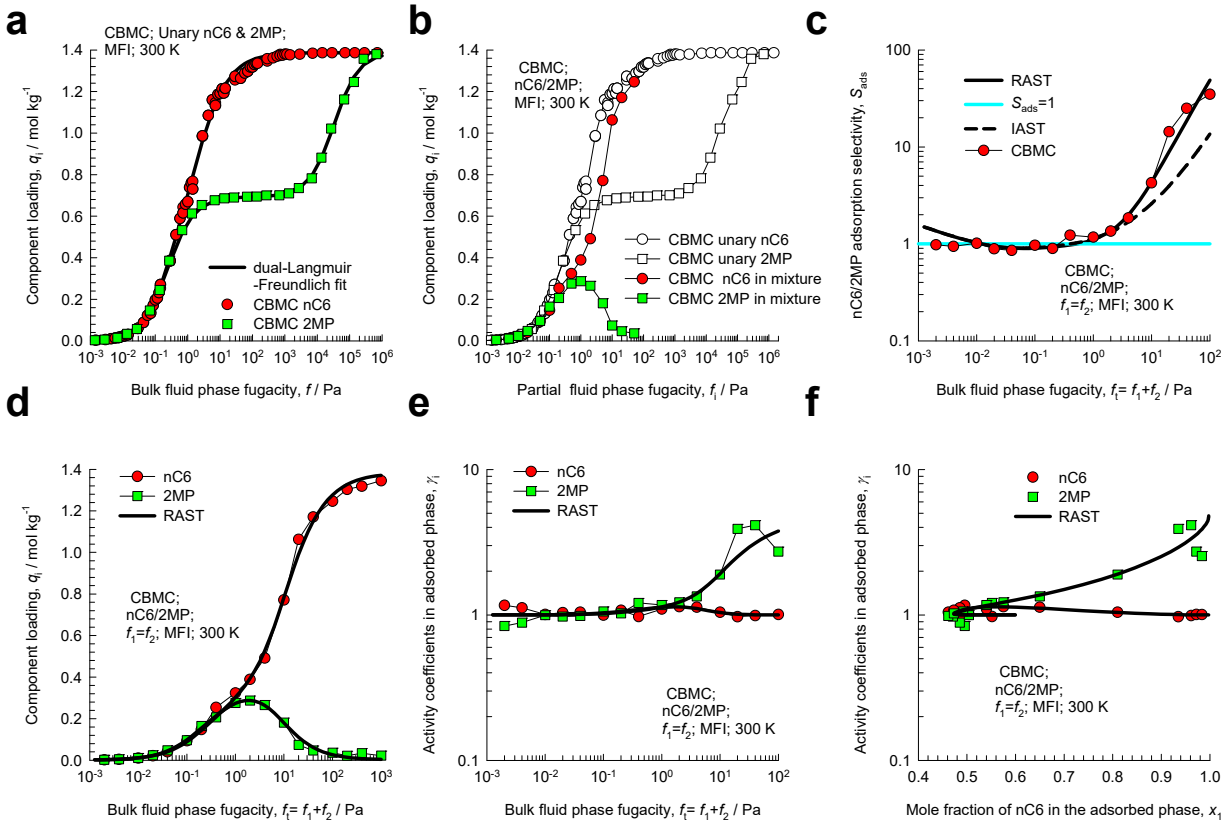

Figure S64. CBMC simulation data and analysis for Campaign A (y_1= 0.5) for binary nC6/2MP mixtures in MFI zeolite at 300 K. (a) Unary isotherms and fits. (b) Component loadings in mixture compared with CBMC simulations of unary isotherms. (c) CBMC data for nC6(1)/2MP(2) selectivity compared with IAST and RAST estimates. (d) CBMC data for component loadings in mixture compared with RAST estimates. (e. f) Activity coefficients from CBMC compared with RAST model calculations. The unary isotherm data fits and Margules parameters are provided in Table S13.

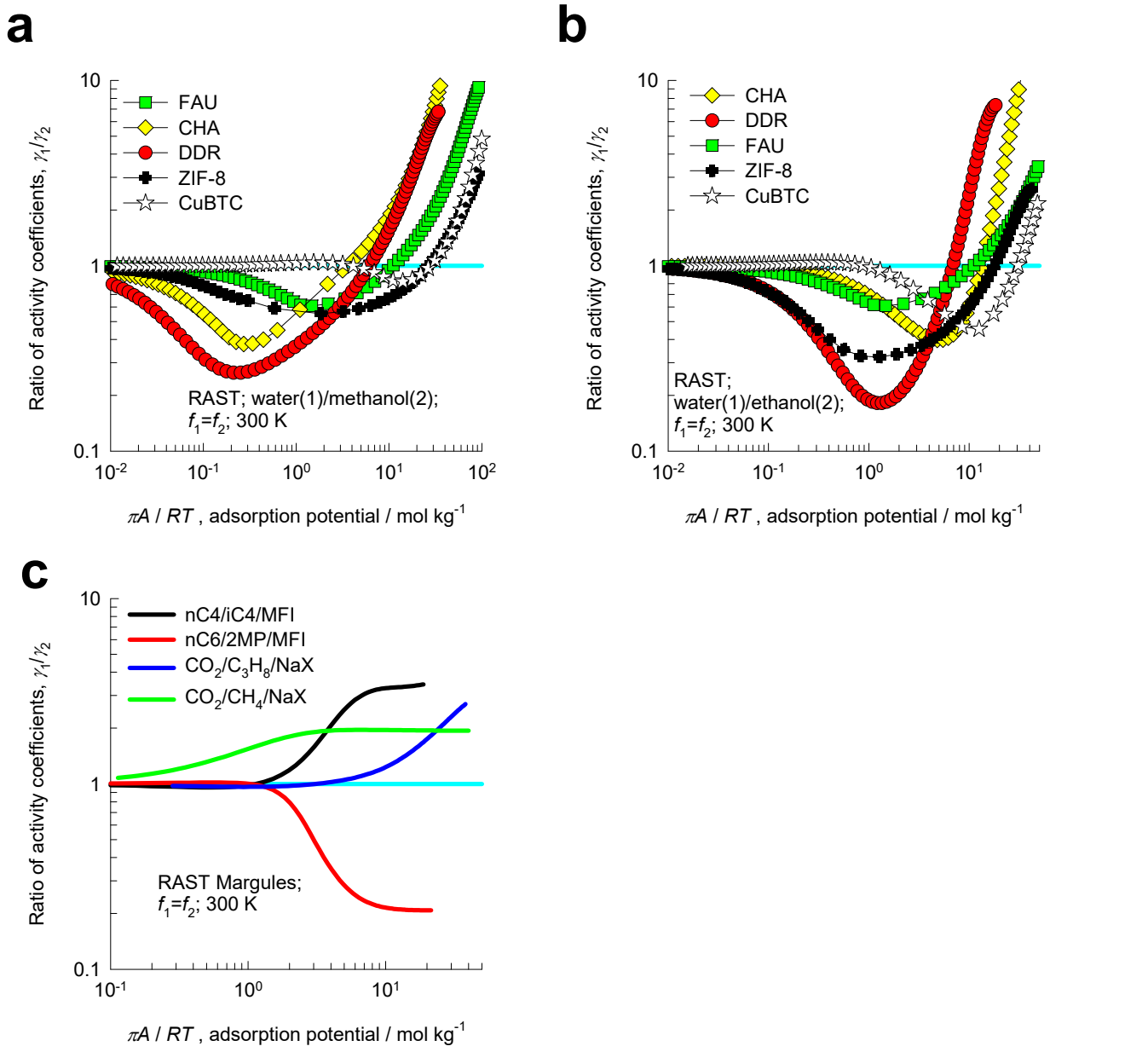

Figure S65. (a, b, c) RAST (Margules) calculations of the ratio of activity coefficients γ_1/γ_2 for (a) water/methanol, (b) water/ethanol, (c) gaseous mixtures subject to non-idealities induced by congregation/segregation effects. The *x*-axes represent the adsorption potential, $\pi A/RT$.

CBMC data for mixture adsorption and RAST analysis

7 Nomenclature

Latin alphabet

A	surface area per kg of framework, $m^2\ kg^{-1}$
A_{12}, A_{21}	Margules parameters, dimensionless
b_i	Langmuir-Freundlich parameter, $Pa^{-\nu}$
C	constant used in eq (S16), kg mol^{-1}
f_i	partial fugacity of species *i*, Pa
f_t	total fugacity of bulk fluid mixture, Pa
G^{excess}	excess Gibbs free energy, J mol^{-1}
n	number of species in the mixture, dimensionless
p_i	partial pressure of species *i*, Pa
p_t	total system pressure, Pa
P_i^0	sorption pressure, Pa
q_i	molar loading of species *i*, mol kg^{-1}
q_t	total molar loading of mixture, mol kg^{-1}
$q_{i,sat}$	molar loading of species *i* at saturation, mol kg^{-1}
R	gas constant, 8.314 J mol^{-1} K^{-1}
S_{ads}	adsorption selectivity, dimensionless
S_{diff}	diffusion selectivity, dimensionless
S_{perm}	permeation selectivity, dimensionless
T	absolute temperature, K
V_p	pore volume, $m^3\ kg^{-1}$
x_i	mole fraction of species *i* in adsorbed phase, dimensionless

Nomenclature

y_i	mole fraction of species *i* in bulk fluid mixture, dimensionless

Greek letters

γ_i	activity coefficient of component *i* in adsorbed phase, dimensionless
μ_i	molar chemical potential, J mol^{-1}
ν	Freundlich exponent, dimensionless
π	spreading pressure, N m^{-1}
ρ	framework density, kg m^{-3}

Subscripts

i,j	components in mixture
i	referring to component *i*
t	referring to total mixture
sat	referring to saturation conditions

Superscripts

0	referring to pure component loading
excess	referring to excess parameter

8 References

(1) Olson, D. H.; Camblor, M. A.; Vallaescusa, L. A.; Kuehl, G. H. Light hydrocarbon sorption properties of pure silica Si-CHA and ITQ-3 and high silica ZSM-58. *Microporous Mesoporous Mater.* **2004**, *67*, 27-33.

(2) Hedin, N.; DeMartin, G. J.; Roth, W. J.; Strohmaier, K. G.; Reyes, S. C. PFG NMR self-diffusion of small hydrocarbons in high silica DDR, CHA and LTA structures. *Microporous Mesoporous Mater.* **2008**, *109*, 327-334.

(3) Ruthven, D. M.; Reyes, S. C. Adsorptive separation of light olefins from paraffins. *Microporous Mesoporous Mater.* **2007**, *104*, 59-66.

(4) Khalighi, M.; Chen, Y. F.; Farooq, S.; Karimi, I. A.; Jiang, J. W. Propylene/Propane Separation Using SiCHA. *Ind. Eng. Chem. Res.* **2013**, *52*, 3877-3892.

(5) Gies, H. Studies on clathrasils IX: Crystal structure of decadodecasil 3 R, the missing link between zeolites and clathrasils. *Z. Kristallogr.* **1986**, *175*, 93-104.

(6) van Koningsfeld, H.; Jansen, J. C.; van Bekkum, H. The monoclinic framework structure of zeolite H-ZSM-5. Comparison with the orthorhombic framework of as-synthesized ZSM-5. *Zeolites* **1990**, *10*, 235-242.

(7) Nalaparaju, A.; Zhao, X. S.; Jiang, J. W. Molecular Understanding for the Adsorption of Water and Alcohols in Hydrophilic and Hydrophobic Zeolitic Metal-Organic Frameworks. *J. Phys. Chem. C* **2010**, *114*, 11542-11550.

(8) Chui, S. S. Y.; Lo, S. M. F.; Charmant, J. P. H.; Orpen, A. G.; Williams, I. D. A Chemically Functionalizable Nanoporous Material $[Cu_3(TMA)_2(H2O)_3]_n$. *Science* **1999**, *283*, 1148-1150.

(9) Yang, Q.; Zhong, C. Electrostatic-Field-Induced Enhancement of Gas Mixture Separation in Metal-Organic Frameworks: A Computational Study. *ChemPhysChem* **2006**, *7*, 1417-1421.

(10) Krishna, R.; van Baten, J. M. Hydrogen Bonding Effects in Adsorption of Water-alcohol Mixtures in Zeolites and the Consequences for the Characteristics of the Maxwell-Stefan Diffusivities. *Langmuir* **2010**, *26*, 10854-10867.

(11) Krishna, R.; van Baten, J. M. Mutual slowing-down effects in mixture diffusion in zeolites. *J. Phys. Chem. C* **2010**, *114*, 13154-13156.

(12) Krishna, R.; van Baten, J. M. Highlighting Pitfalls in the Maxwell-Stefan Modeling of Water-Alcohol Mixture Permeation across Pervaporation Membranes. *J. Membr. Sci.* **2010**, *360*, 476-482.

(13) Kuhn, J.; Castillo-Sanchez, J. M.; Gascon, J.; Calero, S.; Dubbeldam, D.; Vlugt, T. J. H.; Kapteijn, F.; Gross, J. Adsorption and Diffusion of Water, Methanol, and Ethanol in All-Silica DD3R: Experiments and Simulation. *J. Phys. Chem. C* **2009**, *113*, 14290-14301.

(14) Rick, S. W. A Reoptimization of the Five-site Water Potential (TIP5P) for use with Ewald Sums. *J. Chem. Phys.* **2004**, *120*, 6085-6093.

(15) Chen, B.; Potoff, J. J.; Siepmann, J. I. Monte Carlo Calculations for Alcohols and Their Mixtures with Alkanes. Transferable Potentials for Phase Equilibria. 5. United-Atom Description of Primary, Secondary, and Tertiary Alcohols. *J. Phys. Chem. B* **2001**, *105*, 3093-3104.

(16) Kiselev, A. V.; Lopatkin, A. A.; Shul'ga, A. A. Molecular statistical calculation of gas adsorption by silicalite. *Zeolites* **1985**, *5*, 261-267.

(17) Mayo, S. L.; Olafson, B. D.; Goddard, W. A. DREIDING: A Generic Force Field for Molecular Simulations. *J. Phys. Chem.* **1990**, *94*, 8897-8909.

(18) Yang, Q.; Zhong, C. Understanding Hydrogen Adsorption in Metal-Organic Frameworks with Open Metal Sites: A Computational Study. *J. Phys. Chem. B* **2006**, *110*, 655-658.

(19) Jorgensen, W. L.; Maxwell, D. S.; Tirado-Rives, J. Development and Testing of the OPLS All-Atom Force Field on Conformational Energetics and Properties of Organic Liquids. *J. Am. Chem. Soc.* **1996**, *118*, 11225-11236.

(20) Zhou, M.; Wang, Q.; Zhang, L.; Liu, Y. C.; Kang, Y. Adsorption Sites of Hydrogen in Zeolitic Imidazolate Frameworks. *J. Phys. Chem. B* **2009**, *113*, 11049-11053.

(21) Xu, Q.; Zhong, C. A General Approach for Estimating Framework Charges in Metal-Organic Frameworks. *J. Phys. Chem. C* **2010**, *114*, 5035-5042.

(22) Frenkel, D.; Smit, B. *Understanding Molecular Simulations: From Algorithms to Applications*. 2nd Edition, Academic Press: San Diego, 2002.

(23) Vlugt, T. J. H. BIGMAC. http://molsim.chem.uva.nl/bigmac/, University of Amsterdam, 1 November 2000.

(24) Gutierrez-Sevillano, J. J.; Calero, S.; Krishna, R. Selective Adsorption of Water from Mixtures with 1-Alcohols by Exploitation of Molecular Packing Effects in CuBTC. *J. Phys. Chem. C* **2015**, *119*, 3658-3666.

(25) Gutierrez-Sevillano, J. J.; Calero, S.; Krishna, R. Separation of Benzene from Mixtures with Water, Methanol, Ethanol, and Acetone: Highlighting Hydrogen Bonding and Molecular Clustering Influences in CuBTC. *Phys. Chem. Chem. Phys.* **2015**, *17*, 20114-20124.

(26) Ruthven, D. M. *Principles of Adsorption and Adsorption Processes*. John Wiley: New York, 1984.

(27) Myers, A. L.; Prausnitz, J. M. Thermodynamics of Mixed Gas Adsorption. *A.I.Ch.E.J.* **1965**, *11*, 121-130.

(28) Siperstein, F. R.; Myers, A. L. Mixed-Gas Adsorption. *A.I.Ch.E.J.* **2001**, *47*, 1141-1159.

(29) Krishna, R.; Van Baten, J. M. Elucidation of Selectivity Reversals for Binary Mixture Adsorption in Microporous Adsorbents. *ACS Omega* **2020**, *5*, 9031-9040. https://doi.org/10.1021/acsomega.0c01051.

(30) Krishna, R.; Van Baten, J. M. Using Molecular Simulations for Elucidation of Thermodynamic Non-Idealities in Adsorption of CO_2-containing Mixtures in NaX Zeolite. *ACS Omega* **2020**, *5*, 20535-20542. https://doi.org/10.1021/acsomega.0c02730.

(31) Krishna, R.; Van Baten, J. M. Investigating the Non-idealities in Adsorption of CO_2-bearing Mixtures in Cation-exchanged Zeolites. *Sep. Purif. Technol.* **2018**, *206*, 208-217. https://doi.org/10.1016/j.seppur.2018.06.009.

(32) Talu, O.; Myers, A. L. Rigorous Thermodynamic Treatment of Gas-Adsorption. *A.I.Ch.E.J.* **1988**, *34*, 1887-1893.

(33) Talu, O.; Zwiebel, I. Multicomponent Adsorption Equilibria of Nonideal Mixtures. *A.I.Ch.E.J.* **1986**, *32*, 1263-1276.

(34) Zhang, C.; Yang, X. Molecular dynamics simulation of ethanol/water mixtures for structure and diffusion properties. *Fluid Phase Equilib.* **2005**, *231*, 1-10.

(35) Krishna, R.; van Baten, J. M.; Baur, R. Highlighting the Origins and Consequences of Thermodynamic Nonidealities in Mixture Separations using Zeolites and Metal-Organic Frameworks. *Microporous Mesoporous Mater.* **2018**, *267*, 274-292. http://dx.doi.org/10.1016/j.micromeso.2018.03.013.

(36) Krishna, R. Separating Mixtures by Exploiting Molecular Packing Effects in Microporous Materials. *Phys. Chem. Chem. Phys.* **2015**, *17*, 39-59.

(37) Krishna, R. Elucidation and Characterization of Entropy Effects in Mixture Separations with Micro-porous Crystalline Adsorbents. *Sep. Purif. Technol.* **2019**, *215*, 227-241. https://doi.org/10.1016/j.seppur.2019.01.014.

References

(38) Krishna, R.; van Baten, J. M. Separating n-alkane mixtures by exploiting differences in the adsorption capacity within cages of CHA, AFX and ERI zeolites. *Sep. Purif. Technol.* **2008**, *60*, 315-320.

(39) Krishna, R.; van Baten, J. M. Entropy-based Separation of Linear Chain Molecules by Exploiting Differences in the Saturation Capacities in Cage-type Zeolites. *Sep. Purif. Technol.* **2011**, *76*, 325-330.

(40) Krishna, R.; van Baten, J. M. Commensurate-Incommensurate Adsorption and Diffusion in Ordered Crystalline Microporous Materials. *Phys. Chem. Chem. Phys.* **2017**, *19*, 20320-20337.

(41) Van Assche, T. R. C.; Duerinck, T.; Van der Perre, S.; Baron, G. V.; Denayer, J. F. M. Prediction of Molecular Separation of Polar−Apolar Mixtures on Heterogeneous Metal−Organic Frameworks: HKUST-1. *Langmuir* **2014**, *30*, 7878−7883.

(42) Sakuth, M.; Meyer, J.; Gmehling, J. Vapor Phase Adsorption Equilibria of Toluene + 1-Propanol Mixtures on Y-Zeolites with Different Silicon to Aluminum Ratios. *J. Chem. Eng. Data* **1995**, *40*, 895-899.

(43) Sakuth, M.; Meyer, J.; Gmehling, J. Measurement and Prediction of Binary Adsorption Equilibria of Vapors on Dealuminated Y-zeolites (DAY). *Chem. Eng. Process.* **1998**, *37*, 267-277.

(44) Takeuchi, Y.; Iwamoto, H.; Miyata, N.; Asano, S.; Harada, M. Adsorption of l-butanol and p-xylene vapor with high silica zeolites. *Separations Technology* **1995**, *5*, 23-24.